Title

Bridging Cell Biology with Macroscopic Tumor Features via Large-Scale Computational Modeling

Author

Du, Jiayi

Publication Date

2024

Peer reviewed|Thesis/dissertation

UNIVERSITY OF CALIFORNIA

Los Angeles

Bridging Cell Biology with Macroscopic Tumor Features via Large-Scale Computational Modeling

A dissertation submitted in partial satisfaction of the requirements for the degree Doctor of Philosophy in Physics and Biology in Medicine

by

Jiayi Du

2024

ABSTRACT OF THE DISSERTATION

Bridging Cell Biology with Macroscopic Tumor Features via Large-Scale Computational Modeling

by

Jiayi Du

Doctor of Philosophy in Physics and Biology in Medicine

University of California, Los Angeles, 2024

Professor Ke Sheng, Committee Chair

Radiomics offers a promising method to discern tumor biology through non-invasive medical imaging, successfully performing various prediction tasks and demonstrating potential in clinical applications. However, limitations in interpretability and robustness are significant obstacles to its broad clinical adoption. In the era of personalized medicine, there is an urgent need to better understand the physio-biological properties reflected by Radiomics and, more fundamentally, the multiscale problem of how these microscopic tissue properties develop as the tumor grows, leading to macroscopic tumor patterns or features in medical images.

In this study, we introduced a hybrid simulation platform that integrates continuum tissue dynamics with discrete vasculature modeling for large-scale, vascularized tumor growth simulations with comprehensive hemodynamic capabilities. Through innovative vasculature conditioning and remodeling strategies, this platform enables unbiased simulations of tumor development to sizes previously unattainable, closely mirroring the biophysical vascular properties and tissue growth patterns observed in actual tumors.

Our study has significant implications for understanding tumor characteristics. By examining the influence of cellular proliferation rate (PR) and oxygen consumption rate (OCR) on tumor patterning and heterogeneity, we have elucidated the mechanistic links between biophysical properties and tumor characteristics. Key findings include the pivotal role of tumor proliferation rate in driving necrosis and tissue heterogeneity and the impact of OCR on tissue vascular density. Using our platform, we analyzed 20 randomly generated samples to predict PR and OCR using Radiomics, based on semantic and agnostic features. The resulting high-performance predictive model sees through tumor appearance to identify critical features that uncover underlying biological processes. Given the insight from modeling, the rationale behind feature selection can be understood, and features can be interpreted.

Our study advanced our understanding of the complex tumor vasculature and tissue development problem and laid the groundwork for integrating computational models with Radiomics, bridging the gap between data-driven tumor prediction and fundamental biophysics. This integration opens up exciting new avenues for research in personalized medicine and beyond. It provides a new paradigm for interpreting tumor features and can help identify tumor property types with the

highest potential to reveal specific biophysical properties, guiding the development and selection of imaging modalities for advanced non-invasive biophysical assessments.

The dissertation of Jiayi Du is approved.

Arion-Xenofon Hadjioannou

Lihua Jin

Michael McNitt-Gray

Xiangrong Qi

Ke Sheng, Committee Chair

University of California, Los Angeles

2024

Contents

LIST OF TABLES

LIST OF FIGURES

LIST OF EQUATIONS

LIST OF ABBREVIATIONS AND ACRONYMS

CT

Computed Tomography

MRI

Magnetic Resonance Imaging

PET

Positron Emission Tomography

GBM

Glioblastoma Multiforme

PR

Proliferation Rate

DT

Doubling Time

OCR

Oxygen Consumption Rate

PDE

Partial Differential Equation

ODE

Ordinary Differential Equation

BC

Boundary Condition

RRMSE

Relative Root Mean Squared Error

ACKNOWLEDGEMENTS

I would like to first extend my deepest gratitude to my parents for their unwavering love and support. Despite being unfamiliar with my field of study, they have always trusted in me and supported my decisions unconditionally, from undergraduate to graduate school. My father, Zhanping, exemplifies lifelong learning. He never stops reading whenever he has the opportunity, inspiring me with his dedication and work ethic. In the midst of my PhD, my mom, Shuqi, was unfortunately diagnosed with breast cancer and faced a long battle against the disease. Despite her struggles, she never wanted me to worry. During our phone calls, she always maintained an optimistic attitude and put on a brave face, shielding me from her pain. Her enduring love always comforts me, and I am immensely proud of her resilience as a cancer fighter.

My greatest thanks go to my advisor, Dr. Ke Sheng, the best mentor I could ever ask for. Dr. Sheng's enthusiasm for research and deep insights into the field are genuinely inspiring. He is an exceptionally supportive and kind mentor, always trying to provide the ideal resource and healthy research environment and encouraging us to explore our field freely. It is both a true privilege and an honor to work with him.

I also would like to thank Dr. Dan Ruan, who provides invaluable advice to guide all the students around her and genuinely cares about our lives. She has also been a role model for her students and us, showing us what a good person and researcher should be like.

Many thanks to our collaborators, Yu Zhou and Prof. Lihua Jin. Without their expertise and insight in continuum mechanics, many of the achievements would be otherwise impossible.

Thanks also go to my classmates and labmates at UCLA: Hengjie, Zhengyang, Yingqing, Zhou, Daili, Elizabeth, Ryan, Qihui, Wenbo, Kaley, Pav, Alan, Qifan, Lu, Xinyi, and Flute. As well as my undergraduate friends around the US include Dayu, Dong, Lingfeng, and Tingyu. Life would be tough without their help and company. A Special thanks to Elizabeth for being a lovely big sister in the lab, and I sincerely hope for her swift and complete recovery from her health challenges.

VITA

Education:

University of Science and Technology of China Hefei, Anhui

BS, Physics 2014-2018

Thesis: CT Reconstruction from Partial Data by Deep Learning; Advised by Dr. Lei Zhu

University of California, Los Angeles Los Angeles, California

Ph.D. Candidate, Physics and Biology in Medicine 2018-2024

Thesis: Bridging Cell Biology with Macroscopic Tumor Features via Large-Scale Computational Modeling; Advised by Dr. Ke Sheng

Awards

Outstanding Academic Scholarship

2014-2016

Publication

J Du, Y Zhou, L Jin, K Sheng. Gell: A GPU-powered 3D hybrid simulator for large-scale multicellular system. Plos one. 2023 Jul 18;18(7):e0288721.

Conference & Presentations:

1. **J Du**, K Sheng. Oxygen Depletion Kinetics Due to Flash with Real Tumor Vasculature Coupling. AAPM 2023. (Oral)
2. **J Du**, K Sheng. Modeling Tumor Vasculature for Perfusion and Oxygenation Analysis. AAPM 2023. (Poster)
3. **J Du**, Y Zhou, L Jin, K Sheng. A Hybrid Tumor Model for Ultra-Large-Scale Heterogeneous Vascular Tumor Growth. International Journal of Radiation Oncology, Biology, Physics. 2022 Nov 1;114(3):e92. (Poster)
4. **J Du**, Y Zhou, L Jin, K Sheng. Gell: A GPU-Powered Ultra-Large-Scale Cell-Based Simulator. AAPM 2022. (Poster)
5. **J Du**, Y Zhou, L Jin, K Sheng. A Hybrid Tumor Model for Ultra-Large-Scale Heterogeneous Vascular Tumor Growth. AAPM 2022. (Poster)
6. **J Du**, Y Zhou, L Jin, K Sheng. Development of Gell: A GPU-Powered Ultra-Large-Scale Cell-Based Simulator. AAPM 2021. (Poster)
7. **J Du**, XS Qi, R Chin, K Sheng. Independent Feature Selection in Radiomics Cross-Validation Is Essential to Estimate the True Model Performance. AAPM 2020. (Poster)
8. Y Jia, X Qi, **J Du**, R Chin, E McKenzie, K Sheng. A Deep Transfer Learning-Based Radiomics Model for Prediction of Local Recurrence in Laryngeal Cancer. AAPM 2020.

1.Introduction

1.1 Radiomics

"Images are more than pictures".[1] Medical images (CT, MRI, PET, etc.) contain far more information beyond the visual interpretation of human eyes that could support disease diagnosis and prognosis. Radiomics is one of the emerging research fields that aim to build machine learning-based predictive models using high-throughput quantitative features extracted from medical images[2] that are believed to reflect underlying pathophysiologic characteristics.

A typical Radiomics analysis process starts with the extraction of large numbers of quantitative features from the region of interest (ROI) of the medical images. Typically, hundreds or thousands of features are extracted, including a small number of semantic clinical features and a large amount of agnostic quantitative features such as Intensity-based features, shape features, texture features, transform-based features, radial features, and deep learning extracted features[3]. Then, feature selection is performed to remove irrelevant or redundant features. The reduced feature dimensionality permits higher learning efficiency and lower overfitting risks in the subsequent steps[4]. After selection, various machine learning algorithms are applied to analyze the features and establish a predictive model, such as support vector machine (SVM), random forest (RF), k-nearest neighbors (KNN), and neural networks (NN).

With the pioneering work of Aerts et al.[2], there has been an exponential growth in Radiomic publications since 2014, reporting tasks including treatment response and outcomes prediction[5], tumor staging[6], tissue identification[7] and assessment of cancer genetics[8]. Radiomics provides a non-invasive method to peek into tumor biology through radiologic images, providing complementary information that is otherwise unavailable for treatment decision-making. Radiomics using existing medical imaging information can be easily integrated into clinical workflow.

Despite the potential of Radiomics in personalized medicine, its application has been largely retrospective and non-interventional due to significant concerns about its reliability, accuracy, and interpretability. Radiomics is found to lack repeatability and reproducibility[9]. Balagurunathan et al. [10] found the majority of features unstable between even repeated lung cancer patient CT scans acquired only 15 minutes apart, not to mention features extracted from images obtained using different machines in different institutions. Guha et al.[11] identified several loopholes in Radiomics analysis for head and neck cancer response assessment, including the lack of reproducibility and consistency. These questions are related to the most fundamental challenge for Radiomics, which is the interpretability of the extracted features and the generated models[12]. Due to its data-driven nature, radiomics provides only correlation without causation, does not offer insights into the underpinning biology of observed relationships, and does not clinically interpret its decisions. Without overcoming these limitations, Radiomics would remain an academic exercise without influencing the course of patient treatment. There are attempts to tackle the interpretability issue by connecting radiomics to tumor biology[13]. For instance, correlations between cancer imaging features and certain gene expressions or gene mutations

were studied[14,15], as well as the correlations between imaging features and a specific histological substrate like microvascular density[16], and the correlations between tumor metabolism and radiomic features[17]. On the prediction model side, Yi Luo et al.[18] developed a Bayesian network to identify the hierarchical relationships among biophysical features for lung cancer radiotherapy local control prediction. Novel visualization methods that highlight regions of the tumor according to their importance for the prediction of the generated classifier have also been developed.[12,19] Although these studies improved our understanding of radiomic features and how prediction models work, they do not establish causality nor offer the mechanistic view of feature and prediction formation. Without such a causal relationship, the radiomic features are not truly interpretable, and the generality and robustness of extracted features are questionable, thus hindering Radiomics from being widely adopted as a reliable clinical component, particularly for interventional purposes.

In the era of personalized medicine, there is an urgent need to better understand Radiomics and the reflected physio-biological properties behind, or more essentially, to better understand the multiscale problem of how those key physio-biological microscopic tissue properties lead to the emergence of macroscopic tumor patterns or high-level features that can be captured in medical images. However, the direct connection between arbitrary genes or expressions and features can be overwhelmingly obstructed and complicated. One mutation could affect multiple aspects of tumor development, and one apparent physio-biological property or tumor feature may be controlled by multiple mutations. For example, oncogenes like MYC, RAS, BRAF, suppressor genes like TP53 and PTEN, and growth-factor-related genes like EGFR and HER2/neu may

share roles in the alteration of apparent tumor cell proliferation rate, while each of them also has other function in other aspects of tumor development[20–23].

For a clearer view of the pattern formation process, it can be roughly divided into two steps. The first step involves how genes and their expression affect the apparent physio-biological properties of various components in tumors at the molecular level. The second step is about how these apparent microscopic physio-biological properties of the tumor lead to macroscopic features or pattern formation as the tumor grows, which is a better-defined, physics-driven process. It is reasonable to believe that molecular alteration identifiable in medical images must first change the apparent property of tissue components to alter downstream macroscopic imaging features. Decoupling apparent tumor properties from their complex molecular backend is a necessary step for us to gain a clear and causal view of the feature development process.

The knowledge related to the first step can be acquired through in vitro or in vivo experiments. Recent advances in RNAseq, transcriptomics, and proteomics significantly facilitated the understanding of cell behaviors as a result of genetics[24]. However, our understanding of tumor cell development and organization into tumors that can be observed in macroscopic medical images remains highly limited. In this study, we propose to use physics-driven computational modeling to explore how the microscopically apparent tumor physio-biological properties can casually and mechanistically derive the observable macroscopic appearance that is interpreted as Radiomics. Computational modeling allows us to conduct clean variable control with arbitrary data samples in tumor development complementary to actual experiments that are more limited by scientific scopes and economic feasibility. Through mechanism and physics-based modeling,

the causality relationship between biological parameters and the tumor macroscopic features can be studied and established.

To achieve the goal, an ultra-large-scale computational tumor model emphasizing emergency tumor heterogeneity needs to be established.

1.2 Computational Oncology

Cancer represents a leading health threat globally, with a lifetime risk of one in four individuals and nearly half of these cases being fatal[25]At its core, cancer involves uncontrolled cell growth with the potential for metastasis and presents as an extremely complex and heterogeneous evolutionary phenomenon influenced by interplaying factors across subcellular, cellular, and tissue scales. The complexity of tumors can be rationalized through the eight hallmark traits and two enabling characteristics as delineated by D Hanahan et al.[26,27]. To better understand the complex physical, chemical, and biological processes in cancer development and treatment intervention, there has been an emerging interest in using computational models to study these multiscale processes, encompassed in a field called computational oncology, from subcellular level DNA synthesis, degradation or damage, cellular level signaling network[28] to tissue-level multicellular system development[29].

The computational models of multicellular cancer development can be generally divided into discrete, continuum, and hybrid models.

The discrete model is also known as the cell-based model[30]. Cell-based models simulate individual cells as they interact in virtual tissues, which allows us to explore how single-cell behaviors lead to the dynamics we observe and work to control in cancer systems. It can be further classified into Lattice-Based Methods and Off-Lattice methods depending on whether the agents are allowed to move freely in space. For lattice-based methods, there could be subcellular elements (Cellular Potts models (CPM)[31]), a single (cellular automaton (CA)[32]) or multiple cells (lattice gas cellular automaton (lattice gas CA (LGCA) [33]) in each lattice site. Lattice-base models suffer from grid biases[34], whereas the off-lattice method is free of such issues. Off-lattice models can be divided into Center-Based models (CBMs) and Boundary-tracking methods[30]. Center-based models track cell centers and enable a more realistic cell movement simulation by incorporating forces such as adhesive, repulsive, locomotive, and drag-like forces[29,35], meanwhile assuming a simple spherical shape of cells. Boundary-tracking models put more computational resources into the morphological characterization of the cells[36].

Different from the discrete or cell-based methods, continuum models represent the evolution of the tumor generally involving using partial differential equations, disregarding the behavior of each individual cell[37–39]. The most common type of continuum model is called diffusive models[40,41]. These models use the reaction-diffusion formalism to describe the change of tumor cell density: diffusion term to describe the invasion of tumor cells in the surrounding tissues and source term that describes the proliferation of tumor cells. The RD model is widely used due to

its simplicity and consistency with the biological tumor growth process[42]. One emerging type of diffusive model is phase-field[43,44] model that considers the tumor as a multiphase system and uses a phase field to model the tumor and normal tissue transition[45]. The interface between constituents can be characterized by a gradient term in the energy of the system and is handled automatically as a feature of the solution[37]. A general derivation of the continuum theory of mixtures with diffuse interfaces is provided in[37].

The hybrid models include both discrete and continuum components, combining the strength of heterogeneity characterizing the discrete component with the computation efficiency of the continuum tissue. Cell-based models usually also include a continuum of oxygen field[29] making it actually a hybrid model by definition, and the distinction between these two is usually blurred.

Computational simulations have been utilized to study various oncological topics[46], such as epithelial ducts and cysts through the epithelial acini models[47], the development of initial phases of avascular tumor development through multicellular tumor spheroid (MCS) models[48,49], angiogenesis and vascular network formation problems[50], and all major types of anti-cancer treatments effectiveness modeling[51,52]. However, computational simulation has not been used to explore the way macroscopic tumor textures and the underlying biological mechanisms are related.

1.3 Overview

Cancer is an evolutionary and ecological process[53], and cancer heterogeneity is a complex systems problem that involves interactions between cancer cells and tissue microenvironments.[30] Hypoxia is one common tumor microenvironment factor of all cancers where the oxygen demand of the intensively proliferating and expanding tumor tissue cannot be fulfilled by the enhanced but still unpaired angiogenesis process and the resulting limited blood perfusion and oxygen supply[54]. The oxygen level in normal organs varies from 4% to 10%, and the average level is about 5%[55]. While the oxygen level in tumors falls between approximately 0.3% to 4.2% and mostly showing median oxygen levels less than 2%[55]. The pathological hypoxic environment in the tumor could trigger metabolism transition, invasion mechanisms enhancement, the release of vascular endothelial growth factor (VEGF), or even the process of necrosis or apoptosis, with respective thresholds depending on the different sensitivity to oxygen conditions of each cell. Meanwhile, it is believed that the misshapen, irregular, disorganized, and tortuous architecture arising from tumor-induced angiogenesis eventually results in the formation of hypoxic voids, necrosis, and an acidic milieu, which are the basis for imaging tumor heterogeneity with CT[56]. Therefore, we believe that the interrelated angiogenesis and hypoxia mechanisms in tumors play an important role in driving the formation of macroscopic heterogeneities and texture patterns. Such an idea is supported by an empirical in vivo study where B Ganeshan et al.[57] showed that texture parameters derived from CT images of NSCLC have the potential to act as imaging correlates for tumor hypoxia and angiogenesis. For the

reasons above, we are going to focus on angiogenesis, blood perfusion, and oxygen supply during tumor development. Additionally, for the emergence of macroscopic heterogeneity, the size of the tumor needs to be sufficiently large, and high throughput modeling is needed for statistical analysis. These imposed a high requirement for both modeling efficiency and fidelity.

Given the pivotal roles of angiogenesis, blood perfusion, and oxygen supply in tumor growth and behavior, our study will concentrate on these critical aspects during tumor development. Besides, to adequately capture the emergence of macroscopic heterogeneity, the modeled tumors must reach a significant scale. Furthermore, comprehensive statistical analysis necessitates high-throughput modeling capabilities. Consequently, our approach must meet stringent requirements for both computational efficiency and model fidelity to accurately reflect the complex dynamics of tumor growth and vascular development.

Considering the crucial influence of angiogenesis, blood perfusion, and oxygen supply on tumor progression and characteristics, our research will focus intently on these aspects during tumor development. Moreover, to accurately represent the emergence of macroscopic heterogeneity our models must simulate tumors on a substantial scale. High-throughput modeling is also indispensable for conducting in-depth statistical analysis of the simulation results. These requirements necessitate a modeling framework that balances the demands of computational efficiency with the need for high fidelity to provide realistic and insightful representations of tumor biology.

In this dissertation, I will first introduce our work on large scale avascular cell-based modeling platform in Chapter 2. We highlight critical enhancements in modeling speed and memory

efficiency, crucial for facilitating comprehensive cell-based simulations. In Chapter 3, we explore the vasculature of both tumor and normal tissues, focusing on their morphology and functionality in relation to perfusion and oxygenation. Notably, our methods achieve real-time, coupled perfusion-oxygenation modeling at a scale representative of actual mice tumors and vasculature, marking a significant achievement. Chapter 4 is dedicated to our ultra-large physics-driven vascularized tumor model, which illuminates the mechanisms contributing to the formation of macroscopic tissue heterogeneity. Additionally, this chapter provides insights into how imaging features, extracted from the model analyzed with Radiomic approach, can be interpreted.

2.Chapter 1: Gell: A GPU-powered 3D hybrid simulator for large-scale multicellular system

As a powerful but computationally intensive method, cell-based hybrid computational models study the dynamics of multicellular systems by evolving discrete cells in reacting and diffusing extracellular microenvironments. As the scale and complexity of studied biological systems continuously increases, the exploding computational cost starts to limit large-scale cell-based simulations. In this chapter I will introduce our work on developing Gell: a fast and memory-efficient open-source GPU-based hybrid computational modeling platform for large-scale system modeling. We fully parallelize the simulations on GPU for high computational efficiency and propose a novel voxel sorting method to further accelerate the modeling of massive cell-cell mechanical interaction with negligible additional memory footprint. As a result, Gell efficiently handles simulations involving tens of millions of cells on a personal computer. We compare the performance of Gell with a state-of-the-art paralleled CPU-based simulator on a hanging droplet spheroid growth task and further demonstrate Gell with a ductal carcinoma *in situ* (DCIS) simulation. Gell affords ~150X acceleration over the paralleled CPU method with one-tenth of the memory requirement.

2.1 Introduction

Computational modeling has become an important tool for studying the dynamics of tissue development and tumor response to different therapeutic interventions over the past three decades. Three major types of models are commonly utilized in these studies: discrete, continuum, and hybrid models[32]. Discrete models, also known as cell-based models or agent-based models, simulate the individual behaviors and the mutual interactions of the cells in a system. Continuum models consider biological tissues as domains composed of different solid and fluid phases and describe the system evolution using partial differential equations. Hybrid models combine the aforementioned two methods as they model discrete cells in a continuum environment.

Cell-based and hybrid simulations adopt the discrete representation of the cell of interest. Compared to the continuum representation, the discrete modeling of individual cells better captures the heterogeneity of tumorous tissue with independently tracked cell states and enables a more straightforward translation from biological hypothesis to simulation rules[30]. Cell-based/hybrid simulation has been utilized to explore various kinds of oncological topics[46], such as epithelial ducts and cysts through the epithelial acini models[58] [47], the development of the initial phases of avascular tumor development through multicellular tumor spheroid (MCS) models[48], angiogenesis, vascular network formation problems[59], and anti-cancer treatments

effectiveness modeling[52] [51]. The method for discrete representation of cells can either be lattice-based or off-lattice. Lattice-based methods are mesh-based, including cellular automaton (CA) models[60], lattice gas CA (LGCA) models[61], and Cellular Potts models (CPM)[62]. Lattice-based models are susceptible to grid biases[34], which do not affect the off-lattice methods. Two major types of off-lattice models are Boundary-tracking models[36] and Center-Based models (CBMs)[32] [29]. Boundary-tracking models dedicate more computational resources to the cells' morphological dimension and are thus more computationally expensive than CBMs[30]. CBMs assume a spherical cell shape and represent cell movement by displacing the cell center position. Cell movements can be realistically modeled by incorporating forces such as adhesive, repulsive, locomotive, and drag-like forces[29]. Center-based representation is often a superior choice for large-scale cell-based/hybrid simulations interested in the heterogeneous development of biological tissue due to its realistic modeling of multicellular interactions and lower computational cost than other cell-based methods.

However, even with a center-based representation of discrete cells, as the scale and complexity of the studied biological systems continuously increase, the exploding computational cost still limits the large-scale cell-based/hybrid simulations. Several CPU-based cell-based/hybrid simulation software frameworks have been proposed to enable large-scale biological system modeling on high-performance computers. Biocellion[63], a closed-source commercial software, has simulated millions to billions of cells on computer cluster. PhysiCell[29] is an open-source parallel simulation platform capable of simulating 18.2 days of hanging drop spheroid growth with up to one million cells in 3 days on a high-performance computer. BioDynaMo[64] is another

open-source parallel simulator which is 945X faster on the 'epidemiology (medium-scale)' benchmark using 72 CPUs on a server compared to a single thread version. Because of the demonstrated potential to accelerate cell-based simulation with parallelization, recent research has shifted to the graphic processing unit (GPU), which has an intrinsic parallel architecture with thousands of computational cores. Ya||a[65] is a paralleled agent-based model on GPU. Its extended spheroid cell model with spin-like polarities can simulate epithelial sheets and tissue polarity. Although Ya||a[65] can achieve 10X acceleration compared to CPU-based cell-based simulation library Chaste[66], their simulation software is not designed for large systems. Simulation of large systems using Ya||a[65] is limited by its computational complexity of $O(N^2)$ for cell-cell interaction. CBMOS[67] is another GPU-based software that provides a platform to study the effects of force functions, ODE solvers, time step sizes, and cellular events in CBMs. CBMOS[67] utilizes fast GPU vector operations provided by CuPy for efficient calculations and achieves a simulation speed 30X faster than their CPU version. Their emphasis, however, is on a better user interface for fast prototyping of new models. Its ability to handle large systems is still limited by the platform design, e.g., the force calculation time complexity is $O(N^2)$ and the GPU memory consumption can exceed 16 GB (e.g., NVIDIA Tesla T4) for $>10^4$ cells. GPU BioDynaMo[68] upgrades BioDynaMo[69] by enabling GPU co-processing. With a GTX 1080Ti GPU, GPU BioDynaMo can be 130X faster than the single thread CPU only version BioDynaMo. However, GPU BioDynaMo does not solve PDEs on GPU, and its uniform grid method for force calculation still needs CPU for linked list maintenance, which significantly limits its real-world performance.

Therefore, although acceleration of cell simulation using GPU has been demonstrated, the potential has not been fully realized. Specifically, the cell-cell interaction has not been fully parallelized, and the slow data transfer between CPU and GPU results in significant overhead. In this study, we developed a new open-source fast and memory-efficient fully GPU-based hybrid simulation software, GPU cell (Gell), to overcome these bottlenecks for large-scale hybrid cell simulation.

2.2 Methods

2.2.1 Cell model

2.2.1.1 Cell Cycle and Death

We model five cell phases in Gell. The premitotic, postmitotic, and quiescent phases are for living cells, and the necrotic and apoptotic phases are for cell death. The phase transition from premitotic to postmitotic and from postmitotic to quiescent are deterministic with a fixed gap time, respectively. Meanwhile, the phase transition from the quiescent phase to the premitotic

phase and any phase transition from the living cell phase to the dead cell phase are all stochastic with a certain transition rate. The respective transition rates are listed in Table 2-1.

Transition Rate	Premitotic Phase	Postmitotic Phase	Quiescent Phase	Apoptotic Phase	Necrotic Phase
Premitotic Phase		$1/T_{prem}$	0	0	0
Postmitotic Phase	0		$1/T_{postm}$	0	0
Quiescent Phase	$r_{pro}(p_{oxy})$	0		r_{apop}	$r_{nec}(p_{oxy})$

Table 2-1 The phase transition rate in the cell cycle model from the left column phase to the top row phase. The transition rate for deterministic phase duration is noted as one over the fixed phase duration.

The probability for any stochastic transition α with transition rate r_a to take place in a short time interval Δt is given by:

$$Prob_{\alpha} = r_a \Delta t$$

Equation 2-1

During the quiescent phase, cells maintain their standard volume and remain to be stochastically activated for division preparation at the rate $r_{pro}(P_{oxy})$:

$$r_{pro}(P_{oxy}) = \begin{cases} r_{pro\_max} & P_{oxy} \geq Sa_{pro}, \\ r_{pro\_max}\dfrac{P_{oxy} - Th_{pro}}{Sa_{pro} - Th_{pro}} & Th_{pro} < P_{oxy} < Sa_{pro}, \\ 0 & P_{oxy} \leq Th_{pro}. \end{cases}$$

Equation 2-2

The proliferation rate increases linearly with local oxygen concentration in the given range $Th_{pro} < P_{oxy} < Sa_{pro}$, where Th_{pro} is the minimum oxygen partial pressure required for proliferation, Sa_{pro} is the saturation oxygen partial pressure when the transition rate for proliferation reaches the maximum value r_{pro_max}.

Once activated for proliferation, cells enter the premitotic phase and prepare for division. Premitotic cells gradually gain mass/volume, and then divide at the end of this phase and enter the postmitotic phase. The division process is mechanically modeled to finish in an instant, and the two daughter cells equally inherit half of the parent cell volume and be placed around the parent cell center with the displacement x_{disp}[29].

$$x_{disp} = \pm\left(R - \frac{R}{\sqrt[3]{2}}\right)\theta$$

Equation 2-3

Where R is the cell radius of the parent cell, and θ is a three-dimensional random unit vector. The postmitotic phase accounts for the duration required for daughter cells to reach mechanical equilibrium and grow to be proliferation ready.

Cell death is activated stochastically for all living cells. The transition rate to enter the apoptotic phase is a constant for all cells, r_{apop}, while the transition rate for necrotic death depends on the local oxygen partial pressure P_{oxy}:

$$r_{nec}(P_{oxy}) = \begin{cases} 0 & P_{oxy} \geq Th_{nec}, \\ r_{nec\_max}\dfrac{Th_{nec} - P_{oxy}}{Th_{nec} - Sa_{nec}} & Sa_{nec} < P_{oxy} < Th_{nec}, \\ r_{nec\_max} & P_{oxy} \leq Sa_{nec}. \end{cases}$$

Equation 2-4

Necrosis happens only when local oxygen partial pressure is lower than the necrosis threshold Th_{nec}. The transition rate increases linearly as the oxygen concentration decreases till the maximum necrosis rate r_{nec_max} is reached when oxygen partial pressure equals the necrosis saturation threshold Sa_{nec}.

All cell components start to shrink for apoptotic death upon entering the phase. While for the necrotic phase, early necrotic cells first absorb fluid and swell in the oncosis process, and then enter the late necrosis process after the membrane ruptures and start to lose fluid components. Modeling of two-stage necrotic death can be critical when studying the microstructures in the hanging drop spheroid necrotic center[29]. Phase transition-related parameters can be found in

Table 2, where the listed values are all adopted from the "Ki67 Advanced" model from PhysiCell[29].

Parameter	Biophysical meaning	Reference Value
T_{prem}	Duration of premitotic phase	13 $hour$
T_{postm}	Duration of postmitotic phase	2.5 $hour$
r_{apop}	Apoptosis rate	0.0060 $hour^{-1}$
r_{pro_max}	Max proliferation rate	0.1176 $hour^{-1}$
Sa_{pro}	The oxygen level when the proliferation rate reaches maximum	10 $mmHg$
Th_{pro}	The oxygen level when the proliferation rate drops to zero	5 $mmHg$
r_{nec_max}	Max necrosis rate	0.1667 $hour^{-1}$
Sa_{nec}	The oxygen level when the necrosis rate reaches maximum	2.5 $mmHg$
Th_{nec}	The oxygen level when the necrosis rate drops to zero	5 $mmHg$

Table 2-2 Phase transition-related parameters.

Following PhysiCell[29], we divide the total cell volume V into the fluid volume V_F and the solid biomass volume V_S. The solid biomass volume is further divided into total nuclear volume V_{NS} and cytoplasmatic volume V_{CS}. Different cell components have different rates of volume gain and loss in different phases. All the volume changes of different cell components are modeled using ordinary differential equations (ODEs):

$$\frac{dV_i(t)}{dt} = r_{p,i}\left(V_i(t) - V_i^p\right)$$

Equation 2-5

Where V_i is the volume of component i, $r_{p,i}$ is the volume change rate of component i in phase p, and V_i^p is the desired volume of component i in phase p. Specially, the desired fluid volume of a cell is a function of the current total cell volume V. Related parameters can be found in Table 3, adopted from MCF-10A human breast cancer cell line[29].

	Premitotic Phase	**Postmitotic Phase/ Quiescent Phase**	**Apoptotic Phase**	**Early Necrotic Phase**	**Late Necrotic Phase**
$\boldsymbol{V_F}$	$0.7502V$	$0.7502V$	$0\ um^3$	V	$0\ um^3$

r_F	3 $hour^{-1}$	3 $hour^{-1}$	3 $hour^{-1}$	0.67 $hour^{-1}$	0.05 $hour^{-1}$
V_{NS}	270 um^3	135 um^3	0 um^3	0 um^3	
r_{NS}	0.33 $hour^{-1}$	0.33 $hour^{-1}$	0.35 $hour^{-1}$	0.013 $hour^{-1}$	
V_{CS}	976 um^3	488 um^3	0 um^3	0 um^3	
r_{CS}	0.27 $hour^{-1}$	0.33 $hour^{-1}$	1 $hour^{-1}$	0.0032 $hour^{-1}$	

Table 2-3 Cell volume growth-related parameters.

2.2.1.2 Cell Mechanics

Cells in Gell are mechanically modeled as elastic balls with varied volumes and center positions. Cells adhere to each other while attached and push against each other upon compression. The motion of cell i at position $x_i(t)$, with velocity $v_i(t)$, and with a set $N_i(t)$ of nearby cells can be modeled as[29]:

$$m_i \dot{v}_i = \sum_{j \in N(i)} \left(F_{cca}^{ij} + F_{ccr}^{ij} \right) + F_{mot}^{i} - \eta_i v_i$$

Equation 2-6

Where $\dot{v}_i$ is the acceleration, F_{cca}^{ij} denotes the adhesive force from cell j to cell i, and F_{ccr}^{ij} represents the repulsive force from cell j to cell i. F_{mot}^{i} accounts for the force related to cell migration. $\eta_i v_i$ represents the resistance contributed by the local microenvironment, such as fluid resistance and cell-matrix adhesion forces. η_i is a fluid-drag-coefficient parameter and v_i is the cell velocity.

The force equilibrates at relatively short time scales relative to the time scale of cell volume change and multicellular patterning. Therefore, we can safely apply the zero acceleration inertialess condition to Eq (6) and explicitly solve v_i by:

$$v_i = \frac{1}{\eta_i}\left(\sum_{j\in N(i)}\left(F_{cca}^{ij} + F_{ccr}^{ij}\right) + F_{mot}^{i}\right)$$

Equation 2-7

The adhesive force and repulsive force experienced by cell i are modeled as:

$$F_{cca}^{ij} = \begin{cases} C_{cca}\left(1 - \frac{|r_{ij}|}{R_A}\right)^2 \frac{r_{ij}}{|r_{ij}|} & if\ \ |r| \le R_A, \\ 0 & otherwise. \end{cases}$$

Equation 2-8

$$F_{ccr}^{ij} = \begin{cases} -C_{ccr}\left(1 - \frac{|r_{ij}|}{R_R}\right)^2 \frac{r_{ij}}{|r_{ij}|} & if\ |r| \le R_R, \\ 0 & otherwise. \end{cases}$$

Equation 2-9

R_R is the maximum repulsive interaction distance that equals the sum of the radius of cell i and j. R_A is the maximum adhesive interaction distance, which is slightly larger than R_R due to the deformability of the two cells. C_{cca} is the cell-cell adhesion parameter and C_{ccr} is the cell-cell repulsion parameter. r_{ij} is a vector pointing from the center of cell i to the center of cell j.

Once the sum of the experienced force is calculated for all cells, the velocity of any cell can be directly calculated. Cell position is then updated using the second-order Adam-Bashforth method:

$$x_i(t + \Delta t) = x_i(t) + \frac{\Delta t}{2}\left(3 \cdot v_i(t) - v_i(t - \Delta t)\right)$$

Equation 2-10

2.2.2 Extracellular microenvironment

The tumor is surrounded by a complex ecosystem named tumor microenvironment (TME), composed of tumor cells, stromal cells, and other extracellular physical and chemical factors. The mutual and dynamic crosstalk between the tumor and tumor microenvironment, together

with the genetic/epigenetic change in tumor cells, are two factors that influence the formation and progression of the tumor[70]. In our model, cells can absorb environmental nutrients and release biochemical factors into the extracellular fluid. In addition, critical environmental factors can also regulate cell behaviors. To simulate the spatio-temporal variation of environmental factors during tumor development, we consider a continuous extracellular fluid space and use PDEs to describe the secretion, diffusion, uptake, and decay of diffusive substances such as oxygen and vascular endothelial growth factor. The continuum environment and the discrete cells are explicitly linked. Cell phases, sizes, and positions are treated as static while updating the continuous molecular space and vice versa. The equation for any diffusive substance in the extracellular fluid domain Ω can be written as[71]

$$\frac{\partial \rho}{\partial t} = \nabla \cdot (D \nabla \rho) - \lambda \rho + S(\rho^* - \rho) - U\rho$$

Equation 2-11

Depending on the problem, the domain boundary $\partial\Omega$ can be either Dirichlet or Neumann type. ρ is the substance concentration, ρ^* is the saturation concentration, D is the diffusion coefficient, λ is the decay rate, S is the supply rate, U is the uptake rate.

In the provided code, the oxygen concentration is the only considered environmental factor and discrete cells are the only contributor of oxygen consumption. Cells absorb oxygen from the extracellular fluid and regulate their behavior according to local oxygen concentration. The oxygen consumption of each cell is modeled as proportional to both the oxygen concentration

and the cell volume. With a cartesian grid, for each isotropic voxel i, the total uptake rate of oxygen equals the sum of the local cell consumption:

$$U_i = \sum_{j\ in\ i} \frac{V_j}{V_{voxel}} U_o$$

Equation 2-12

The uptake rate here represents the oxygen concentration decrease rate as a proportion of current concentration, U_o is the default oxygen consumption rate of living cells that equals 10 per min. V_{voxel} is the volume of the given voxel, j is the index of cells inside the voxel, and V_j is the corresponding cell volume.

In the simulation, each voxel's total oxygen consumption rate is first calculated according to the position, size, and phase of all the cells. Then the molecular space is updated using the static consumption rate map. With the calculated molecular concentration, cells in the discrete model could read the local oxygen concentration and carry on their stochastic phase transitions according to these values.

For the numerical processing of the PDE, following BioFVM[71], a first-order splitting method is first applied to split the righthand side into simpler operators: a supply and uptake operator and a diffusion-decay operator.

$$\begin{cases} \dfrac{\sigma-\rho^{n}}{\Delta t}=\nabla\cdot(D\nabla\sigma)-\lambda\sigma \\ \dfrac{\rho^{n+1}-\sigma}{\Delta t}=S(\rho^{n+1}-\sigma)-U\sigma \end{cases}$$

Equation 2-13

The supply and uptake operators are handled analytically. The three-dimensional diffusion-decay operator is further split into a series of related one-dimensional PDEs using the locally-one dimensional (LOD) method.

$$\begin{cases} \dfrac{\eta-\rho^{n}}{\Delta t}=\partial_x(D\partial_x\eta)-\dfrac{1}{3}\lambda\eta \\ \dfrac{\eta^{*}-\eta}{\Delta t}=\partial_y\left(D\partial_y\eta^{*}\right)-\dfrac{1}{3}\lambda\eta^{*} \\ \dfrac{\sigma-\eta^{*}}{\Delta t}=\partial_z(D\partial_z\sigma)-\dfrac{1}{3}\lambda\sigma \end{cases}$$

Equation 2-14

Discretized using the finite volume method, the updated concentration of each strip of voxels for each direction can be obtained by solving Eq (15) using the Thomas algorithm[72].

$$\begin{cases} \left(1+\dfrac{1}{3}\Delta t\lambda+\dfrac{\Delta t}{\Delta x^{2}}D\right)\circ\eta_{(0,y_f,z_f)}-\dfrac{\Delta t}{\Delta x^{2}}D\circ\eta_{(1,y_f,z_f)} & =\rho^{n}_{(0,y_f,z_f)} \\ -\dfrac{\Delta t}{\Delta x^{2}}D\circ\eta_{(n_x-1,y_f,z_f)}+\left(1+\dfrac{1}{3}\Delta t\lambda+2\dfrac{\Delta t}{\Delta x^{2}}D\right)\circ\eta_{(n_x,y_f,z_f)}-\dfrac{\Delta t}{\Delta x^{2}}D\circ\eta_{(n_x+1,y_f,z_f)} & =\rho^{n}_{(n_x,y_f,z_f)} \\ -\dfrac{\Delta t}{\Delta x^{2}}D\circ\eta_{(N_x-2,y_f,z_f)}+\left(1+\dfrac{1}{3}\Delta t\lambda+\dfrac{\Delta t}{\Delta x^{2}}D\right)\circ\eta_{(N_x-1,y_f,z_f)} & =\rho^{n}_{(N_x-1,y_f,z_f)} \end{cases}$$

Equation 2-15

2.2.3 Implementation Details

Gell is developed using C++ and CUDA (v11.2) with the program's design schematic illustrated in Figure 1. There are two major types of data in the simulation, the pre-allocated array of structure for cell data management and the isotopically discretized cartesian grid for spatial domain-related data, which includes information related to the tumor microenvironment (TME) and our Voxel Sorting (VS) method. Once initialized on the CPU, all the cellular and microenvironmental data are transferred to GPU memory. From this point, all the following computation steps are exclusively handled by GPU to eliminate costly back-and-forth data transfer between GPU and CPU.

2.2.3.1 Main Loop

The main simulation loop of Gell consists of three critical computational modules as delineated in dashed lines in Figure 1: the Microenvironment Module, the Cell Cycle Module, and the Cell Mechanics Module. Each module is responsible for one of the key tasks in the hybrid cell-based simulation and is uniquely designed to enable efficient parallelization on the GPU. Further details on this these modules will be explored in the following sections.

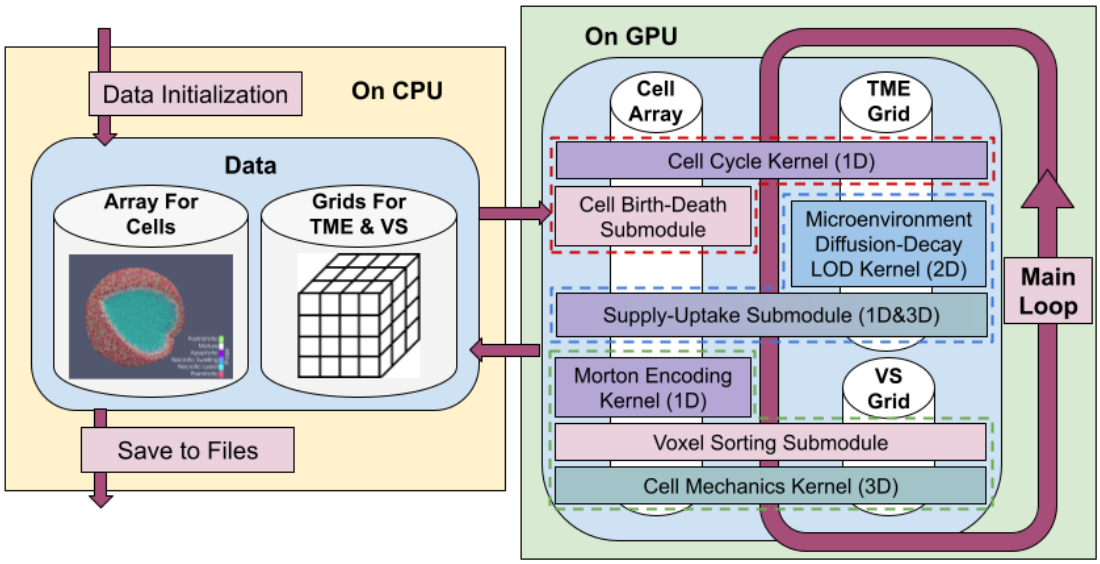

Figure 2-1 Diagram for the program design. In the provided diagram, white cylinders symbolize the simulation data, and colored boxes positioned atop this data represent associated operations. The abbreviations TME and VS are used to denote the Tumor Microenvironment and Voxel Sorting, respectively. The Microenvironment Module, Cell Cycle Module, and Cell Mechanics Module are distinctly demarcated with dashed lines in blue, red, and green, respectively.

2.2.3.2 Microenvironment Module

The Microenvironment Module is tasked with managing the diffusive transportation and cellular secretion/uptake of environmental factors, such as oxygen. This module is divided into two sections: a Supply-Uptake Submodule and a Diffusion-Decay LOD Kernel.

The Supply-Uptake Submodule deals with the supply and uptake of microenvironmental factors. This process involves two CUDA kernels: a 1D kernel parallelized over the cells to calculate the total supply and uptake in each voxel, followed by a 3D kernel parallelized over voxels to adjust the factor concentration after supply and uptake.

The Diffusion-Decay LOD Kernel uses the LOD algorithm to address the diffusion and decay of environmental factors. During each diffusion-reaction step, the LOD solver transforms the concentration update problem along the three axes into $3*N^2$ tridiagonal linear systems, each with N unknowns. Each parallel thread solves one of these tridiagonal linear systems using the Thomas algorithm. The overall computational complexity of each update step is $O(N_{voxel})$.

2.2.3.3 Cell Cycle Update

The Cell Cycle Module is responsible for managing cell proliferation, growth, and death. It is divided into two components, the cell cycle kernel, and the cell birth-death submodule.

The cell growth and phase transition only involve the current cell status as well as the local environmental factors. These processes are highly parallelizable and are directly distributed across different threads and computed by GPU in the Cell Cycle Kernel. The Cell Birth-Death Submodule manages cell proliferation and death, focusing on memory management of structured data. By leveraging this submodule, fast simulations can be conducted with only minimal additional computation and memory cost for thread competition avoidance. During cell

proliferation, the total cell count is atomically updated to enable the addition of new daughter cells to the cell array. For cell death, cells earmarked for removal are initially labeled in their respective phase update thread, and then collectively deleted from the cell array in a subsequent kernel for efficient cell array maintenance. The overall computational complexity of the above-mentioned processes is approximately O(N).

2.2.3.4 Cell Mechanics Update

N-body interaction simulations can be extremely expensive due to its $O(N_{cell}^2)$ computational complexity. For a large multicellular system with millions of cells, it is computationally impractical just to loop over all the cell pairs, even with GPU[65,67]. Fortunately, the cell-cell mechanical interactions are short-range interactions, making it reasonable to calculate only the forces between neighboring cells, thus reducing the computational complexity to $O(N_{cell})$. PhysiCell utilizes the cell-cell interaction data structure (IDS) method[29]. A large number of lists are created and maintained to record the indices of cells inside each voxel. The force calculation for each cell only has to loop over the cells inside its nearest 27 voxels, according to the lists. GPU BioDynaMo, with its uniform grid method[68], improves memory usage efficiency by replacing the cell index list with the linked list. However, maintaining such cell lists or linked lists is not GPU friendly. GPU does not allow us to dynamically allocate memory in the thread, making it challenging to create lists with dynamic lengths for all mechanical voxels in the IDS method. Suppose GPU memory for cell lists is all pre-allocated according to the maximum cell

density. In that case, memory usage can be highly inefficient due to the high cell density necrotic region. The challenge lies in the maintenance of the linked list for the uniform grid method on GPU. Thread locks are required to update the linked list correctly, but the wrapping mechanism of CUDA could easily create deadlocks during such processes and pause the program indefinitely.

To realize an efficient cell-cell mechanics computation on GPU, we have developed our Voxel-Sorting Method. Cells are stored in array-of-structures, and a Morton code is generated for each cell according to the i, j, k index of its containing mechanical voxel as a key for sorting. Then a fast GPU-based radix sort algorithm[73] of complexity $O(N_{cell})$ is used to rearrange the cell array according to the ascending Morton code value order. After sorting, cells in the same voxel are stored contiguously in the GPU memory, and cells in adjacent voxels are stored relatively close. Such a contiguous memory layout increases the memory fetch efficiency, especially when groups of cells in the same voxel have to be accessed together by the same thread. The array index range for cells inside each voxel is easily determined with $O(N_{voxel})$. Figure 2 illustrates the voxel sorting method in a 2D scene.

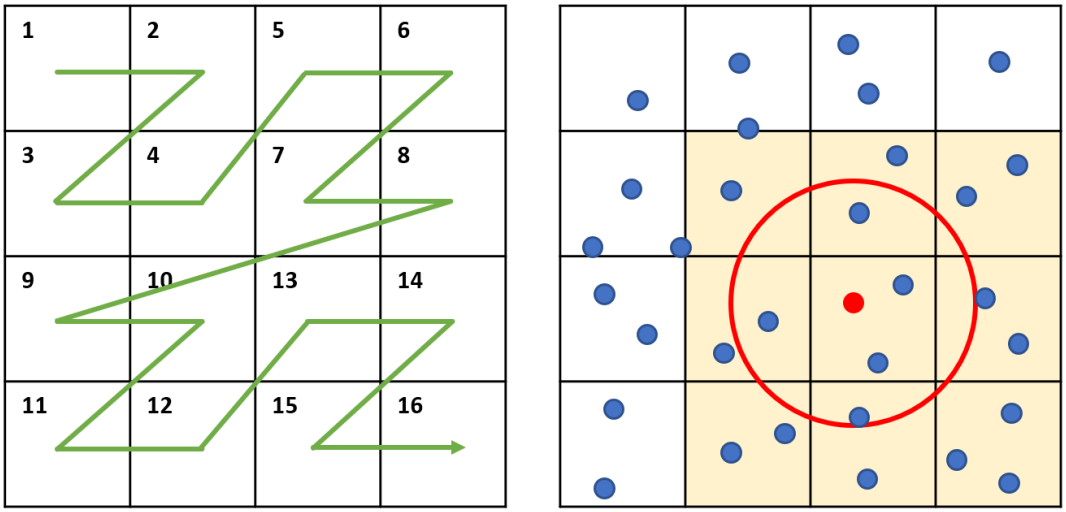

Figure 2-2 2D illustrations of voxel sorting method.

Left: The Morton code maps 2D position to 1D number while preserving the locality of the data points. The Morton code is generated by interleaving the binary x and y pixel index values. Adapted from[74]. Right: The force calculation example of a single cell(red). The red circle represents the maximum range of cell-cell mechanical interaction whose radius is shorter than the side length of voxels. The Force module only needs to loop over the cells in yellow voxels to calculate the aggregated force, and the indexes of cells inside these voxels can be easily figured out after sorting. As long as the voxel side length is longer than the maximum cell-cell interaction distance, each cell's aggregated cell-cell mechanical interaction can be calculated efficiently by looping only over cells inside its nearest 27 voxels. Our voxel sorting method achieved force calculation time complexity of $O(N_{cell})$ and high GPU memory utilization efficiency. An additional advantage of our voxel sorting method is memory access efficiency. With the cells in the same voxel stored next to each other in the GPU memory after voxel sorting, the following 27 times of memory fetch of these cell data can become much more

efficient than fully random memory access. After the force calculation, the cell position update can be directly parallelized using the aggregated force information.

This rapid cell-cell interaction simulation method described above is implemented in the three-step Cell Mechanics Module. The first Morton Encoding kernel determines the order index of each cell. Then the second Voxel Sorting Submodule sorts the cells accordingly and determines the index range of cells within each voxel. In the last step, the aggregated force and cell movements of each cell is calculated by the Cell Mechanics Submodule.

2.2.3.5 Time Scale Considerations

Different biological processes evolve at different time scales: the temporal scale of cell colony biology and mechanics is on the order of minutes, while the equilibrium of transport diffusion is achieved in seconds[29]. Because the extracellular environment updates substantially faster than cellular evolution, it is computationally inefficient to synchronize the cell simulator and extracellular environment simulator updates. Instead, we first fixed cellular properties while solving the PDEs for the extracellular environment at a higher frequency and then evolved cell phenotype and mechanical interaction at a lower frequency to reduce the simulation cost.

2.3 Results

All calculations are tested on a personal computer (with Intel® Core™ i7-7700K CPU, 64GB memory, and a NVIDIA® GeForce® RTX 2080Ti graphics card) on 64-bit Windows 10. Tests are conducted to determine the optimal block size settings for GPU computation during the program development, which have been fixed for later simulations. Specifically, the kernels for cell cycle update have a 1D block width of 64, while the 3D kernels for oxygen consumption employ a block width of 4. As for the 2D kernels used for LOD calculation, we have adopted a small 2D block width of 4 due to the storage requirements of the Thomas algorithm on GPU. This algorithm necessitates the storage of a temporary array for each thread, and a small block size allows us to store all data on the registers.

2.3.1 Hanging Drop Spheroid

As an *in vitro* 3D multicellular model, multicellular tumor spheroids (MCTS) possess many *in vivo* tumor features, including cell-cell interaction, hypoxia, treatment response, and production of extracellular matrix[75,76]. Tumor spheroids are widely used for various tumor growth dynamics and treatment response studies. Many modeling works have been published to bridge the observed spheroid experiment results to mechanistic understandings mathematically. Joshua A.

Bull et al.[77] developed an off-lattice hybrid spheroid growth model to explore the growth dynamics of tumor spheroids and reproduced the migration and internalization of tumor cells observed in spheroid experiments[78]. Kevin O. Hicks et al.[79] developed an on-lattice hybrid spheroid model using experimentally determined parameters and accurately simulated the cell killing after radiation and hypoxia-activated prodrug interventions.

To compare the computational performance of our simulation framework with existing simulation software, we simulated a benchmark problem of hanging drop spheroid growth[29]. In the hanging drop spheroid (HDS) benchmark, a suspended multicellular aggregate is cultured in the middle of a growth medium with oxygen supplied through diffusion from the domain boundary. All the Gell simulations and PhysiCell simulations share identical simulation settings. The simulation started with 2347 cells and evolved to nearly one million cells after 450 hours of cultivation. The simulation domain contains one million isotropic voxels with a side length of 25 μm. Cell mechanics and phase update is calculated every 0.1 minutes, and the diffusion-reaction of oxygen in the extracellular fluid is solved every 0.01 minutes. At the end of the simulation, Gell and PhysiCell produce nearly identical results, predicting a spheroid radius of 1.87 mm and evolving visually identical spheroid structures, including the crack patterns in the necrotic cores. These findings suggest that the computation of Gell is accurate, and the use of single precision arithmetic has a negligible impact on the simulation result. The evolution of cell numbers and spheroid radius over time is shown in Figure 3. The result shows no necrosis development until the spheroid reaches a certain radius when oxygen diffusion from the outer rim becomes insufficient to support the inner cells. The radius growth curve exhibits a linear shape due to the

approximately constant viable rim thickness, which agrees with the simulation result and theoretical prediction of PhysiCell[29].

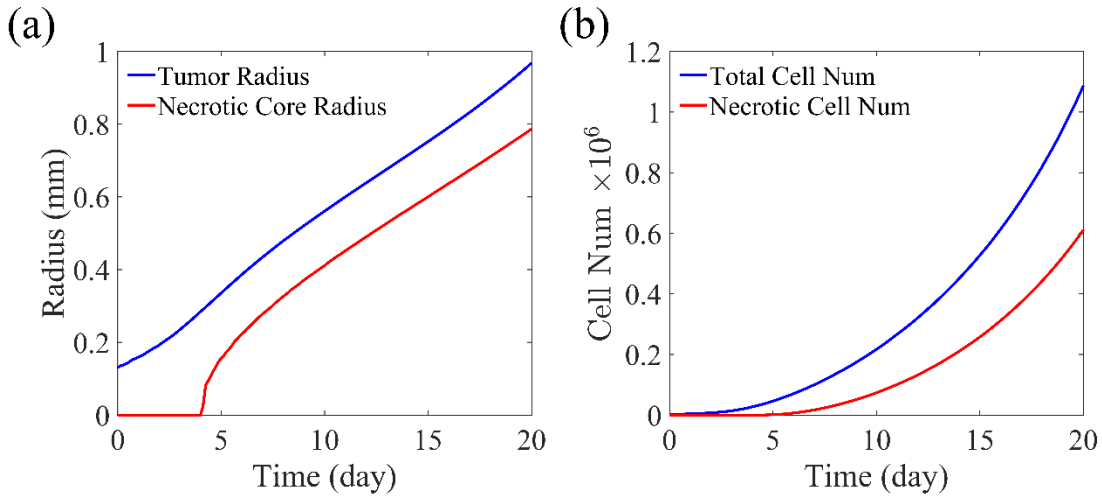

Figure 2-3 Simulation result analysis of Gell. (a) Whole tumor radius and necrotic core radius change over the HDS growth. (b) Number change of total tumor cells and necrotic tumor cells over the HDS growth.

The rendered images of the simulation results are shown in Figure 2-4. There is a clear viable rim of actively proliferating cells at the outer shell of the spheroid and a necrotic core in the center (Figure 2-4. a). Additionally, the subtle cell-cell mechanical adhesion, crack like microstructures successfully emerged in the necrotic core enter. The simulation results of Gell agree with PhysiCell and *in vitro* experiments[29].

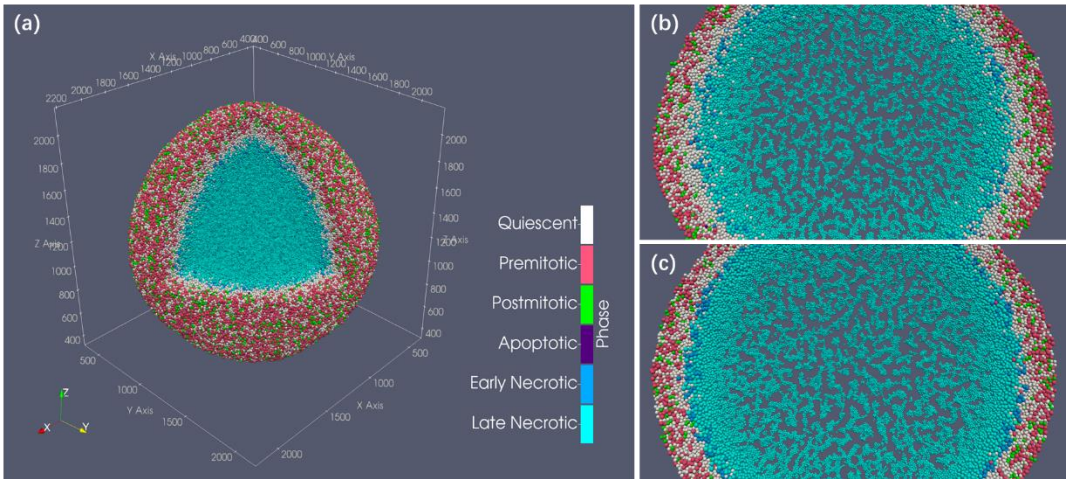

Figure 2-4 HDS simulation result after 450 hours. (a) Cell cluster generated by Gell. (b) 60 μm thick central slice of the HDS simulation result shows the microstructure of the necrotic core of Gell simulation. (c) central slice of PhysiCell showing identical microstructure. Both spheroids have a radius of 1.87 mm.

Gell completed the entire simulation process in 47 minutes using the personal computer. As a comparison, the state-of-the-art CPU-based parallelled simulator PhysiCell used 119 hours for the same simulation on the same personal computer. In other words, Gell is 150X faster for the cell simulation problem of this scale.

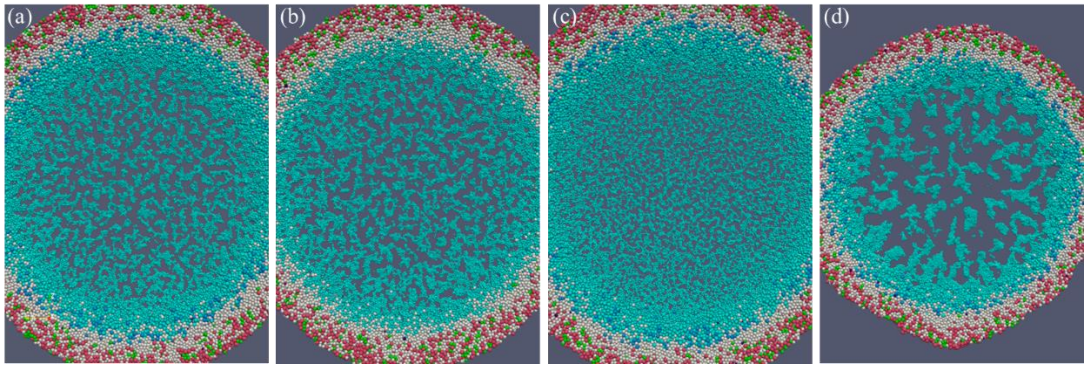

Figure 2-5 HDS simulation with altered phenotype. The 60-um thick central slices of simulated spheroids with various cellular mechanical properties. All the spheroids start with a small cluster of 2347 randomly placed cells, and the cultivation duration is 450 hours. (a) The reference spheroid ends up with 0.9 million cells and a diameter of 1.87 mm. (b) Spheroid of tumor cells with no swelling during early necrosis, with 0.9 million cells and a diameter of 1.8 mm. (c) Spheroid of tumor cells with the cell-cell adhesion suppressed, with 1.0 million cells and a diameter of 1.97 mm. (d) Spheroid of tumor cells with the cell-cell adhesion enhanced, with 0.66 million cells and a diameter of 1.53 mm.

Benefiting from the accelerated computation, we were able to explore the parameter space without agonizing pain. We surprisingly found that the crack pattern of the necrotic core has little to do with the two-stage necrosis process of tumor cells. The central slice of the spheroid of non-swelling tumor cells shows almost identical microstructure patterns (Figure 2-5.b). However, this system ends up with a slightly smaller size, fewer cells, and a higher overall necrotic debris density. This suggests that the swelling process of tumor cells could facilitate spheroid growth by pushing the viable cells towards the more oxygenated outer regions. Figure 5.c shows the spheroid of tumor cells with the cell-cell adhesion suppressed. The cell-cell adhesion factor C_{cca}

is decreased to one-fourth of the reference value. The weak adhesion discourages the gathering of necrotic cells leading to a more scattered distribution of smaller necrotic cell clusters with more minor interleaving cracks. Figure 5.d is a spheroid with the cell-cell adhesion enhanced by quadrupling Ccca. The strong adhesive force helps form the massive necrotic debris clusters and promotes a significantly higher cell density that intensifies the oxygen competition between tumor cells and ultimately hinders tumor growth. Such pattern differences in necrotic core microstructures that emerged in the simulation are also observed in *in vitro* experiments [80], as shown in Figure 6. Two spheroids of the same melanoma cell line (A2508) form clustered (Figure 2-6.a) and scattered (Figure 2-6.b) necrotic cores, respectively. The exact differences in cell treatment and mechanisms of pattern formation are not described in the original literature. However, our simulations hint that cell-cell adhesion could be an important factor that dramatically affects the spheroid morphology, especially the necrotic core microstructure.

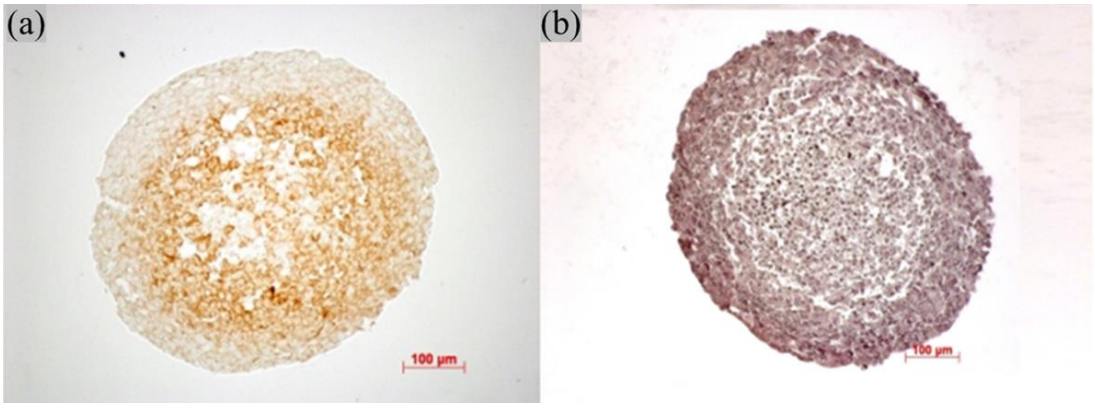

Figure 2-6 Melanoma cell line spheroids. Two spheroids of the same melanoma cell line (A2508) show distinct pattern differences in necrotic core microstructures due to differences in cell

treatment. Images are adapted from [33], and treatment details are not mentioned in the original literature. (a) A pimonidazole stained spheroid. (b) A Hematoxylin and eosin stained spheroid. Adapted from [33] with permission.

Simulations have the potential to depict a causal and mechanistic path from certain microscopic cell properties to the development of qualitative macroscopic morphology and provide insights into real-world phenomena. However, it can be very time-consuming to explore the parameter space and to improve the models iteratively. Gell could help these studies by dramatically increasing the computational speed.

Besides the baseline HDS simulation task, further comparisons of simulation performance with varying initialized cell numbers (Figure 2-7.a) and domain sizes (Figure 2-7.b) suggest that Gell is consistently around two orders of magnitude faster than multi-thread PhysiCell on the personal computer. For serial PhysiCell using only one thread, Gell can be almost 400x faster (Figure 2-7.c). The default simulation setting for the performance comparison contains one million 25×25×25 μm isotropic voxels and one million living cells. Cells are randomly initialized in a sphere with a specific cell density. The acceleration ratios of these tests differ from the whole HDS simulation because the HDS simulation has a more heterogeneous cell distribution and is closer to the equilibrium states after prolonged mechanical interactions.

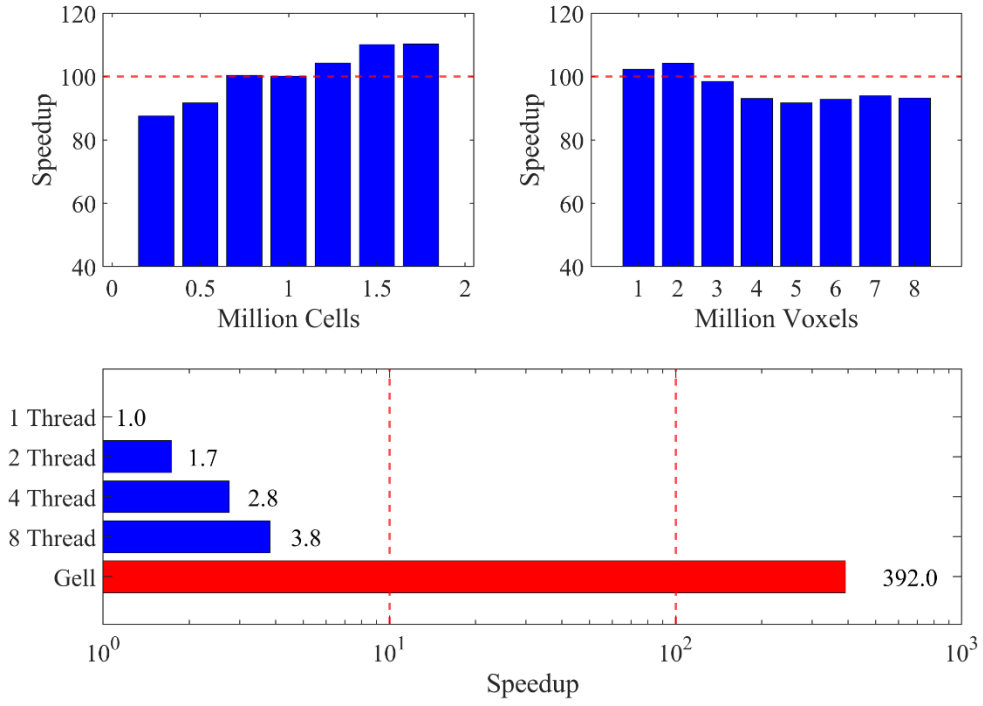

Figure 2-7 Gell simulation speedup with respect to PhysiCell. Gell simulation speedup with respect to PhysiCell with varied cell numbers (a), domain voxel numbers (b), and PhysiCell CPU thread numbers (c with logarithmic x scale).

Additionally, Gell can complete the simulation with its maximum memory footprint being only one-tenth of that of PhysiCell's without sacrificing accuracy and system complexity (Table 2-4).

	PhysiCell	**Gell**
Memory Footprint of HDS Simulation (MB)	6360	500

Memory Footprint per Additional Million Cells (MB)	5384.2	118.0
Memory Footprint per Additional Million Voxels (MB)	742.8	15.38

Table 2-4 Memory footprint comparison. Memory footprint comparison of Gell and PhysiCell per additional million cells and per additional million domain voxels in the HDS simulation task. Our model is able to simulate the problem with a much lower memory occupation.

2.3.2 Ductal Carcinoma in Situ

Ductal carcinoma in situ (DCIS) is non-invasive breast cancer that grows within the lumens of the mammary duct[81]. DCIS itself is not hard to treat, but as a precursor to invasive ductal carcinoma with a high incidence rate (26.6 per 100000 women[82]), its development and progression raise the interest of many modelers[35 83 84 85 86]. Following the work of Paul Macklin (30), we created a hybrid DCIS simulation example to further illustrate Gell with a more complex task. A cluster of tumor cells is placed at the dead-end of a fixed single-opening duct. The movement of tumor cells is confined within the tube lumen, and the oxygen is supplied through diffusion across the duct wall into the lumen. Breast ducts have a typical radius ranging

from 100 μm to 200 μm [84]; therefore, we simulated three growth scenarios of ductal carcinomas in situ with the respective duct radius of 100 μm, 150 μm, and 200 μm.

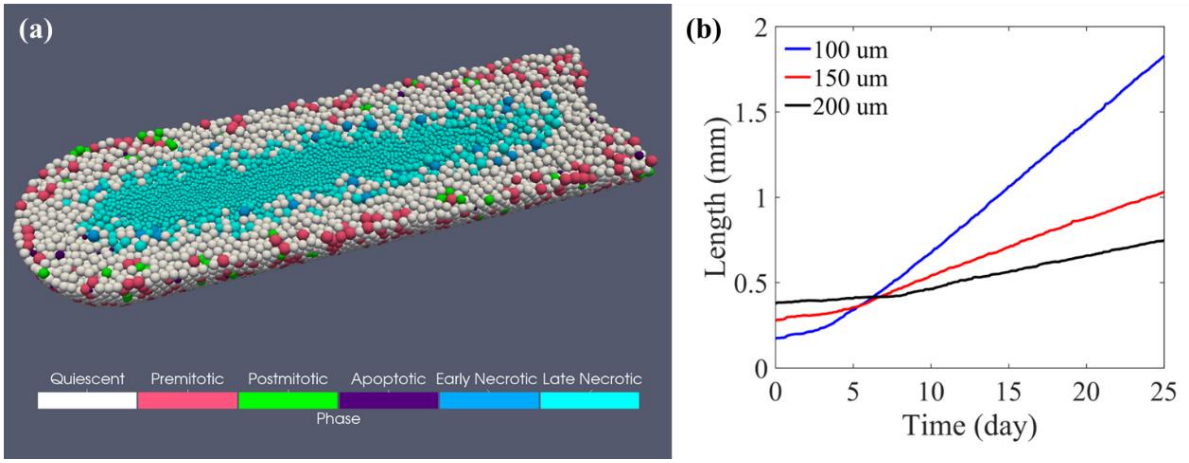

Figure 2-8 Simulation results of DCIS development. (a) Ductal carcinoma in situ simulation with duct radius of 150 μm. (b) Linear DCIS growth under various duct radius conditions.

With the same cell model as in the HDS simulation and a Dirichlet boundary condition of 7.2 mmHg oxygen concentration applied to the duct surface, the average rate of DCIS advance for ducts of radius 100, 150, and 200 μm is 77.0, 32.7, 19.0 μm/day, respectively. Our simulation results show a linear growth speed of DCIS, and the tumor advance rate has an inverse relationship with the duct radius, which agrees with the clinical observations and other computational studies in 2D[35] or 3D[87].

2.3.3 Performance Testing

2.3.3.1 Individual Module Time Cost

For performance assessment, we first evaluated our simulator with a randomly initiated spherical cell cluster with one million cells. The simulation domain contains one million 25 μm-long isotropic voxels. The time cost of each module is listed in Table 5. With the entire calculation paralleled on GPU, Gell maximizes computational efficiency in all the simulation modules. Meanwhile, unnecessary data transfer between CPU and GPU during the simulation is eliminated, ensuring a low delay between modules.

Module	Time cost per invocation
Morton code calculation	0.303 ms
Cell sorting	6.041 ms
Force calculation	3.613 ms
Cell movement	0.360 ms
Reaction-diffusion update	0.542 ms

Phase update with birth and death	4.744 ms
Memory copy between CPU and GPU	0.011 ns
Others	0.387 ms

Table 2-5 The execution time cost of each simulation module in Gell. Values are averaged over 1000 simulation steps with the time step for phase update, mechanics update, and diffusion-reaction update all set to be the same. Short time such as the time cost of memory copy during a simulation, is estimated by comparing a 1000-step simulation with another 2000-step simulation. The time cost for initialization and data saving is omitted.

In the table, the cell-sorting-related process appears to be slow, but in practice, its impact on the overall computation is small. Firstly, the cell sorting module is less invocated than many other modules. The simulation faces a multiscale problem. The cell phase is updated every few simulation minutes, cell motion is updated every few seconds, and the diffusion reaction of oxygen is updated more than once per second. In this case, the simulation is approximately equally dominated by the cell-motion-related modules and the diffusion-reaction model. Secondly, the sorting process accelerates the rest of the calculations. Take the oxygen consumption model as an example. This kernel is a part of the reaction-diffusion module that calculates each cell's oxygen consumption rate and adds the value to the total consumption rate of each corresponding voxel. This kernel works with both unsorted and sorted cell structures. Changing from unsorted random memory access to sorted contiguous memory access, this module's time cost per invocation is reduced from 0.345 ms to 0.170 ms by 51%. The force calculation module is expected to benefit most from the high data fetch efficiency of the voxel

sorting method. Because force calculation does not work with unsorted data structures, the speed comparison cannot be performed. Nevertheless, the longer time spent on cell sorting benefits the overall computation and is a worthy investment.

2.3.3.2 Performance Scaling

Unaffordable memory occupation is another potential barrier for large-scale cell-based simulations. Memory efficiency is another design goal to make Gell a suitable software for large-scale simulations on widely available devices. The GPU memory footprint of the HDS simulation with one million voxels and one million cells is limited to 500 MB, and the memory occupation increases with the cell number and domain size is linear and slow, as shown in Table 5. This enables Gell to fit extremely large-scale problems into a modern personal computer easily.

We tested Gell's ability to handle ultra-large-scale problems with a hypothetical ultra-large spheroid model. In reality, the size of hanging droplets is diffusion constrained. Larger *in vivo* tumors inevitably involve angiogenesis and supporting tumor vasculature. However, angiogenesis and oxygen transportation simulations are beyond the scope of the current work. Instead, we simulate a series of hypothetical huge hanging droplet development problems in a huge domain with varying initial cell numbers, each for one hour. As shown in Figure 9, Gell has a linear computational cost scaling with the cell number. Simultaneously, the Gell GPU memory

footprint peaked at 4392 MB, showing high efficiency in memory and computational source usage. This linear time complexity and low memory occupation demonstrate that Gell can handle potential ultra-large-scale problems.

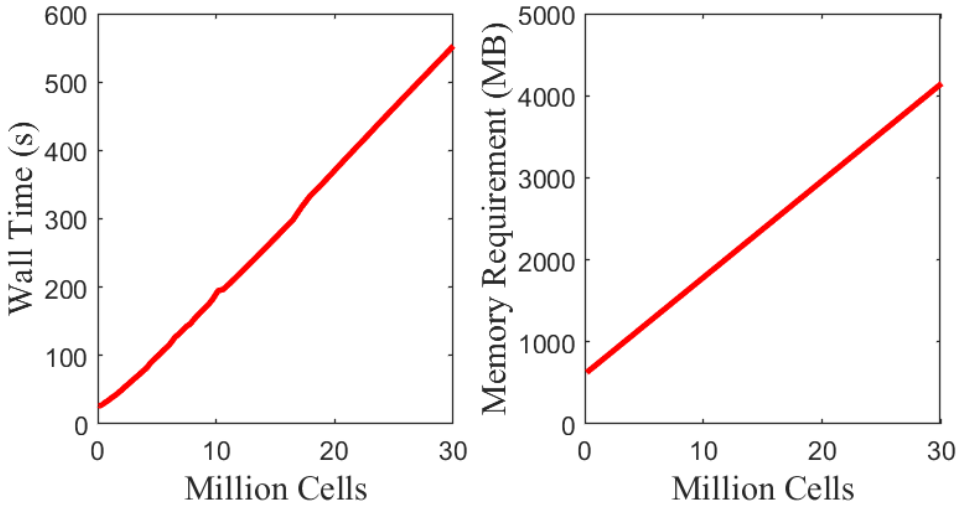

Figure 2-9 Performance scaling of Gell. Time and memory cost for one hour's mechano-biological process simulation with varying cell numbers. The domain contains 250×250×250 25 μm-long isotropic voxels.

2.4 Discussion

Cell simulation is driven by the need to model larger and more complex digital tumors parallel to human tumors containing billions of cells. Simulation of such complex systems has been limited by the modeling accuracy of the biology and computational capacities. Existing tools such as

Biocellion[63] for such large-scale simulations are close-sourced and require expensive CPU clusters. Open source tools, including PhysiCell [29] and BioDynaMo [64] require high-end CPU clusters to perform computation in practical time. In theory, GPU is well suited to manage the large parallel components of cell simulation. However, due to the differences between GPU and CPU architecture, a direct translation of a CPU-based cell simulation code to a GPU-based one is not straightforward and can be inefficient. Specifically, global cell-cell interactions have a time complexity of $O(N^2)$. The non-linear computational cost severely limits the number of cells that can be modeled and, subsequently, the size and complexity of the model. To overcome the challenge, a neighboring cell list needs to be maintained, which is difficult for GPU memory due to its dynamic nature. Besides this challenge, an incomplete translation of computation from CPU to GPU requiring frequent data transfer between them can also be rate limiting. As a result, the threshold of performing cell simulation to a size that is relevant to the small tissue scale remains out of reach for many biological researchers even with modern GPU architecture.

To overcome these challenges, we employed several novel computational techniques to fully leverage the GPU architecture, improve the simulation performance, and minimize memory usage.

As the computational cost of cell-cell interaction rises quadratically with the cell number, we developed a GPU-friendly voxel sorting method that handles the short-range cell-cell interaction modeling and improves the simulation's memory access efficiency. We also implemented a fully GPU-based LOD solver for the spatiotemporal variation of diffusive substance distribution in extracellular water. As a result, we optimized the evolution algorithm to achieve linear computational complexity O(N) while minimizing the memory footprint. In the numerical

implementation, we fully exploited the parallel architecture of modern GPU and different types of GPU memory for high computational speed and low memory access overhead. The computation is nearly 100% on GPU, thus avoiding slow data transfer between CPU and GPU memories.

Our GPU implementation significantly outperformed CPU methods and led to almost 400X speedup over the single thread version of the well-established CPU simulator on a personal computer. The acceleration is the highest among existing GPU-powered simulators. The acceleration, in combination with the low memory footprint, makes Gell readily available to biology researchers. The easy-to-access platform would facilitate the fast prototyping of hybrid models and hypothesis testing for large-scale problems.

As a future research direction, Gell can be scaled to multiple GPUs for larger problems on the order of 10^9 cells. As previously alluded to, simulation of tumor vasculature and other scaffolding cells such as the stromal cells and immune cells would be necessary for a biologically relevant model. Besides our effort to incorporate these extremely complex biological processes for digital tumor twins, we support our peers to join the effort by providing and updating Gell as a user-friendly open-source tool. The source code can be found at https://github.com/PhantomOtter/Gell.

2.5 Conclusion

Large scale cell simulations are valuable for hypothesis generation and testing experimental parameters. However, the high computational cost of the simulation using CPU has limited the simulation size and practicality. In the current study, we describe a novel GPU cell simulation platform Gell to fully leverage the highly parallel nature of GPU. For the first time, we demonstrated a GPU-friendly voxel sorting method that reduced the quadratic cell-cell interaction computational complexity to be linear. The full GPU implementation avoided unnecessary CPU-GPU data transfer overhead. As a result, Gell achieved a 400X acceleration and 1-2 order of magnitude reduction in the memory footprint compared to a state-of-the-art CPU cell simulation platform, PhysiCell, for the same hanging droplet tumor spheroid and ductal carcinoma in situ simulation tasks.

3.Chapter 2: Comprehensive Hemodynamics and Oxygenation Modeling of Real Vasculature

Tumor vasculature plays a crucial role in tumor development and the emergence of tumor heterogeneity. Accurate modeling of morphology and functions of the vasculature system is essential for understanding the tumor microenvironment and tumor development. This chapter analyzes tissue hemodynamic and oxygenation properties based on real vasculature structures from both tumor and healthy murine tissue. On top of the matured hemodynamics modeling, we present a novel 3D-1D coupled semi-implicit finite difference scheme that can solve the ultra-large-scale vasculature-based perfusion and oxygenation in real-time, which, to the best of our knowledge, was not previously possible, providing a tool for mechanistic understanding of tissue perfusion and oxygenation. We robustly solve the steady state oxygenation of various tumor and healthy tissue systems under various perfusion conditions and model the time-dependent FLASH depletion and recovery kinetics, revealing a marked dependency on tissue type.

3.1 Introduction

Vasculature plays a crucial role in supplying tumor development and contributes significantly to the heterogeneity observed within tumors. It is the believed that The misshapen, irregular, disorganized, and tortuous architecture arising from tumor-induced angiogenesis eventually results in the formation of hypoxic voids, necrosis, and an acidic milieu, which are the basis for imaging tumor heterogeneity with CT[56].

Functions of vasculature carry profound implications for therapeutic strategies. Vessel perfusions are crucial for drug delivery and vasculature-based oxygenation of tumor tissue affects various treatment efficacies. Radiation therapy is notably more effective in normoxic regions; it can be more than twice as efficacious for well-oxygenated tissue compared to anoxic regions. This boosting effectiveness is referred to as the oxygen enhancement ratio (OER)[86]. FLASH-RT, which delivers an ultra-high dose rate for cancer treatment, is observed to produce less normal tissue toxicity while maintaining similar tumor control. Although the mechanism behind such FLASH effect is unclear, oxygen is believed to play a central role within[88].

In the emerging era of personalized medicine, a thorough understanding of tumor vasculature and its function is crucial. This knowledge is vital for comprehending tumors' heterogeneous development and predicting their response to treatments, enabling more tailored and effective therapeutic strategies.

While significant advancements in understanding and modeling perfusion in large vasculatures have been made by Secomb et al.—ranging from empirical formulation for in vivo viscosity[89] and discharge hematocrit distribution[90] to optimize based vasculature boundary blood pressure estimation[91]—the challenge of oxygenation through large vascular systems remains. Various models, such as the Krogh cylinder model[92], kernel-based models[93], finite element-based methods[94], and Green's function-based methods[95,96] have been proposed. However, none can adequately handle ultra-large-scale real tumor vasculature while balancing computational speed, memory usage, and biophysical fidelity.

To bridge this gap, we have developed a robust, high-performance modeling platform designed to enable advanced oxygenation analysis across ultra-large-scale, dynamically coupled vasculature-tissue systems.

3.2 Methods

3.2.1 Vasculature Data

We obtained three sets of vasculature data from public sources. Two datasets pertain to tumor vasculature, as detailed in[97]: one from a human colorectal carcinoma (LS174T) xenograft grown subcutaneously in 8–10-week-old female immune-compromised nu/nu nude mice for 10–14

days, and another from orthotopic GL261 murine glioma tumors developed over 20 days post-injection into the brains of 8-week-old female C57BL/6 mice. For both tumors, fluorescent labeling and perfusion fixation were conducted, followed by tumor resection and optical clearing. The transparent tumors were imaged using optical CT, yielding resolutions between 4.3 μm and 8 μm, varying by sample size.

The third dataset represents healthy brain tissue vasculature from a 3-month-old C57Bl6 mouse[98]. Following immunolabeling and tissue clearing, the right hemisphere was imaged using light sheet microscopy at a 1.63-micron isotropic resolution. The caudoputamen vasculature was manually segmented, guided by its alignment with the Allen Mouse Brain Atlas[99]. The caudoputamen (corpus striatum) was selected for its critical role in motor control, cognition, and emotion within the basal ganglia, its accessible perfusion data for model calibration, and the comprehensive coverage of its volume within the hemisphere vasculature data.

3.2.2 Mathematical Representation of Vasculature

In our study, the term 'tubes' is used to describe the small vessel segments required to capture the curvature and radius of an entire vessel from one end to the other. The points where these tubes connect are called 'nodes'. An 'edge' refers to a complete vessel that starts and ends at either bifurcation points or blind ends. Additionally, these bifurcation points and blind ends are designated as 'vertices'. The topology of the vasculature network is described as a multigraph

$G = \{V, E, f\}$ as a collection of vertices $v_i \in V$ where vessel segments start and end, edges $e_k \in E$ represents the vessel segments between two vertices, and a function $f: E \rightarrow \left\{\{v_i, v_j\}: v_i, v_j \in V \; and \; v_i \neq v_j\right\}$ provides a mapping from edges to the vertices they connect. The vessel vertices in our study The maximum degree of vessel vertices should be three considering the cellular nature of vessel components, however, due to the imaging resolution limits, the extracted vasculature structures from imaging data usually have higher maximum degrees sometimes up to ten[100].

3.2.3 Blood Flow Hemodynamics

3.2.3.1 In vivo Blood Viscosity

Modeling blood flow within a given large vasculature poses a significant challenge. The Navier–Stokes equations for the fluid can be difficult and expensive to solve, and the presence of cellular components, which deviate the blood's behavior from the homogeneous fluid, particularly in micro-vasculatures, makes the problem even more complex.

An alternative strategy involves assuming Hagen–Poiseuille flow within each vessel segment and subsequently adjusting the apparent viscosity using empirical formulas derived from experimental data[91]. This approach has gained widespread acceptance and, to the best of our

knowledge, remains the only appropriate method for addressing blood flow in large microvascular systems. Therefore, in this study, we embrace this framework for modeling the hemodynamics of vasculature.

Assuming Hagen–Poiseuille flow in the lumen of the vessel segment e_k where $f(e_k) = \{v_i, v_j\}$, the blood flow rate Q_k goes:

$$Q_k = G_k \cdot (P_i - P_j)$$

Equation 3-1

$$G_k = \frac{\pi \cdot R_k^4}{8 \cdot \mu_k \cdot L_k}$$

Equation 3-2

Where G_k is the hydraulic conductance, and μ_k is the apparent viscosity of the blood flowing within. R_k and L_k stands for the radius and the length of the vessel segment. The reference rat blood plasma's apparent viscosity μ_0 measured at 37℃ is 1.05 cP[90]. An additional two-step correction is required to account for various vessel diameters and red blood cell (RBC) concentration conditions and estimate realistic in vivo apparent viscosity in blood vessels.

The first correction is for in vitro viscosity that considers the plasma cell-free layer due to the centering movement of erythrocytes resulting in lower resistance between flow and tube wall, also known as the Fahraeus-Lindqvist Effect[101]. A. R. Pries et al.[102] proposed an empirical correction for such an effect based on in vitro glass tube experiments:

$$\eta_{vitro} = 1 + (\eta_{0.45} - 1) \cdot \frac{(1 - H_d)^C - 1}{(1 - 0.45)^C - 1}$$

Equation 3-3

$$\eta_{0.45} = 220 \cdot e^{-1.3D} + 3.2 - 2.44 \cdot e^{-0.06D^{0.645}}$$

Equation 3-4

$$C = (0.8 + e^{-0.075D}) \cdot \left(\frac{1}{1 + 10^{-11} \cdot D^{12}} - 1\right) + \frac{1}{1 + 10^{-11} \cdot D^{12}}$$

Equation 3-5

Where D is the measured anatomic vessel diameter in microns, η_{vitro} is the relative apparent viscosity and $\eta_{0.45}$ is that of rat blood with discharge hematocrit at a level of 0.45. The term discharge hematocrit is defined as the volume fraction of RBCs delivered by the blood flow[103]. The second correction accounts for the endothelial layer (ECL) that observed to substantially increase the in vivo blood viscosity[104]. The effective thickness of the layer W_{eff} can be calculated by adding an asymptotic component W_{as} and a biphasic component W_{peak} with a peak[90]:

$$W_{eff} = W_{as} + W_{peak} \cdot (1 + 1.18 \cdot H_d)$$

Equation 3-6

$$W_{as} = \begin{cases} 0 & if\ D \leq 2.4 \\ 2.6 \cdot \dfrac{D - 2.4}{D + 100 - 4.8} & if\ D > 2.4 \end{cases}$$

Equation 3-7

$$W_{peak} = \begin{cases} 0 & if\ D \leq 2.4 \\ 1.1 \cdot \dfrac{D - 2.4}{10.5 - 2.4} & if\ 2.4 < D \leq 10.5 \\ 1.1 \cdot e^{-0.03 \cdot (D - 10.5)} & if\ 10.5 < D \end{cases}$$

Equation 3-8

Then the effective diameter and in vivo relative apparent blood viscosity D_{eff} reads:

$$D_{eff} = D - 2W_{eff}$$

Equation 3-9

$$\eta_{vivo} = \eta_{vitro} \cdot \left(\frac{D}{D_{eff}} \right)^4$$

Equation 3-10

3.2.3.2 Linear System Construction for Blood Flow

With the in vivo viscosity and boundary condition given, a linear system can be constructed by applying mass conservation to all the vertices in the vasculature graph.

$$G^M \cdot P^M = Q^M$$

Equation 3-11

Where G^M is a sparse symmetric matrix for hydraulic conductance of all vessel segments with

$$G_{ij}^M = \begin{cases} -G_{i,j} & i \neq j \\ \sum_{v_k \in V} G_{i,k} & i = j \end{cases}$$

Equation 3-12

$$with\ G_{i,j} = \sum_{e_k \in E_{i,j}} G_k$$

Equation 3-13

Where $E_{i,j}$ is the set contains all the edges that connect both vertices v_i and v_j. P^M is the vector of blood pressure at vertices, and Q^M is the vector of the blood flow rate of net outflow from vertices. By splitting inner vertex and boundary vertex-related terms into different sides of the equation, the linear system can be transformed to[105]:

$$G_{int}^M \cdot P_{int}^M = G_b^M \cdot P_b^M$$

Equation 3-14

G_{int}^{M} is the submatrix of the hydraulic conductance matrix that contains inner vertex rows, while G_{b}^{M} only contains boundary vertex rows. With given boundary blood pressure values P_{b}^{M}, the unknown inner vertex blood pressure P_{int}^{M} can be effectively solved using the generalized minimum residual method (GMRES)[106]

3.2.3.3 Phase Separation Effect

The volume fraction of RBCs in blood: Hematocrits have a highly heterogeneous distribution in real vasculature, especially in poorly structured tumor vasculatures[107], due to the nonproportional distribution of RBCs in daughter branches at diverging bifurcations known as the phase separation effect[108]. It is important to obtain an estimation of RBC distribution in vasculature not only because of its effect on apparent blood viscosity but also because of its dominating role in oxygen delivery. Approximately 98% of the oxygen carried in the blood is bound to hemoglobin contained in RBCs, while only 2% is dissolved in plasma and RBC water[109]. Vessels without adequate red blood cells are unable to support the tissue metabolism despite the flow rate.

In this study, we assume a uniform discharge hematocrit feed of 0.45[110] at the vasculature inlet. In the downstream bifurcation vertices in the vasculature, we adopted an experimentally determined parametric description of the phase separation effect by Pries AR et al.[90]:

$$logit(FQ_E) = A + B \cdot logit\left(\frac{FQ_B - X_0}{1 - 2X_0}\right)$$

Equation 3-15

$$A = -13.29 \cdot \frac{{D_\alpha}^2 / {D_\beta}^2 - 1}{{D_\alpha}^2 / {D_\beta}^2 + 1} \cdot \frac{1 - H_d}{D_p}$$

Equation 3-16

$$B = 1 + 6.98 \cdot \frac{1 - H_d}{D_p}$$

Equation 3-17

$$X_0 = 0.964 \cdot \frac{1 - H_d}{D_p}$$

Equation 3-18

D_p, D_α and D_β are the vessel diameters of the parent vessel and two daughter vessels measured in microns. H_d is the discharge hematocrit of the parent vessel. FQ_E is defined as the fractional flow of RBCs into the daughter branch α and FQ_B is the corresponding blood flow fraction. The RBC distribution at each bifurcation vertex can be calculated as shown above using a bisection method. Combining this with a depth-first search (DFS)-like algorithm, the discharge hematocrit distribution in the entire vasculature network can be obtained efficiently.

3.2.3.4 Virtual Vessels

For vasculature structures extracted from medical images obtained using micro-CT[105] or optical projection tomograph[97], one vascular vertex may connect more than three vessel edges due to the resolution limit of the images. To overcome the difficulties of applying the bifurcation RBCs flow fraction equations to these vasculature data, we introduced the virtual vessels. For vertices with outflow edge numbers bigger than two, we first calculate the RBC fractional flow of each outflow edge compared to the virtual vessel combining all other outflow edges. Assuming a vertex $Veretx_{vi}$ connecting to a set of outflow edges $\mathbb{N}_{Out}$. The virtual D_β for vessel $i \in \mathbb{N}$ is defined as:

$$D_{\beta_{virtual}}{}^3 = \sum_{j \in \mathbb{N}_{out} \setminus \{i\}} D_j{}^3$$

Equation 3-19

The exponent of three comes from transport cost and transport medium maintenance minimization condition for laminar flow, known as Murray's Law[111], which agrees well with experimental measurements[112]Once the fractional flow of RBCs is calculated for each outflow edge, the final flow fraction can be obtained after the total flow fraction is normalized to one.

If multiple inflow vessels also exist, a virtual parent vessel can be introduced:

$$D_{F\_virtual}{}^3 = \sum_{i \in \mathbb{N}_{in}} D_i{}^3$$

Equation 3-20

$$H_{D\_virtual} = \frac{\sum_{i \in \mathbb{N}_{in}} H_{D_i} \cdot Q_i}{\sum_{i \in \mathbb{N}_{in}} Q_i}$$

Equation 3-21

Where $\mathbb{N}_{in}$ is the set contains all the inflow edges for this vertex, D_i, H_{D_i}, and Q_i are the diameter, discharge hematocrit, and flow of the parent vessel i.

3.2.3.5 Iterative Update

Discharge hematocrit levels significantly influence the apparent viscosity of blood in each vessel segment, potentially altering the flow patterns within the vasculature system. To tackle the interaction between blood flow and discharge hematocrit distribution, we employ an iterative approach. This involves solving a linear system for blood flow and conducting vasculature traversal for discharge hematocrit until the system reaches convergence. Typically, with a physiologically plausible vasculature structure, convergence is achieved with low iteration differences within 3-4 iterations.

3.2.3.6 Edge Contraction

The node-tube representation of vasculature data effectively captures vascular morphology and vessel shape. However, the extensive number of nodes and tubes could significantly complicate the computation of blood flows. To improve computational efficiency, we developed a corresponding vertex-edge model specifically for hemodynamic calculations within the vasculature. This approach leverages the fact that non-leaking edges exhibit consistent flow through all constituent tubes, meaning that only the aggregate information of each edge and the pressure at its vertices are required to assess perfusion. By applying edge contraction to the vasculature, conducting hemodynamic computations on this equivalent vertex-edge model, and then mapping the results back to the original node-tube representation, we significantly enhance computational efficiency, achieving improvements by orders of magnitude.

3.2.3.7 Boundary Condition Optimization

Large tumor vasculatures contain numerous inlets and outlets on their surface, making the experimental determination of the blood pressure at these boundary nodes infeasible. Alternative approaches are needed to estimate this missing information. Following the work of Fry et al.[91]

we adopted an optimization-based boundary condition estimation framework, emphasizing a physiological distribution of vessel wall shear stress (WSS). The WSS τ_w of a vessel segment can be calculated from:

$$\tau_w = \frac{R\Delta P}{2L} \; or \; \frac{4\mu Q}{\pi R^3}$$

Equation 3-22

The objective function for boundary condition optimization is shown below:

$$minimize\ L = \frac{k_p}{2} \sum_{k \in Nodes} w_{pk}\left(P_k - P_{target}\right)^2 + \frac{k_\tau}{2} \sum_{j \in Tubes} w_{\tau j}\left(\left|\tau_j\right| - \tau_{target}\right)^2$$

$$s.t.\ Q_i = 0\ for\ i \in Inner\ nodes$$

Equation 3-23

Entire optimization is constrained by the blood flow mass balance at the vertices. The first term determines the main blood pressure across the vasculature and constrains the range of blood pressure within, with w_{pk} being a weight for nodes depending on the summed length connecting to it and k_p as a universal weighting factor for this pressure term. The second term promotes a certain wall shear stress for the edges and prevents a zero-flow solution for the problem, with $w_{\tau j}$ weights the edge length and k_τ weights the entire second term.

The wall shear stress at each vessel is a signed value depending on the flow direction. To estimate unknown flow direction in large vascular systems, we utilize an approach akin to simulated annealing. This strategy involves repeated optimization of boundary conditions with doubled wall shear stress (WSS) weights at each optimization level, and constantly updated flow direction estimation along the process. Initially, flow or WSS directions are randomly assigned. Multiple optimizations are performed at each weight level, and the flow direction estimation is updated according to previous optimization results. The stop criteria to stop or enter the next level is the inter-optimization flow direction agreement. The latest optimization result with the desired WSS weight is adopted as the final boundary condition estimation.

3.2.4 Intravascular Oxygen Transportation

The oxygen delivery through blood is stored in two forms: one is water-resolved oxygen in plasma and cell fluids, and the other one is the oxygen bound to the hemoglobin inside red blood cells. The total oxygen flux is a function of blood flow rate, red blood cell fraction, and oxygen concentration, writes:

Oxygen is contained in the blood in two primary forms: dissolved in plasma and cell fluids and bound to hemoglobin within red blood cells. The total oxygen flux (OF) depends on the blood flow rate (Q), the red blood cell flow fraction (discharge hematocrit), and the oxygen concentration, expressed by the equation:

$$OF(Q, H_D, P_{oxy}) = Q \cdot (P_{oxy} \cdot a_{plasma} + S_{oxy} \cdot H_D \cdot a_{rbc})$$

Equation 3-24

Where H_D is the discharge hematocrit of the blood and P_{oxy} is the oxygen partial pressure in the blood plasma. S_{oxy} is the oxygen saturation of hemoglobin, it is related to oxygen partial pressure P_{oxy} through Oxygen-Hemoglobin Dissociation Curve[113], which can be described by Hill's equation:

$$S_{oxy} = \frac{\left(\frac{P_{oxy}}{27\ mmHg}\right)^{2.7}}{1 + \left(\frac{P_{oxy}}{27\ mmHg}\right)^{2.7}}$$

Equation 3-25

The constants $a_{plasma} = 3 \times 10^{-5}\ mlO_2/ml/mmHg$ and $a_{rbc} = 0.447\ mlO_2/ml$ represent the oxygen solubility in plasma and red blood cells, respectively. In physiological conditions, red blood cells can store up to 99% of oxygen, underscoring their critical role in oxygen transport.

Inspired by the in vivo observation of Kerger et al.[114]we adopted a flow velocity-dependent inflow blood oxygen level writes:

$$P_{oxy} = P_0 + v \cdot 2.5\ mmHg \cdot s/mm$$

Equation 3-26

Where v is the blood velocity at the boundary inlets, and P_0 is a tunable parameter for the overall blood oxygen level.

3.2.5 Transvascular Oxygen Transportation

The oxygen supply rate from a vessel segment into the surrounding tissue can be written as[115]:

$$S = A_{vas} \cdot MTC_{oxy}\left(P_{boxy} - P_{wall}\right)$$

Equation 3-27

Where A_{vas} is the surface area of the vessel segment, P_{boxy} is the blood oxygen partial pressure and is modeled as constant for perfused vessels, and P_{wall} is tissue oxygen partial pressure at the vessel surface. MTC_{oxy} is the mass transfer coefficient (MTC) for transvascular oxygen release[115]:

$$MTC_{oxy}(H_D) = 17.7{H_D}^2 - 1.07H_D + 0.672 \; {nlO_2}/{s \cdot cm^2 \cdot mmHg}$$

Equation 3-28

Contrary to models that treat vessel walls as diffusion surfaces[116], incorporating the mass transfer coefficient (MTC) enhances computational efficiency by obviating the need for detailed vessel surface representation. This approach also achieves closer alignment with in vivo measurements, particularly regarding the dependence of discharge hematocrit.

3.2.6 Tissue Oxygen

Oxygen distribution in homogeneous tissue is governed by following equation, considering the oxygen diffusion in tissue, the oxygen consumption by tissue, and the oxygen supply through perfused vasculature:

$$\frac{\partial P_{oxy}}{\partial t} = \nabla \cdot \left(D_{oxy} \nabla P_{oxy}\right) - \frac{1}{a_{oxy}} M\left(P_{oxy}\right) + \frac{1}{a_{oxy}} S\left(P_{oxy}\right)$$

Equation 3-29

Where P_{oxy} is the oxygen partial pressure, D_{oxy} and a_{oxy} are oxygen diffusion coefficient and solubility in tissue, respectively. $M(P_{oxy})$ is the Michaelis-Menten type tissue oxygen consumption, reads:

$$M(P_{oxy}) = \frac{M_{max} P_{oxy}}{P_{oxy} + P_{M50}}$$

Equation 3-30

P_{M50} is the critical oxygen partial pressure when the consumption rate reaches half maximum, it is usually a small value in the range of 0.5-1 mmHg[117]. M_{max} is the maximum oxygen consumption rate, which can vary dramatically across cell types[118]. The baseline resting oxygen metabolism rate of the human body, also called the One metabolic equivalent (MET) is 3.5 mlO2/kg/min[119], while that for the human brain can be up to 35 mlO2/kg/min[120]. For rats, according to HM Wiesner[121], compared to humans, the baseline body metabolism is much higher, but the brain oxygen metabolism rate is similar, reports 24.2 mLO2/kg/min and 1.97 μmol/g/min, respectively. For brain glioma, due to The Warburg Effect[122], its metabolism can be significantly lower than that of normal tissue. Daniel Paech et al.[123] measured an average 0.23 ± 0.07 μmol/g/min oxygen metabolism rate for high grade glioma and 0.39 ± 0.16 μmol/g/min for low grade glioma.

According to these literature values, human body metabolism can be approximated at a rate of 1.5 mmHg/s. We have adopted this value as the oxygen consumption rate (OCR) for the LS174T

human colorectal carcinoma xenograft. Considering the metabolic similarities between human and mouse brain tissues, we set the OCR for mouse caudoputamen at 20 mmHg/s. For the GL261 mouse brain glioma, in the absence of direct reference data, we use the OCR of 4 mmHg/s, which is based on values reported for human glioblastoma multiforme (GBM).

3.2.7 Vasculature-Tissue Coupling

Accurately coupling vessel perfusion with oxygen release into surrounding tissue presents a complex and computationally demanding challenge. Currently, high-performance methods for managing large systems are lacking. To address this gap and enable ultra-large-scale vasculature modeling, we propose a novel semi-implicit 3D-1D coupled method. This method is optimized for high-performance GPU-based modeling and is capable of characterizing time-dependent intravascular oxygen transportation and transvascular oxygen release across the vessel wall.

3.2.7.1 Mass Balance of Oxygen

To refresh from the previous discussion, the oxygen flux in the blood can be calculated as:

$$OF\left(Q, H_D, P_{boxy}\right) = Q \cdot \left(P_{oxyb} \cdot a_{plasma} + \frac{\left(\frac{P_{boxy}}{27\ mmHg}\right)^{2.7}}{1 + \left(\frac{P_{boxy}}{27\ mmHg}\right)^{2.7}} \cdot H_D \cdot a_{rbc}\right)$$

Equation 3-31

Using i as the index for vessel node, and j for vessel tube, considering a node with a set of inflow tube $J \in \mathbb{N}_{in,i}$ and outflow tube $J \in \mathbb{N}_{out,i}$, assuming that confluence blood get well mixture and results in homogeneous oxygen partial pressure in the outflow, the blood oxygen partial pressure at the node i can be calculated by solving the following equation:

$$\sum_{J \in \mathbb{N}_{in,i}} OF\left(Q_j, H_{D\,j}, P_{boxy,j}\right) = OF\left(\sum_{J \in \mathbb{N}_{in,i}} Q_j\,, \frac{\sum_{J \in \mathbb{N}_{in,i}} Q_j\, H_{D\,j}}{\sum_{J \in \mathbb{N}_{in,i}} Q_j}, P_{boxy,i}\right)$$

Equation 3-32

The left side of this equation is constant, and the right side is a monotonically increasing function for node oxygen tension. This can be efficiently solved by simple bisection method. Notice that although oxygen partial pressure at equal in the downstream vessels, the discharge hematocrit distribution is heterogeneous due to the phase separation effect.

The oxygen flux into a downstream vessel $J \in \mathbb{N}_{out,i}$ can be written as:

$$OF_{in,j} = OF\left(Q_j, H_{D\,j}, P_{boxy,i}\right)$$

Equation 3-33

Considering a specific time interval from time t to $t + \Delta t$, based on the mass balance in the tube, the net oxygen released rate from the vessel segment to tissue can be calculated by

$$Release\ rate = OF_{in,j}^{t} - OF\left(Q_j, H_{D\,j}, P_{boxy,j}^{t+\Delta t}\right) + F\left(\frac{V_{vas,j}}{\Delta t}, H_{D\,j}, P_{boxy,j}^{t}\right) - F\left(\frac{V_{vas,j}}{\Delta t}, H_{D\,j}, P_{boxy,j}^{t+\Delta t}\right)$$

Equation 3-34

Where $V_{vas,j}$ represents the blood volume of the tube, and the latter two terms account for changes in the amount of oxygen stored within this blood volume. Including this blood volume term is crucial for ensuring a theoretically sound mass balance. Although this component may be negligible in high-perfusion vessels, it becomes essential in low or zero-perfusion scenarios, where oxygen transport is predominantly governed by diffusion from surrounding tissues rather than by perfusion from parent vessels. Such conditions are commonly observed in functionally compromised tumor vasculatures. Incorporating this term not only yields biologically reasonable oxygen tension results but also enhances the numerical stability of the simulation.

Considering a tissue voxel k receiving the released oxygen, the mass balance of tissue oxygen gives:

$$Release\ rate = \frac{P_{oxy,k}^{t+\Delta t} - P_{oxy,kj}^{t}}{K\Delta t}, K = \frac{1}{a_{oxy}V_{voxel}}$$

Equation 3-35

Where coefficient K represents the coefficient of conversion of oxygen volume to tissue partial pressure under the specific voxel size setting. $P_{oxy,kj}^{t}$ represents the tissue oxygen level of the voxel where the vessel j locates, indexed kj at time point t.

The oxygen release rate is constrained by the mass transfer coefficient and the vessel surface area of the tube:

$$Release\ rate = M_j \cdot \left(P_{boxy,j}^{t+\Delta t} - P_{oxy,kj}^{t+\Delta t}\right), M_j = A_{vas,j} \cdot MTC\left(H_{D\,j}\right)$$

Equation 3-36

We adopted an implicit release rate term for higher numerical stability. M is the release rate coefficient for the specific tube.

From these three equations, the blood oxygen tension at the time $t + \Delta t$ can be calculated by:

$$\frac{M}{1+MK\Delta t}P_{boxy,j}^{t+\Delta t} + OF\left(Q_j + \frac{V_{vas,j}}{N\Delta t}, H_{D\,j}, P_{boxy,j}^{t+\Delta t}\right)$$
$$= OF_{in,j} + \frac{M}{1+MK\Delta t}P_{oxy,kj}^{t} + OF\left(\frac{V_{vas,j}}{\Delta t}, H_{D\,j}, P_{boxy,j}^{t}\right)$$

Equation 3-37

The left side is monotonical for $P_{boxy,j}^{t+\Delta t}$, and right side is constant. After solved blood oxygen tension with bisection method, the tissue oxygen level can be acquired through:

$$P_{oxy,kj}^{t+\Delta t} = \frac{MK\Delta t \cdot P_{boxy,j}^{t+\Delta t} + P_{oxy,kj}^{t}}{1+MK\Delta t}$$

Equation 3-38

The amount of oxygen delivered from vasculature to target voxel is given by:

$$L = \frac{M\Delta t}{1+MK\Delta t}\left(P_{boxy,j}^{t+\Delta t} - P_{oxy,kj}^{t}\right)$$

Equation 3-39

3.2.7.2 Vessel Surface Sampling

Tumor vasculature exhibits a broad range of vessel diameters, from a few microns to tens of microns. To ensure accurate simulation results, it is crucial to completely cover the entire circumference of each vessel[95]. In this work, we adaptively sample multiple random equidistance points around the vessel circumference, each representing a part of the vessel surface as an independent oxygen source and releasing oxygen to their corresponding tissue voxels.

The estimation of vessel surface sampling data N is given by:

$$N = ceil(\frac{2\pi R k_N}{L_{voxel}})$$

Equation 3-40

Where R is the vessel radius, L_{voxel} is voxel length, k_N is a scaling parameter that controls sampling density. Ceil represents the ceiling function that returns the smallest integer value greater than or equal to the specified number. In the simulation, we first randomly sample one point on the center line of the vessel surface, then create the ret N-1 evenly distributed sampling points covering the circumference. The minimum sampling number is set to four to ensure adequate surface coverage across any vessel radius conditions.

The candidate blood oxygen tension calculated from the sampling point n can be acquired from:

$$\frac{M}{N+MK\Delta t}P_{boxy,j,n}^{t+\Delta t}+\ OF\left(\frac{Q_j}{N}+\frac{V_{vas,j}}{N\Delta t},H_{D\,j},P_{boxy,j,n}^{t+\Delta t}\right)$$
$$=\frac{OF_{in,j}}{N}+\frac{M}{N+MK\Delta t}P_{oxy,kjn}^{t}+OF\left(\frac{V_{vas,j}}{N\Delta t},H_{D\,j},P_{boxy,j}^{t}\right)$$

Equation 3-41

Where $P_{boxy,j,n}^{t+\Delta t}$ represent the candidate blood pressure of tube j calculated from sampling point n for time point $t+\Delta t$, $P_{oxy,kjn}^{t}$ represent the tissue oxygen level of the voxel where the sampling point n locates. The oxygen tension of the corresponding voxel of sampling points is directly updated through:

$$P_{oxy,kjn}^{t+\Delta t}=\frac{MK\Delta t\cdot P_{boxy,i,n}^{t+\Delta t}+N\cdot P_{oxy,kjn}^{t}}{N+MK\Delta t}$$

Equation 3-42

After traversing all the sampling points, the total oxygen release from the tube is calculated through:

$$L_N=\ \sum_n\frac{M\Delta t}{N+MK\Delta t}\left(P_{boxy,j,n}^{t+\Delta t}-P_{oxy,kjn}^{t}\right)$$

Equation 3-43

Then the final blood oxygen level at the time $t + \Delta t$ can be calculated based on mass balance principles:

$$OF\left(Q_j + \frac{V_{vas,j}}{\Delta t}, Hd, P_{boxy,j}^{t+\Delta t}\right) = OF_{in,j} + OF\left(\frac{V_{vas,j}}{\Delta t}, H_{D\,j}, P_{boxy,j}^{t}\right) - L_N$$

Equation 3-44

3.2.7.3 Update Scheme

By iteratively updating the node blood oxygen level information and the tube oxygenation information, the vascular system can evolve in a time-dependent manner. The method's design focuses on parallelism. For each step, all the nodes or tubes can be updated parallelly with no constraint on the update order, making it inherently GPU-friendly.

3.2.8 Implementation

All the code involved is developed in-house using Python. Packages, including SciPy and cvxpy (1.3.2), are used to solve linear system and optimization problems in hemodynamics modules. And Taichi[124] language is used for GPU computation in oxygenation models. A NVidia RTX 4090 graphics card is used for the simulation.

The voxel size in the simulation is 20 microns, which is comparable to the diameters of individual cells. The simulation time step is set to be $\Delta t = 0.001s$.

For the finite difference method applied to the oxygen diffusion process, the time stop constrain is $\Delta t \leq \Delta x^2/6D$, which equals 0.028s.

For intravascular transportation in the coupled perfusion-oxygenation module, a physical perfusion speed requires a step time $\Delta t \leq V_{vas,j}/Q_j$. This means the update time step should be smaller than the shortest flow-through time in the vascular system. A typical scenario involving a 20-micron vessel length and a flow velocity of 0.5 mm/s translates to a minimum time step of 0.04 seconds. While tumor vasculature may include a small fraction of vessels with exceptionally high flow rates imposing stringent demands on the time step, a time step of 1 ms is sufficient to accurately capture perfusion speeds up to 20 mm/s for a standard 20-micron tube length; for faster-flowing tubes, the modeled perfusion speed will be capped at 20 mm/s. Given that our data domain is less than one centimeter, failing to account for the part of flow rates exceeding 2 cm/s should not significantly impact the overall simulation accuracy.

For transvascular oxygen transportation, our model employs an implicit numerical scheme that inherently does not have a specific time step threshold. However, for optimal numerical accuracy, the desired time step is:

$$\Delta t \leq \frac{a_{oxy} \cdot V_{voxel} \cdot N}{MTC \cdot A_{vas}}$$

Equation 3-45

Where N is the surface sampling number. This threshold is comfortably achieved in our simulations, as the threshold remains above $1\ ms$ even with $N = 1$, according to the vascular data utilized in this study.

3.1 Results

3.3.1 Vascular Structure Characteristics

The rendered vasculature image and the histogram for radius distribution are shown in Figure 3-1. The colorectal carcinoma tumor is the largest, measuring up to 10.2 mm along its longest axis, yet it exhibits relatively sparse vasculature. In contrast, the smaller glioma tumor features a higher vessel density and a significant number of large vessels. The caudoputamen, although the smallest of the three, boasts the most extensively developed vasculature and the smallest mean vessel radius. The glioma tumor presents a considerable number of small-radius vessels, likely due to either a large portion of its vascular region being poorly structured with extremely low flow or errors from the imaging and vessel structure extraction process. Without knowledge of the ground truth, the assessment and correction of the second possibility fall outside the scope of this study.

Detailed statistics for these three tumors are provided in Table 3-1.

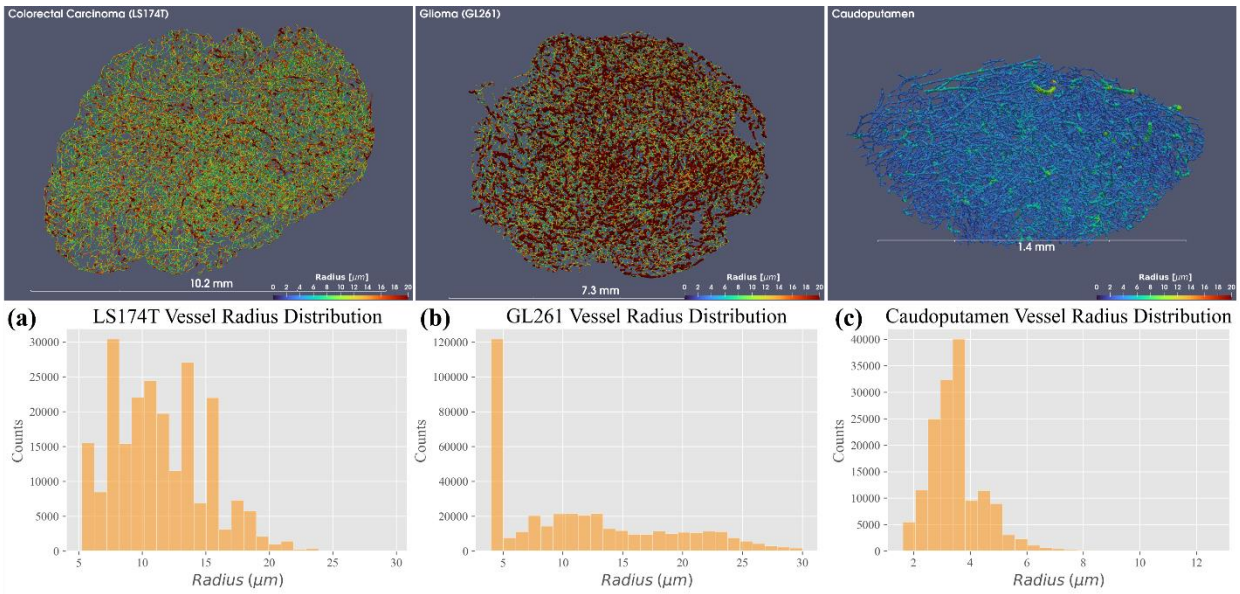

Figure 3-1 Rendered vasculature image and respective radius distribution histogram of Colorectal carcinoma (LS174T), Glioma (GL261), and Caudoputamen vasculature. The color is coded with radius.

	LS174T	**GL261**	**Caudoputamen**
No. of Tubes	224872	397923	152640
No. of Nodes	217739	387909	150624
No. of Edges	24934	41539	8431
No. of Vertices	17801	31535	6415

Domain Size (mm)	10.2 x 7.9 x 4.4	7.2 x 6.1 x 2.8	1.4 x 0.8 x 0.5
Tumor Volume (mm^3)	169.06	54.37	0.328
Mean Vessel Diameter (μm)	22.64 ± 7.26	23.38 ± 14.76	7.04 ± 2.02
Vessel Length (m)	4.98	4.14	0.355
Length density (mm^{-2})	29.5	76.2	1083.7
Vessel Surface Density (mm^{-1})	2.06	5.74	24.07
Vessel Volume Density (%)	1.28	4.77	4.616
Branching Length (μm)	199.79 ± 200.28	99.66 ± 69.20	42.15 ± 39.64

Table 3-1 Information table of vasculature data.

3.3.2 Hemodynamic Characteristics

The simulation results for coupled discharge hematocrit and blood flow distribution are shown in Figure 3-2.

Boundary pressure conditions are optimized with a mean vascular blood pressure of 40 mmHg across all vasculature data sets. The target wall shear stress (WSS) is finely tuned to align total tissue perfusion with reference data. For colorectal carcinoma, the simulated tissue perfusion of 18.65 nl/100g/min closely matches the measured reference of 19 nl/100g/min. Similarly, for glioma, the simulated perfusion of 110.58 nl/100g/min aligns well with the observed reference of

110 nl/100g/min. In the absence of direct reference data for caudoputamen, its WSS was calibrated in line with that of glioma, reflecting their common origin from mouse brain tissue. The modeled caudoputamen perfusion is 110 nl/100g/min, which is high considering a reference perfusion of 94 nl/100g/min for the larger encompassing structure of the mouse striatum. This discrepancy is acceptable and is partly attributed to the well-known volume dependency of perfusion measurements, which tend to yield higher values for smaller tissues due to their higher surface-to-volume ratio. Additionally, significant arteriole penetration in the sampled tissue likely contributes substantially to the overall perfusion.

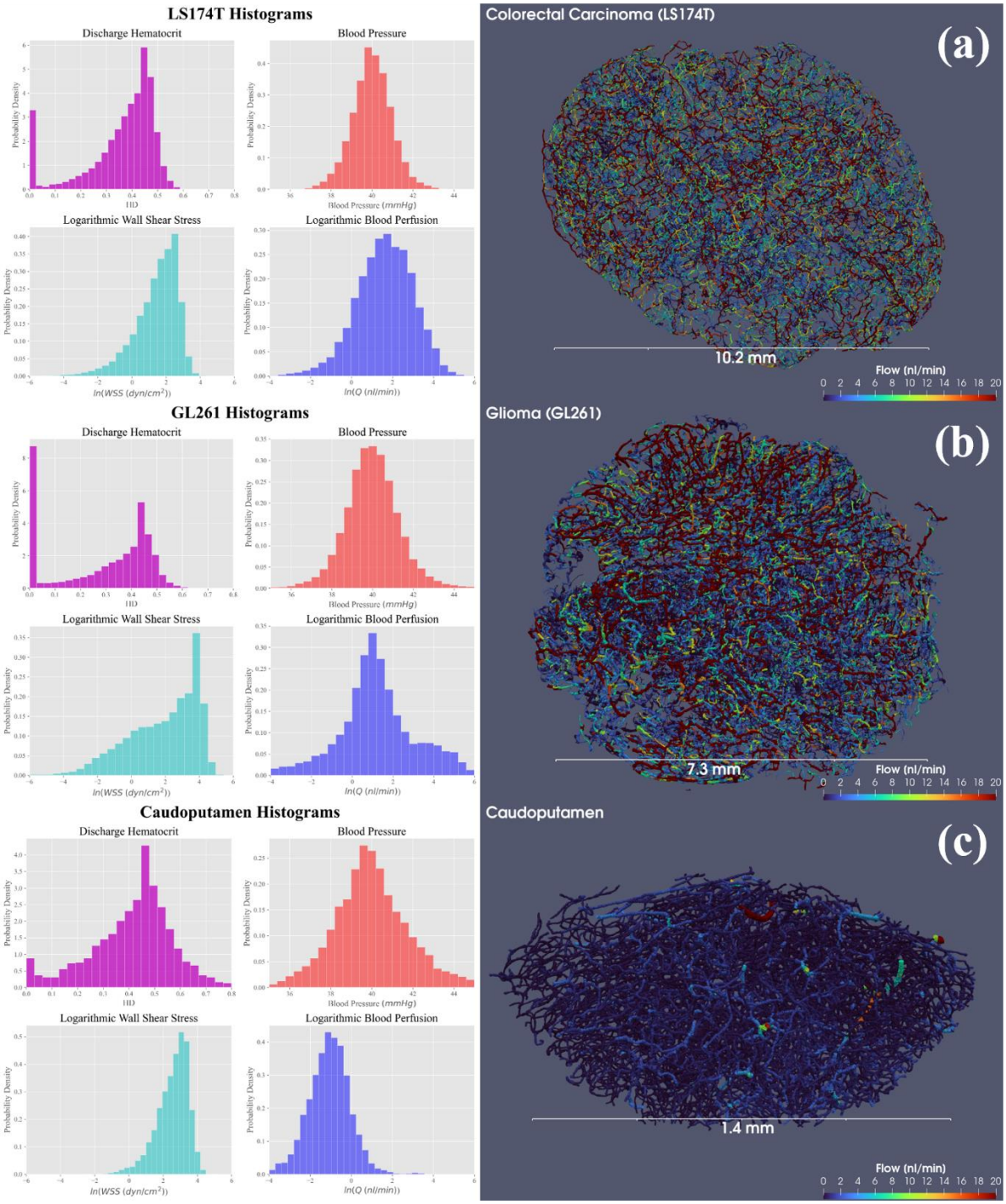

Figure 3-2 On the left side are Histograms for discharge hematocrit, blood pressure, logarithmic wall shear stress for perfused tubes, and logarithmic perfusion for perfused tubes. The criteria

for being perfused is 100 um^3/s. On the right side are rendered vasculature images that are color-coded for blood perfusion. From (a) to (c) displays the property of colorectal carcinoma, glioma, and caudoputamen, respectively.

The details of the statistics are listed in Table 3-2. All three types of vasculatures exhibit a broad range of discharge hematocrit distributions. Both tumor samples display a significant fraction of tubes with low or zero red blood cell components, indicative of compromised oxygen delivery capabilities. A particularly large fraction of tubes with zero hematocrit is observed in the glioma vasculature, likely due to its abundance of small vessels with low blood perfusion, and lead to a low fraction of red blood cells entering these bifurcation branches.

In the case of colorectal carcinoma and caudoputamen, blood flow, when represented on a logarithmic scale, typically shows a near-normal distribution across both high and low flow ranges. However, the glioma vasculature histogram is more spread out, featuring a significant number of tubes at higher blood flow values. This pattern may be attributed to its wider range of vessel diameters, likely indicating a subregion of interconnected large-diameter vessels.

	LS174T	**GL261**	**Caudoputamen**
Blood Flow (nl/min)	10.55 ±17.31	16.20 ± 56.38	0.60 ± 1.40

Blood Velocity (mm/s)	0.39 ± 0.48	0.44 ± 1.04	0.22 ± 0.20
Wall Shear Stress (dyn/cm^2)	6.68 ± 6.51	17.72 ± 24.49	17.78 ± 13.29
Tissue Perfusion (ml/min/100g)	18.65	110.58	198.66
Measured Reference Perfusion (ml/min/100g)	19 ± 8	110 ± 7	N/A

Table 3-2 Hemodynamics-related statistics.

3.3.3 Steady State Oxygenation

Once determined, the blood perfusion and discharge hematocrit distribution will not change anymore in the subsequent oxygenation simulation. The Zero-oxygen-flux Neuman condition is applied to the tumor boundary, and the tissue and blood volume are initialized to contain zero oxygen content when the simulation begins. Steady state is reached within 1 minute for all cases, and the simulation time was extended to 2 minutes to secure the reliability of the steady state result. With the step of 0.001 seconds, the simulation for each in silico seconds ranges from 1.4 to 3.6 seconds, representing an almost real-time simulation speed for ultra-large systems with tens of millions of voxels and hundreds of thousands of vessel segments.

Variation of tissue and blood oxygen level over time in the first minute from zero-oxygen initialization to the establishment of steady state oxygenation is shown in Figure 3-3.

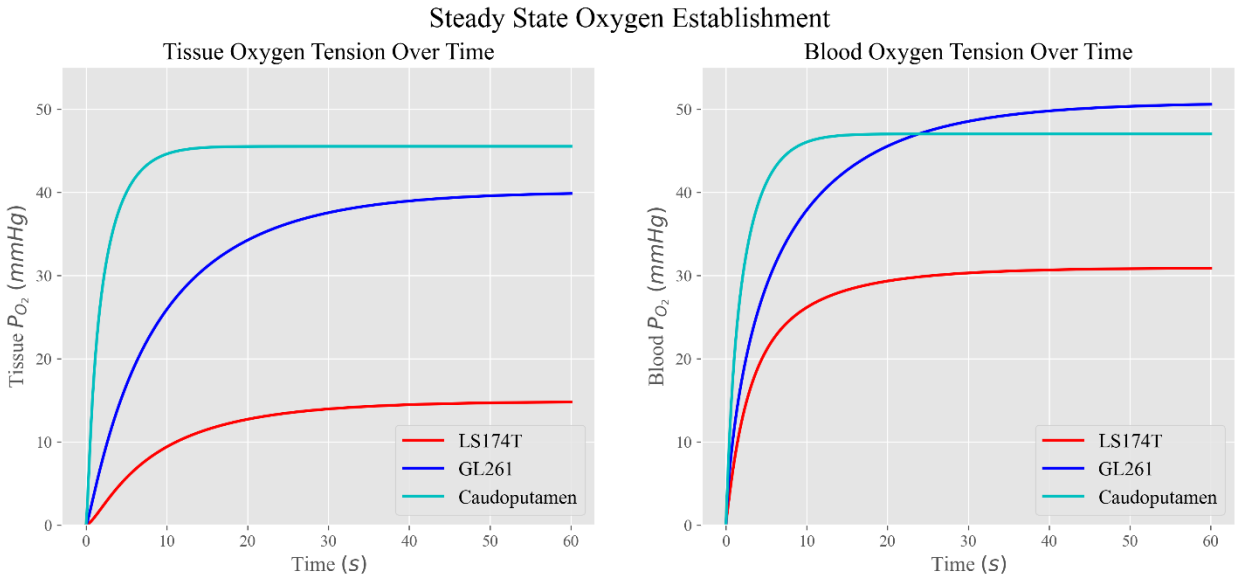

Figure 3-3 Establishment of steady state oxygenation from zero-oxygen initialization. Left: mean oxygen in the tumor. Right: mean oxygen in the blood.

The caudoputamen vasculature demonstrates the fastest establishment of tissue oxygenation, followed by the colorectal carcinoma vasculature. In contrast, the glioma vasculature shows the slowest oxygenation due to its relatively large tumor volume and the presence of large, slowly flowing vessels within a complexly interconnected vasculature system, which compromises overall perfusion efficiency.

Details about the simulation speed and steady state oxygen level results are listed in Table 3-3. The criterion for hypoxia is 3 mmHg, and that for anoxia is 0.01 mmHg.

	LS174T	GL261	Caudoputamen
Voxel Number	46.87 m	16.67 m	97.68 k
Tube Number	224872	397923	152640
Simulation Time per Thousand Steps (s)	2.3	3.6	1.4
Oxygen Consumption Rate (mmHg/s)	1.5	4	20
Blood Oxygen (mmHg)	30.9 ± 9.2	50.7 ± 16.1	47.0 ± 9.1
Tissue Oxygen (mmHg)	14.8 ± 11.3	40.0 ± 16.6	45.4 ± 8.0
Reference (mmHg)	15 [125]	30 - 55 [126]	20 - 60 [127]
Blood-Wall Oxygen Difference (mmHg)	0.79 ± 0.96	0.84 ± 1.55	0.84 ± 1.70
Blood Oxygen Extraction Fraction (%)	10.74	4.30	12.56
Hypoxic Fraction (%)	22.03	2.81	0.0
Anoxic Fraction (%)	8.65	1.07	0.0

Table 3-3 Oxygenation simulation information.

The colorectal carcinoma, characterized by the lowest oxygen consumption rate (OCR) and the sparsest vasculature, displays the lowest tissue oxygen levels. This is also reflected in the largest mean oxygen difference between the blood oxygen tension and the tissue oxygen level. In contrast, the glioma, with a moderate OCR and much denser vasculature, shows a smaller blood-tissue oxygen difference and a low oxygen extraction fraction of only 4.3%. The caudaputamen, despite having an OCR several times higher than that of tumor tissues, maintains a high average tissue oxygen level thanks to its highly developed vasculature. This efficient oxygen supply ensures that no hypoxic regions are present within the tissue.

Despite the significant variations in blood and tissue oxygen levels across the three tissue types, the oxygen tension difference across the vessel wall remains consistently around 0.8 mmHg, suggesting a similar oxygen delivery rate per unit surface area across the different tissues.

The central slice of the tissue oxygen and the histogram of blood and tissue oxygen level are shown in Figure 3-4.

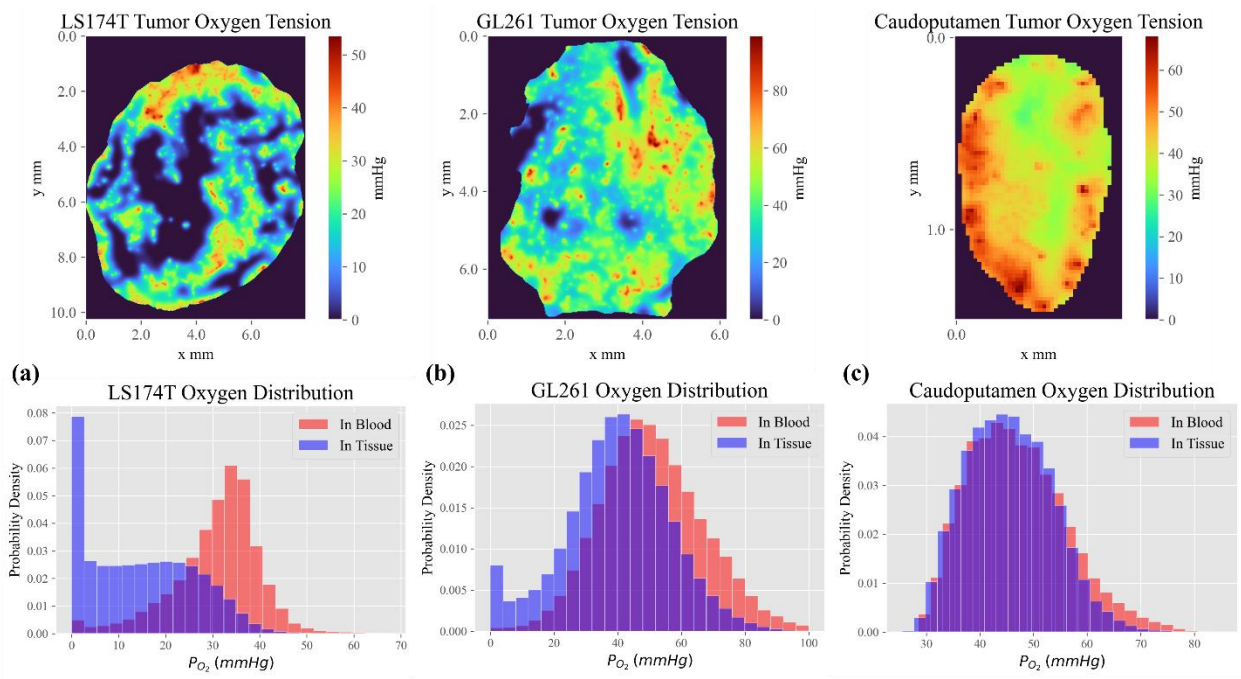

Figure 3-4 Steady state oxygenation results showing the central slice of tissue oxygen as histogram for both tissue and blood oxygen level.

The central slice image of tissue oxygenation reveals a large necrotic center in the colorectal carcinoma, a small fraction of regions with low or zero oxygen tension in the glioma, and a homogeneous and high oxygen distribution in the caudoputamen. Additionally, the histogram of blood and tissue oxygen levels shows a significant disparity in the colorectal carcinoma due to its sparse vasculature. In contrast, the more vascularized glioma tumor exhibits a smaller difference between blood and tissue oxygen levels. The most vascularized healthy caudoputamen displays minimal differences.

3.3.4 Influence of Initial Flow Direction Randomization in Boundary Condition Optimization

To explore the impact of randomly initiated flow directions in optimizing blood pressure boundary conditions on tumor perfusion and oxygenation, we generated five random boundary conditions for the GL261 vasculature. We then analyzed the vasculature's functional properties under these conditions. The results of this analysis are presented in Tables 3-4.

Random Flow Direction Initialization for GL261 Vasculature						
Steady State Functional Properties	**Sample 1**	**Sample 2**	**Sample 3**	**Sample 4**	**Sample 5**	**Statistics**
Tissue Perfusion (ml/min/100g)	110.58	112.46	107.51	107.56	105.37	108.70 ± 2.81
Blood Velocity (mm/s)	0.443	0.445	0.446	0.439	0.438	0.442 ± 0.003
Wall Shear Stress (dyn/cm^2)	17.72	17.66	17.86	17.77	17.66	17.73 ± 0.07

Tissue Oxygen (mmHg)	40.11	40.17	40.15	39.98	40.09	40.10 ± 0.07
Blood Oxygen (mmHg)	50.80	50.89	50.78	50.63	50.77	50.77 ± 0.09

Table 3-4 Effect of random flow direction initialization on vasculature perfusion and oxygenation.

The specific randomization of initial flow directions during the boundary condition estimation step minimally impacts the vasculature's functional properties. The standard deviation for tissue perfusion across five random samples is less than 3%, and for tissue oxygenation, it's below 0.01 mmHg. These stable results underscore the robustness of our comprehensive vasculature function estimation method, which performs effectively even without prior knowledge of classified arteries and veins within the system.

3.3.6 Influence of Blood Perfusion on Tissue Oxygenation

To assess how blood perfusion influences the final steady-state oxygenation of tissue, a series of simulations were conducted on a perfusion-scaled GL261 vasculature. The blood flow rates were scaled to range from 25 to 200 ml/100g/min, based on the original hemodynamic characteristics estimated from the vasculature system, while keeping the input blood oxygen saturation level constant. The effects of varied perfusion are illustrated in Figure 3-5. Figure 3-5 (a) reveals that

higher blood perfusion correlates with higher steady-state oxygen levels and a more rapid establishment of these levels. Figure 3-5 (b) shows a more detailed heterogeneous tissue oxygen distribution, with low perfusion resulting in significantly larger hypoxic regions. Figure 3-5 (c) displays a monotonic increase in mean tissue and blood oxygen levels with increased perfusion, while the oxygen partial pressure difference across the vessel wall remains relatively stable, only increasing from 0.72 mmHg to 0.87 mmHg as perfusion increases from 25 to 200 ml/100g/min. Figure 3-5 (d) indicates a negative relationship between blood perfusion and the fraction of hypoxic and anoxic tissue regions. Additionally, the blood oxygen extraction fraction dramatically decreases as perfusion increases.

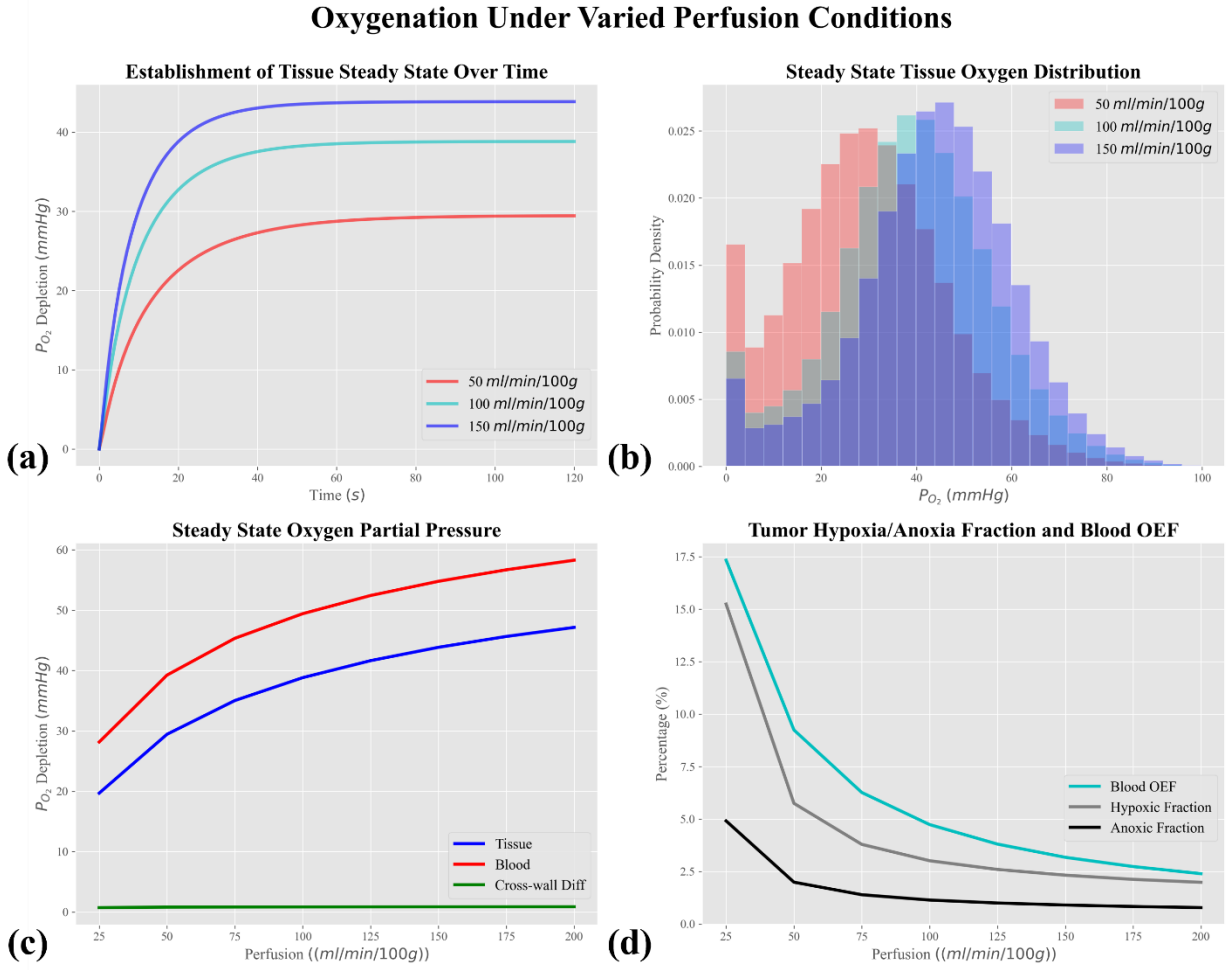

Figure 3-5 Oxygenation with varied tissue perfusion for GL261 tumor. For three example perfusion levels at 50, 100, and 150 ml/100g/min, (a) demonstrates the process of establishing oxygen steady state over time and (b) displays the final tissue oxygen level histogram for three perfusion levels. For a wider range of perfusion from 25 to 200 ml/100g/min, (c) shows the mean steady state tissue oxygen level and the oxygen level difference across the vessel wall, and (d) shows the fraction of hypoxic and anoxic regions in the tumor as well as the oxygen extraction fraction of the input blood oxygen across the perfusion range.

3.3.6 FLASH Oxygen Depletion Dynamics

We model the FLASH depletion by adjusting the tissue oxygen governing equation as:

$$\frac{\partial P_{oxy}}{\partial t} = \nabla \cdot \left(D_{oxy} \nabla P_{oxy}\right) - \frac{1}{a_{oxy}} M\left(P_{oxy}\right) + \frac{1}{a_{oxy}} S\left(P_{oxy}\right) + L_{ROD} \cdot D_r\ (t)$$

Equation 3-46

Where L_{ROD} is the radiolytic depletion rate at 0.4 mmHg/Gy, adopted from Cui et al.[94]. $D_r\ (t)$ is the dose rate function determined by irradiation settings. The oxygen depletion and recovery of 20 Gy dose delivery at 100 Gy/s is shown in Figure 3-4.

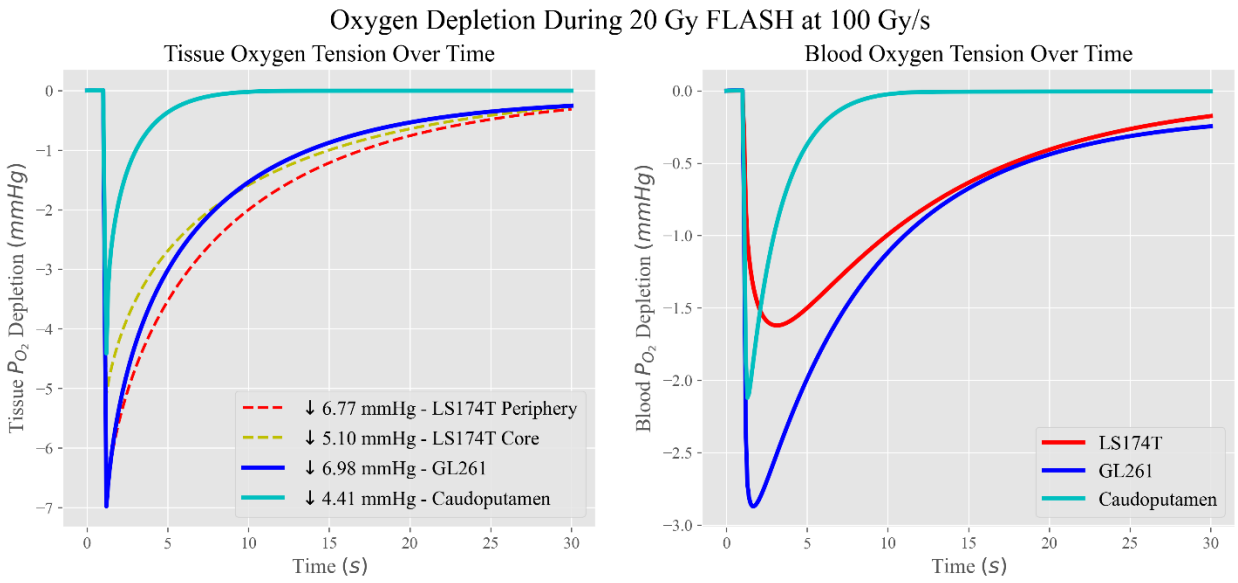

Figure 3-6 FLASH depletion and recovery curve for colorectal carcinoma, glioma, and caudoputamen respectively. The FLASH radiation at 100 Gy/s of a total 20 Gy dose was introduced 1 second after the simulation started. Left: absolute oxygen change in tissue over time. Right: absolute oxygen change in blood over time.

There is rapid oxygen depletion followed by slow recovery agrees with in vivo observation. The more extensively developed vasculature led to less oxygen level decrease at the end of the FLASH irradiation and faster oxygen recovery afterwards. The oxygen level decreases if it has a slower pace than tissue; the minimum oxygen level occurs after the radiation finishes when the oxygen supply from perfusion equals the rate of oxygen extraction supplying the FLASH-depleted tissue. The histogram of tissue oxygen level at the end of FLASH irritation is shown in Figure 3-7. The introduction of FLASH irradiation dramatically altered the oxygen distribution histogram for all three types of tissue. For colorectal carcinoma xenograft, a dramatic increase of anoxia region is observed, similarly for orthotopic murine glioma, although it remains a majority

of region highly oxygenated. For healthy murine caudoputamen, the introduction of a dose of up to 40 Gy didn't create any additional hypoxic region due to its high steady-state oxygen level.

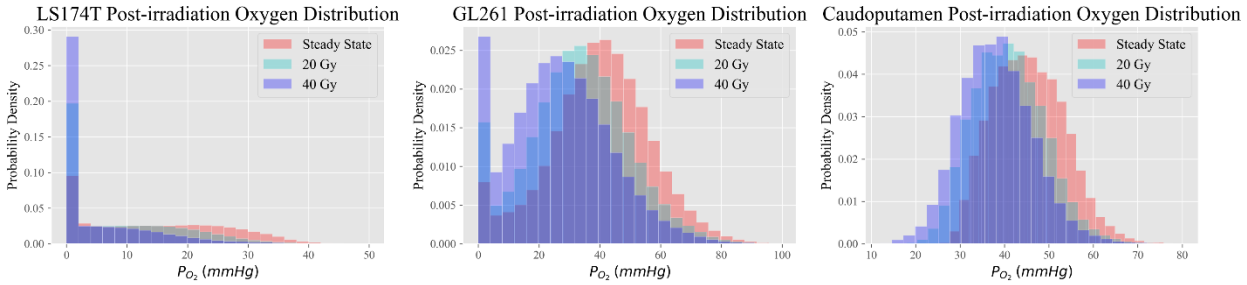

Figure 3-7 Tissue oxygen level at the end of irradiation, for all three types of tissue. Each figure contains three histograms, one for the steady state tissue, one for 20 Gy irradiation, and one for 40 Gy irradiation.

The maximum oxygen depletion amount with varying doses at a delivery rate of 100 Gy/s is shown in Figure 3-8. The amount of oxygen depletion is compensated by the oxygen supply from the blood. With a more vascularized tissue achieves less depletion. Estimation of oxygen level drop (green dotted line in Figure 3-8) without considering the blood oxygen supply can lead to significant overestimation of the depletion achieved. Furthermore, complete depletion is impossible within the normal dose range.

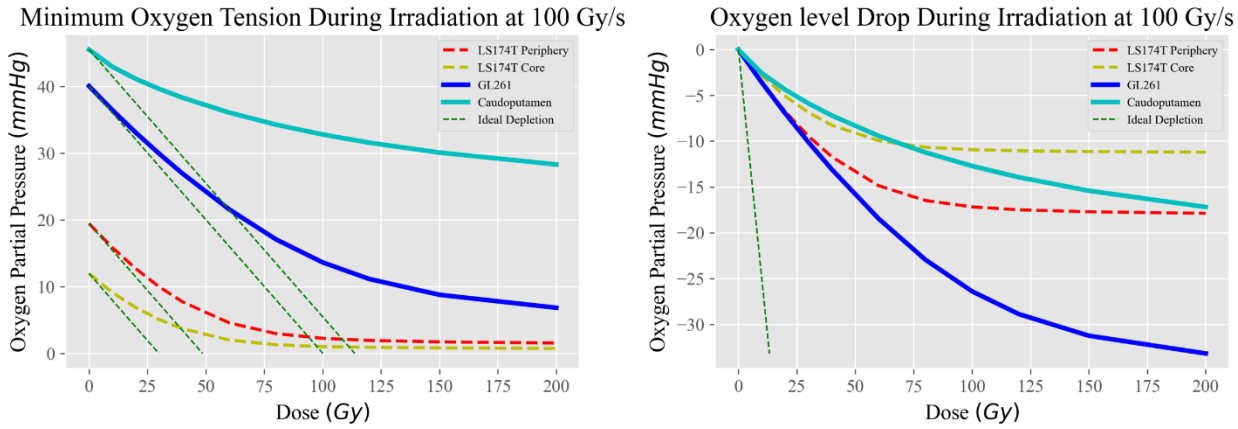

Figure 3-8 Maximum tissue oxygen depletion with varying total dose in 100 Gy/s FLASH irradiation. Left: Absolute oxygen level at the end of irradiation. Right: Absolute oxygen level change compared to steady state at the end of irradiation. A Grey dotted line indicates the scenario of oxygen depleting without the oxygen supply from the vasculature.

Figure 3-9 illustrates the oxygen depletion levels at varying dose rates. A faster delivery rate reduces the time available for oxygen replenishment during irradiation, leading to more efficient oxygen depletion. At conventional dose rates, this depletion effect is not observed; however, the efficiency of depletion dramatically increases with the dose rate and stabilizes at a certain threshold. In less vascularized tissues such as colorectal carcinoma, effective oxygen depletion can be achieved at relatively lower dose rates of 20 Gy/s. For brain glioma, the threshold is around 50 Gy/s, while in extensively metabolizing and vascularized healthy brain tissue, the plateau is not reached even at dose rates as high as 400 Gy/s. These findings are consistent with the established dose rate threshold for FLASH therapy, which is set at 40 Gy/s

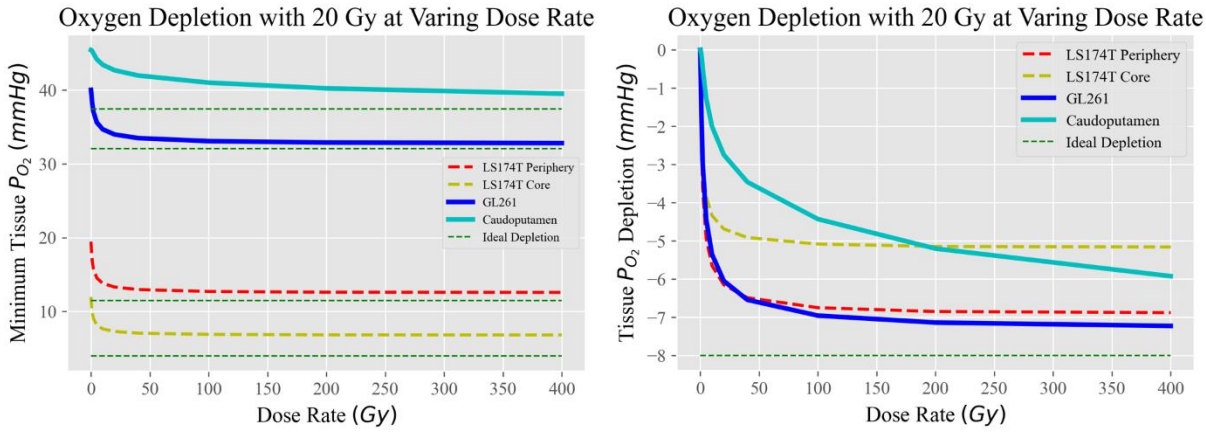

Figure 3-9 Amount of oxygen depletion after the FLASH delivery of 20 Gy with varying dose rates. Left: Absolute oxygen level at the end of irradiation. Right: Absolute oxygen level change compared to steady state at the end of irradiation. A Grey dotted line indicates the scenario of oxygen depleting without the oxygen supply from the vasculature.

3.4. Discussion

While various models have been proposed to simulate tissue oxygenation, none have been capable of handling the complexity and size required for this study. The Krogh model[92], one of the earliest, assumes oxygen diffusion from cylindrical capillaries into surrounding tissue, but is limited to modeling only radial diffusion and is suitable only for tissues with zero-order metabolism, making it inadequate for areas with complex vascular structures and nonlinear metabolisms. Kernel-based methods such as[93] have improved upon the Krogh model by allowing oxygen diffusion in all directions and accommodating more complex vasculature, but they

restrict metabolism modeling to first-order kinetics and do not track intravascular oxygen transportation.

Direct application of Finite Element Method (FEM) or Finite Difference Method (FDM) to the vascularized tissue is also a common approach, such as[94]. However, these methods require extensive meshing and computation to capture the geometry making them improper for large systems.

Yunkai Lu et al.[116] developed an implicit finite-difference method that is able to track vascular oxygen. They use Peskin's numerical delta function to distribute oxygen from vessel centerlines to surrounding voxels, accommodating larger mesh sizes. However, such source distribution does not account for vessel radius but is only voxel size-dependent, which could introduce errors in the physical behavior of oxygen supply. Moreover, the computational demands of this method—requiring over two hours to reach a steady state for a few-thousand-element-vasculature—are not feasible for our purposes.

T.W. Secomb[95] proposed a Green's function method for intravascular and tissue oxygen distribution, later updating it for time-dependent problems[96]Convective transport is simulated by explicitly computing the displacement of fluid elements through the vessel network during the time step. However, due to computational limitations, this method, which involves large influence coefficient matrices, is better suited for small-scale studies.

Our work significantly advances the modeling of time-dependent vascular and tissue oxygen dynamics, particularly in tumor vasculatures which exhibit greater variability in perfusion and hematocrit distribution than normal tissues.

We have developed a method that paralleled the simulation into numerous independent vessel tube ODEs and captures the vasculature structure through a paralleled vessel nodes information gathering step. This approach fully utilizes GPU capabilities to achieve near-real-time computation speeds for ultra-large systems containing tens of millions of voxels and hundreds of thousands of vessel segments without additional memory usage. The vasculature-based oxygenation simulation at this scale has never been achieved before to the best of the author's knowledge.

We have introduced a novel semi-implicit 3D-1D coupling method that efficiently manages oxygen within the vasculature-tissue coupled system. It implicitly models the oxygen release and transport within and across blood vessels and explicitly models oxygen diffusion-reaction in tissue using Finite Difference Methods (FDM). This approach strategically designed the numerical scheme, optimizing both computational efficiency and numerical robustness across highly heterogeneous structural and functional conditions of tumor vasculatures.

We also apply vessel surface sampling to cover the spatial distribution of tube surfaces as oxygen sources, allowing for asymmetric oxygen supply for large vessels that cover heterogeneous tissue regions and a larger time step for transvacular oxygen supply. Such multi-source sampling is fused into our semi-implicit 3D-1D coupling method, and the mass balance in all the steps is explicitly enforced for optimal physiological and physical soundness.

Enabled by our advanced simulation platform, we successfully conducted comprehensive vasculature-based modeling that spans from hemodynamics to vessel-tissue coupled oxygenation. Calibrated against literature values, our results reveal stark oxygen distribution

heterogeneity within tumors and remarkably homogeneous oxygen levels in healthy brain tissue. In poorly vascularized tumors, such as the colorectal carcinoma xenograft, there is a large disparity between blood and tissue oxygen levels, which narrows with increased vascularization, dropping to nearly sub-millimeter mercury levels in healthy caudoputamen vasculature. Despite significant variations in vascularity and tissue metabolism, a consistent mean cross-vessel wall oxygen difference of around 0.8 mmHg is observed across all three vasculature types and varied tissue perfusions, suggesting a uniform per-vessel surface oxygen release rate.

We also assessed the effect of random flow direction initialization on tissue perfusion and oxygen levels. The perfusion of random samples was found to be stable across different samples and the oxygen levels were extremely consistent, with a mean level difference below 0.2%. This demonstrates the robustness of the adopted boundary condition estimation method for blood perfusion and tissue oxygenation modeling tasks.

The relationship between tissue oxygen levels and blood perfusion was also studied. Higher perfusion leads to a faster establishment of a steady state and higher tissue oxygen levels. Tissue oxygen is very sensitive to perfusion levels at the low perfusion range but reaches a plateau at high perfusion levels. Additionally, the mean cross-vessel wall oxygen level difference remains stable across a wide range of perfusion levels. These findings underscore the importance of calibrating tissue perfusion and including explicit intravascular oxygen modeling when examining tissue oxygenation.

In our FLASH depletion modeling, we observed rapid oxygen depletion during irradiation, followed by a gradual recovery. The extent of depletion was significantly lower than in vitro

scenarios, which lack oxygen replenishment from vascular. Our findings reveal an inverse relationship between vascularity and depletion efficiency, underscoring the importance of considering vascular oxygen supply when estimating FLASH depletion. The results also suggest that achieving complete oxygen depletion is impractical with standard dose ranges due to the rapid vascular replenishment, indicating that targeting complete depletion for a FLASH effect is not feasible.

Moreover, we found that depletion levels increased with higher dose rates. The required dose rate for effective oxygen depletion varied from 20 to 50 Gy/s across the studied tumor types, aligning with traditional definitions of FLASH therapy. However, while dose rates above this threshold yielded only marginal gains in depletion for moderately vascularized tissues, in brain tissue, the depletion efficiency plateau did not reach even 400 Gy/s. These findings suggest that while traditional FLASH dose rates are sufficient for normal tissue, higher rates may be more effective in brain tissue.

3.5 Conclusion

Our computation model provided a robust, high-performance modeling platform enabling advanced steady state or time-dependent analysis of the ultra-large-scale and complex dynamically coupled vasculature-tissue system. We demonstrated how well-calibrated functional

properties and heterogeneities can be derived solely based on vasculature structure and reference baseline oxygen consumption rates and tissue perfusions. Our work helps improve the mechanistic understanding of in vivo tissue perfusion and oxygenation and facilitates future ultra-large-scale vascularized tumor growth modeling.

4.Chapter 3: An Ultra-Large Physics-Driven Vascularized Tumor Model to Interpret Macroscopic Tumor Features

4.1 Introduction

Throughout tumor development, the process of angiogenesis, whereby tumors recruit new vasculature from existing vessels, plays an indispensable role in their sustained growth[128]. Without it, avascular tumors that depend solely on metabolite diffusion from surrounding tissues cannot grow beyond 0.2~1 mm[129] in diameter. The tumor vasculature is also known to be morphologically chaotic and functionally impaired compared to normal vasculatures[130]. These characteristics lead to heterogeneous nutrient supply into the tumor microenvironment and further contribute to heterogeneous tumor development. The resultant formation of hypoxic voids, necrosis, and an acidic milieu, which are the basis for imaging tumor heterogeneity with CT[56].

Many computational works have focused on the angiogenesis process during 3d tumor or normal tissue development. Abbas Shirinifard[131] showed asymmetric tumor cell cluster growth toward

vasculature with an agent-based model. Vasileios Vavourakis[132] proposed a hybrid model combining the continuum tumor with discrete vasculature permitting large tissue deformation. Tobias Duswald et al.[133] modeled the tumor growth and treatment response in a dynamic tree-like with an agent-based model using BioDynaMo[69]. JP Alberding et al.[134,135] simulated the angiogenesis in the normal cerebral cortex and retina.

However, aiming at interpreting the macroscopic tumor features of the large heterogeneous tumor development with fully functional vasculature coupled driven heterogeneities, no existing models could fulfill the need. Therefore, we propose our novel ultra-large physics-driven hybrid vascularized tumor model balancing the unbiased ultra-large-scale tumor growth capturing internal heterogeneity with the simulation efficiency enabling high throughput simulations.

In addition, existing models fall short of capturing the macroscopic features of large, heterogeneous tumor development, particularly when considering the complexities introduced by a fully functional, vasculature-driven heterogeneity. To address this gap, we introduce a groundbreaking ultra-large, physics-driven, hybrid vascularized tumor model. Our model achieved a balance, capturing the internal heterogeneity of expansive unbiased vascular tumor growth, while maintaining simulation efficiency to facilitate high-throughput analyses.

4.2 Methods

4.2.1 Overview of Model Design

To model the heterogeneous tumor growth with adequate emphasis on the heterogeneity in tumor oxygenation and cellular density while controlling computational costs, we adopted a hybrid approach, which combines a continuum model for averaged cell behavior in tissue with a discrete model handling the vascular system including its perfusion and development. The continuous tissue and discrete vasculature are coupled so that the tissue mechanically deforms the vasculature as it grows and controls the angiogenesis process through the release of TAF, and the vasculature determines the nutrient supply across the tumorous region. Figure 4-1 shows the brief flowchart illustrating the modeling structure.

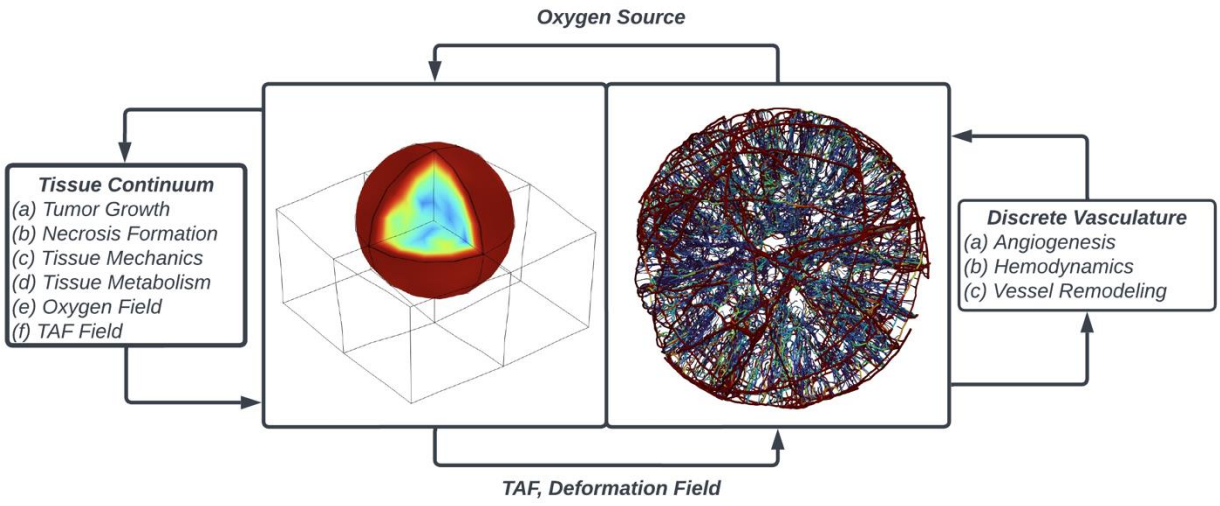

Figure 4-1 Brief flowchart of the model design. The tissue, including the healthy host and tumor, is modeled as a continuum, while vasculature is modeled as discrete nodes and tubes. Vasculature-based oxygen source distribution is generated from a discrete model and provided to the continuum part, while the continuum gives back TAF and tissue deformation information for vasculature update.

In the study, the healthy mouse brain is the reference site for parameters of the healthy host; as for the tumor, mouse glioma (GL261) is the reference type. If available, we will prioritize adopting literature-reported parameters for these specific sites. The following section details the construction of the tissue continuum, biochemical, and vasculature models.

4.2.2 Continuum Tumor Model

4.2.2.1 Tumor Mechanics

To account for the large deformation of the tumor and tissue, a finite strain theory is used. The function $\boldsymbol{x} = \chi(\boldsymbol{X}, t)$ describes that a material point of the tissue (including the tumor and normal tissue) in the reference configuration with coordinate $\boldsymbol{X}$ moves to a location with coordinate $\boldsymbol{x}$ in the current configuration at time *t*. The vectors $d\boldsymbol{X}$ and $d\boldsymbol{x}$ in the reference and current configurations are related by the deformation gradient, defined as $\boldsymbol{F} = \partial \boldsymbol{x}/\partial \boldsymbol{X}$. The deformation gradient can be decomposed into the growth and elastic parts, $\boldsymbol{F} = \boldsymbol{F}^e \boldsymbol{F}^g$, where $\boldsymbol{F}^g$ is the growth component that describes the biological process of growth and $\boldsymbol{F}^e$ is the elastic component that ensures the compatibility of the geometry. Assuming there is no growth in the normal tissue, the corresponding growth tensor $\boldsymbol{F}^g$ of the normal tissue becomes the identity tensor $\boldsymbol{I}$. The determinant of $\boldsymbol{F}$ represents the volume change $J = det(\boldsymbol{F})$. Splitting $\boldsymbol{F}$ yields the split of the volume change $J=J^e J^g$, where $J^e = det(\boldsymbol{F}^e)$ and $J^g = det(\boldsymbol{F}^g)$.

The constitutive response of the tumor and normal tissue is assumed to be hyperplastic. The strain energy density per grown volume $\bar{W}$ is described by the Blatz-Ko free energy function, which is used for characterizing the porous, foam-like rubber material, which is widely used for describing the compressible and nonlinear behavior of tissue and tumor[136]:

$$\bar{W} = \phi\frac{\mu}{2}\left((I_1^e - 3) + \frac{1}{\beta}\left((I_3^e)^{-\beta} - 1\right)\right) + (1-\phi)\frac{\mu}{2}\left(\left(\frac{I_2^e}{I_3^e} - 3\right) + \frac{1}{\beta}\left((I_3^e)^{\beta} - 1\right)\right)$$

Equation 4-1

Where μ is the shear modulus, I_1^e, I_2^e, and I_3^e are the invariants of the strain tensor $\boldsymbol{C}^e = \boldsymbol{F}^{eT}\boldsymbol{F}^e$, given by $I_1^e = tr(\boldsymbol{C}^e), I_2^e = \frac{1}{2}\left(\left(tr(\boldsymbol{C}^e)\right)^2 - tr(\boldsymbol{C}^e \cdot \boldsymbol{C}^e)\right)$, and $I_3^e = det(\boldsymbol{C}^e)$. ϕ and β are non-dimensional parameters, lower ϕ lead to more foam-like behavior and β is related to the Poisson's ratio ν through $\nu = \beta/(1+2\beta)$. While tumors are generally stiffer than normal tissue[137], there are contradictory reports regarding glioblastoma[138]. In this work, we primarily reference Richard Moran et al.[139] and James MacLaurin[136] for normal brain and glioblastoma mechanical properties, respectively.

The relative cell density n_c is estimated as the inverse Jacobian of the elastic deformation gradient $J_e = det(\boldsymbol{F}^e)$, the volumetric oxygen consumption rate and TAF release rate will be scaled accordingly.

The strain energy density per initial volume W is related to $\bar{W}$ through $W = J^g\bar{W}$. The first Piola-Kirchhoff stress is defined as $\boldsymbol{P} = \frac{\partial W}{\partial \boldsymbol{F}}$. The Cauchy stress is related to the first Piola-Kirchhoff stress via $\boldsymbol{\sigma} = \frac{1}{J}\boldsymbol{P}\boldsymbol{F}^T$.

The tissue is assumed to be under mechanical equilibrium and quasi-static deformation. The balance of linear momentum in the Lagrangian framework is written as

$$\frac{\partial}{\partial \boldsymbol{X}} \cdot \boldsymbol{P}^T = 0$$

Equation 4-2

4.2.2.2 Tumor Growth

Assuming isotropic growth of the tumor, the growth tensor is expressed as $\boldsymbol{F}^g = \lambda^g \boldsymbol{I}$, where λ^g is the growth stretch ratio that captures the local tumor mass growth. An evolution equation for the growth is given by:

$$\frac{d\lambda^g}{dt} = \lambda^g \cdot \frac{K_g}{3} \cdot \frac{P_{oxy}}{P_{\lambda 50} + P_{oxy}} \cdot H_V$$

Equation 4-3

Accordingly, the effective proliferation rate (doubling rate) of viable cells writes:

$$r_{pro} = \frac{K_g}{ln(2)} \cdot \frac{P_{oxy}}{P_{\lambda 50} + P_{oxy}}$$

Equation 4-4

The GL261 population doubling time is measured at 20 hours in vitro[140]. However, for in vivo tumors, the acid environment and insufficient oxygen and glucose supply could dramatically

alter the tumor cell proliferation rate[141], the typical tumor doubling time is reported to be 2.4 days[142] with a large variation measured ranging from 1.4 to 6.1 days[143]. Adapting to the reported data, we set the baseline maximum growth rate to have a doubling time of one day.

4.2.2.3 Tumor Necrosis

To track the irreversible necrosis transition, we introduce a cell viability indicator H_V. The lowest oxygen partial pressure experienced by each material point over its growth is tracked with the history variable H, the corresponding $H_V$writes:

$$H_V = f_H(H - P_N)$$

Equation 4-5

Where f_H is the Heaviside step function which returns one if $H \geq P_N$ and zero else wise. The tissue will die and stop growing if its H goes below the critical oxygen partial pressure for necrosis P_N.

Parameter	Description	Value	Unit	Reference

$\boldsymbol{\phi_{Host}}$	Blatz-Ko model parameter	1		Richard Moran et al.[139]
$\boldsymbol{\beta_{Host}}$	Blatz-Ko model parameter	2		Richard Moran et al.[139]
$\boldsymbol{\mu_{Host}}$	Host shear modulus	1	kPa	Richard Moran et al.[139]
$\boldsymbol{\phi_{Tumor}}$	Blatz-Ko model parameter	0.2		James MacLaurin[136]
$\boldsymbol{\beta_{Tumor}}$	Blatz-Ko model parameter	4		James MacLaurin[136]
$\boldsymbol{\mu_{Tumor}}$	Tumor shear modulus	2.7	kPa	James MacLaurin[136]
$\boldsymbol{P_N}$	Critical P_{oxy} for necrosis	0.1	$mmHg$	
$\boldsymbol{\rho}$	Tissue density	1	$^{g}/_{ml}$	
$\boldsymbol{K_g}$	Growth rate	0.693	day^{-1}	See text

$\boldsymbol{P_{\lambda 50}}$	P_{oxy} at half maximum growth rate	10	$mmHg$	See text

Table 4-1 Biophysical parameters used in the tumor growth model.

4.2.3 Oxygen Distribution

4.2.3.1 Oxygen Dynamics in Tumor

Oxygen distribution in homogeneous tissue is governed by the following equation, considering the oxygen diffusion in tissue, the oxygen consumption by tissue, and the oxygen supply through perfused vasculature:

$$\frac{\partial P_{oxy}}{\partial t} = \nabla \cdot \left(D_{oxy} \nabla P_{oxy}\right) - \frac{1}{a_{oxy}} M\left(P_{oxy}\right) + \frac{1}{a_{oxy}} S\left(P_{oxy}\right)$$

Equation 4-6

Where P_{oxy} is the oxygen partial pressure, D_{oxy} and a_{oxy} are oxygen diffusion coefficient and solubility in tissue, respectively. $M\left(P_{oxy}\right)$ is the Michaelis-Menten type tissue oxygen consumption, reads:

$$M(P_{oxy}) = \frac{1}{J_e}\frac{M_{max}P_{oxy}}{P_{oxy} + P_{M50}}$$

Equation 4-7

The Jacobian of the elastic deformation gradient J_e quantifies tissue volume change, and its inverse is employed as an approximation for relative cell density. P_{M50} is the critical oxygen partial pressure when the consumption rate reaches half maximum, it is usually a small value in the range of 0.5-1 mmHg[117]. M_{max} is the maximum oxygen consumption rate, which can vary dramatically across cell types[118]. The base line resting oxygen metabolism rate of the human body, also called the One metabolic equivalent (MET) is 3.5 mlO2/kg/min[119], while that for the human brain can be up to 35 mlO2/kg/min[120]. For rats, according to HM Wiesner[121], compared to humans, the baseline body metabolism is much higher, but the brain oxygen metabolism rate is similar, reports 24.2 mLO2/kg/min and 1.97 μmol/g/min, respectively. For brain glioma, due to The Warburg Effect[122], its metabolism can be significantly lower than that of normal tissue. Daniel Paech et al.[123] measured an average 0.23 ± 0.07 μmol/g/min oxygen metabolism rate for high grade glioma and 0.39 ± 0.16 μmol/g/min for low grade glioma. Based on these literature values, in this work, we adopted a volumetric tumor oxygen metabolism rate M_{max}/a_{oxy} ranging from 2 to 4 mmHg/s. The maximum diffusion distance of oxygen from the vasculature to tissue can be estimated as[144]:

$$L_d = \left(2D_{oxy}a_{oxy}P_{wall}/M_{max}\right)^{1/2}$$

Equation 4-8

A vessel with a blood oxygen partial pressure at the vessel surface of approximately 40 mmHg will yield a diffusion range of around 160 microns.

S is the oxygen supply from sufficiently perfused vasculature, the oxygen supply rate of a vessel segment can be written as[115]:

$$S = A_{vas} \cdot k_{oxy}\left(P_{boxy} - P_{wall}\right)$$

Equation 4-9

Where A_{vas} is the surface area of the vessel segment, P_{boxy} is the blood oxygen partial pressure and is modeled as constant for perfused vessels, and P_{wall} is tissue oxygen partial pressure at the vessel surface. k_{oxy} is the mass transfer coefficient (MTC) for transvascular oxygen release[115]:

$$k_{oxy}(H_D) = 17.7{H_D}^2 - 1.07H_D + 0.672 \; {nlO_2}/{s \cdot cm^2 \cdot mmHg}$$

Equation 4-10

In computation, a cross-wall oxygen partial pressure difference cap P_{cap} is applied to avoid the overestimation of oxygen transportation across the vessel wall due to the limited spatial resolution. In our model, only blood vessels with perfusion higher than 100um3/s and discharge

hematocrit above 0.05 are considered perfused and capable of supporting the tissue oxygen demand; the unperfused vessels are excluded from the oxygen supply.

4.2.3.1 Oxygen Dynamics in Host Tissue

Despite the high degree of microvascular heterogeneity arising from both extrinsic and intrinsic factors, control mechanisms in healthy tissue effectively mitigate variations in oxygen supply, resulting in a relatively stable and adequate oxygen concentration[145]. This observation is supported by studies such as that by Carreau et al.[146], which report low spatial variation in oxygen concentration in various healthy organs, including the brain, muscle, and intestinal tissue. In light of these findings, and also to avoid the need to explicitly model the healthy tissue vasculature, we proposed a dynamic equilibrium oxygen partial pressure distribution in healthy tissue governed by:

$$\frac{\partial P_{oxy}}{\partial t} = \nabla \cdot \left(D_{oxy} \nabla P_{oxy}\right) - \frac{1}{a_{oxy}} M\left(P_{oxy}\right) + \frac{1}{a_{oxy}} S_h \left(P_{boxy} - P_{oxy}\right)$$

Equation 4-11

S_h represents the oxygen supply from healthy tissue vasculature, the value is selected such that the steady state oxygen concentration in normal tissue equals P_{hs} :

$$M(P_{hs}) = S_h\left(P_{boxy} - P_{hs}\right)$$

Equation 4-12

4.2.4 Discrete Vasculature Model

Adhering to the methodology described in Chapter 2, we use node-tube and vertex-edge representations to model tumor vasculature in our vascularized tumor simulations. Recognizing that simulated vasculature is not constrained by resolution limits that might cause abnormally high vertex degrees, as seen in actual tumor vasculature imaging, we have set the maximum degree to three to optimize computational efficiency.

4.2.4.1 Hemodynamics

Following Chapter 2, the same method for hemodynamic calculation is applied to the generated vasculature. In vivo viscosity law and phase separation effect is considered, and iterative flow and discharge hematocrit update is applied on the vertex-edge vasculature data till convergence.

4.2.4.2 Angiogenesis

4.2.4.2.1 Biological Background

Avascular tumors, which rely solely on the diffusion of metabolites from the surrounding environment, are generally limited to a growth size of 0.2 to 1 mm[129]. Sustained tumor development necessitates angiogenesis: the formation of new blood vessels from existing vasculature that penetrate the cancerous growth to supply nutrients and oxygen.

Typical sprouting angiogenesis begins with the formation of a sprout, wherein an endothelial cell is activated by elevated concentrations of angiogenic factors secreted by hypoxic tissue, thereby transforming into a tip cell. This tip cell then actively migrates toward the hypoxic area guiding the stalk-cell-proliferation-driven sprout elongation. When two tip cells meet, the two sprouts will fuse and create a lumen through which oxygenated blood can flow and supply the hypoxic regions[147].

While other factors like fibroblast growth factor, tumor necrosis factor (TNF), transforming growth factor (TGF), matrix metalloproteinases (MMPs), and angiopoietins also play roles in angiogenesis[148], VEGF family remains the critical factors in hypoxia-induced angiogenesis. VEGF-A is the most potent blood vessel growth inducer known to date, both necessary and sufficient to induce endothelial tip cells[149], control the stalk cell proliferation through its concentration, and guide the tip cell migration through its concentration gradient as shown by Holger Gerhardt et al[150].

4.2.4.2.2 Continuous TAF Field

In our model, we introduce a single, unitless, homogenized chemical modulator—referred to as Tumor Angiogenic Factor (TAF)—to represent essential activities needed for the development of vascular networks, particularly those influenced by VEGF-A.

The concentration of TAF (C_{TAF}) in tissue is governed by:

$$\frac{\partial C_{TAF}}{\partial t} = \nabla \cdot (D_{TAF} \nabla C_{TAF}) + S_{TAF} - K_{TAF} C_{TAF}$$

Equation 4-13

Where D_{TAF} is the diffusion coefficient of TAF in tissue, λ_{TAF} is the degradation rate. Following JP Alberding et al.[134] we model the TAF release from hypoxic tissue as:

$$S_{TAF} = \begin{cases} \frac{1}{J_e} K_{TAF} C_{max} \left(1 - \frac{P_{oxy}}{P_{TAF}}\right) \cdot H_V & if\ P_{oxy} \leq P_{TAF} \\ 0 & else \end{cases}$$

Equation 4-14

Where C_{max} is the maximum TAF concentration and K_{TAF} is degradation rate. P_{TAF} is the tissue oxygen partial pressure threshold to initiate the TAF release. The viability indicator multiplied in this term reflects the assumption that necrotic tissue is unable to secrete angiogenic factors.

4.2.4.2.3 Sprout Activation, Migration, and Anastomosis

The activation of an endothelial cell into a tip cell is modeled as a stochastic process, modified from Alberding et al.[134] the probability of the sprout formation on a vessel segment with in a time interval Δt can be written as:

$$P_{sprout} = k_{sprout} L \Delta t \frac{C_{TAF} - C_{th}}{C_{TAF50} + C_{TAF} - 2C_{th}}$$

Equation 4-15

Where k_{sprout} is the maximal sprout rate per unit length, L is the length of the vessel segment, C_{th} is the TAF concentration threshold for sprout formation, and C_{TAF50} is the TAF concentration at which the probability of sprouting reaches half-maximum. The new sprout is randomly placed on the activated vessel segment and has a fixed radius R_{sprout}. If the environmental TAF is about the threshold C_{mig}, the stalk cells will be allowed to proliferate resulting in the sprout elongating at a constant speed V_{sprout} if; otherwise, sprout elongation will come to a halt. Levi B. Wood et al.[151] found a wide distribution of nascent vessels ranging from 5 to 25 microns, and the spout elongation speed ranging from 25 to 75 micros a day, with smaller radius vessels growths faster. According to this observation, we assign a tip cell migration speed of 75 μm/day in the model.

The directional sprout elongation is controlled by tip cells, which is influenced by three primary factors: the previous direction, the local TAF gradient, the anastomosis bias, and the random variation. The new migration direction $\boldsymbol{n}_{new}$ updated from previous direction $\boldsymbol{n}_{old}$ goes:

$$\boldsymbol{n}_{new} = \frac{\boldsymbol{n}_{old} + k_{TAF}\,\nabla C_{TAF}/\|\nabla C_{TAF}\|_2 + k_{ana}\boldsymbol{n}_{ana} + k_{rand}\boldsymbol{n}_{rand}}{\|\boldsymbol{n}_{old} + k_{TAF}\,\nabla C_{TAF}/\|\nabla C_{TAF}\|_2 + k_{ana}\boldsymbol{n}_{ana} + k_{rand}\boldsymbol{n}_{rand}\|_2}$$

Equation 4-16

$\boldsymbol{n}_{ana}$ is the vector indicating anastomosis bias and $\boldsymbol{n}_{rand}$ is a random 3D unit vector for random variation. k_{TAF}, k_{ana}, and k_{rand} serve as the weights for the TAF gradient term, anastomosis bias term, and random variation term, respectively. Adjusted from the work of Secomb et al.[152], we model the anastomosis bias for an arbitrary tip cell a in a form that is both distance- and angle-dependent:

$$\boldsymbol{n}_{ana,a} = \sum_{\beta \in S_{cone,a}} \frac{\boldsymbol{r}_{\alpha,\beta}}{\|\boldsymbol{r}_{\alpha,\beta}\|_2}\left(1 - \frac{\|\boldsymbol{r}_{\alpha,\beta}\|_2}{D_{ana}}\right)\left(\frac{cos(\theta_{\alpha,\beta}) - cos(\theta_{ana})}{1 - cos(\theta_{ana})}\right)$$

Equation 4-17

Where β refers to other tip cells belonging to the set $S_{cone,a}$, which includes all the tip cells that can be sensed by tip cell α. The vector $\boldsymbol{r}_{\alpha,\beta}$ points from tip cell α to tip cell β, and $\theta_{\alpha,\beta}$ represents the angle between the sprout orientation and $\boldsymbol{r}_{\alpha,\beta}$. A tip cell is 'sensible' by another if it can be reached by the filopodia. The majority of filopodia is found to be shorter than 75 micron

in in vitro experiments [150], so we set the tip sense length limit D_{ana} accordingly. Meanwhile due to forward extending morphology of filopodia, a tip sense angle limit θ_{ana} is also applied. When two tip cells come within a proximity of no more than the anastomosis threshold L_{ana}, their migration ceases, and a vessel segment will be placed to connects the two tip cells, thereby establishing a lumen for blood perfusion.

4.2.4.3 Vasculature Remodeling

4.2.4.3.1 tissue-induced motion

In our model, the vasculature is embedded within deforming tissue and adapts its shape and length accordingly. The movement speed of a vasculature vertex located at position $\boldsymbol{x}$ with the deformation of tissue can be written as

$$\boldsymbol{v}(\boldsymbol{x}, t) = \boldsymbol{V}(\boldsymbol{\phi}^{-1}(\boldsymbol{x}, t), t)$$

Equation 4-18

Where $\boldsymbol{\phi}$ is the deformation function mapping the material space to world space, and $\boldsymbol{\phi}^{-1}$ is its inverse. $\boldsymbol{V}$ denotes the velocity of the tissue as defined in material space. Due to the substantial

tissue deformation caused by tumor growth, some vessel segments may be stretched to long lengths and lose the ability to capture vessel tortuosity. To maintain modeling accuracy, we insert extra vertices to ensure that the length of each vessel segment remains approximately 20 microns.

4.2.4.3.2 Angular Remodeling

In addition to tissue-induced motion, we account for the potential of vessels to move through tissue due to longitudinal tension[153] [154]. This mechanism helps to align the branching angles closer to 120 degrees, as observed in microvascular networks[152]. The resultant 'force' of vessel tensions acting at each network vertex can be modeled as[134]:

$$\mathbf{f}_t = \frac{(\sum D_i \boldsymbol{n}_i)(\sum D_i)}{\sum D_i L_i}$$

Equation 4-19

i indexes the vessel segments connecting to the examined vertex, D and L represent the corresponding vessel diameter and length. $\boldsymbol{n}$ is the unit vector indicating vessel orientation, taking the examined vertex as the starting point. They will migrate if the net force exceeds a threshold F_{th}:

$$\boldsymbol{v} = v_{bamax}\mathbf{f}_t\left(1 - \frac{F_{bath}}{\|\mathbf{f}_t\|_2}\right)$$

Equation 4-20

Where v_{bamax} is the maximum velocity, keeping this velocity relatively low is very important for the numerical stability of branching angle remodeling. The threshold F_{bath} is included to prevent the vasculature from losing its curved structures[152].

4.2.4.3.3 Radius Remodeling and Pruning

Functional vasculatures are known to prefer certain wall shear stress (WSS) as a consequence of minimizing power required for maintaining the flow volume combined with the power to pump the flow. Pries et al.[155] found that the WSS of vessel is regulated according to blood pressure despite their flow rate, radius, or vessel type. As a reminder, the wall shear stress of a vessel segment can be calculated from:

$$\tau_w = \frac{R\Delta P}{2L} \; or \; \frac{4\mu Q}{\pi R^3}$$

Equation 4-21

Where R is the vessel radius, L is the vessel length, ΔP is the blood pressure drop over this segment, Q is the blood flow rate going through, and μ is the apparent viscosity of blood. The WSS regulation is later applied to the estimation of blood flow in the given healthy vasculatures structures[91], and the vessel remodeling of healthy vasculature[152]. However, a significant pressure-WSS relationship is not observed in the large chaotic tumor vasculatures even when boundary pressure is optimized accordingly[107]. Furthermore, the numerical adjustment of radius according to WSS is only effective with fixed flow boundary conditions but numerically unstable for pressure-based boundary conditions. Specifically, it tends to encourage the enlargement of radius differences between serially connected vessel segments. In our model, we favor the latter form of boundary condition, where the boundary flow is not predetermined, and tumor perfusion is an emergent functional property from the vasculature structure.

We propose a novel radius remodeling scheme based on both target WSS and target radius, that is table for the pressure boundary condition. The radius adaptation signal S_{tot} is designed to have the following properties. First, for vessels with zero flow, their radius will gradually decrease to r_{min}. Second, for perfused vessels, the higher flow rate will encourage a larger vessel radius post adaptation. Third, when vessels reach the reference WSS τ_{ref}, the adaptation signal will become zero. The radius adaptation and adaptation signal are defined as follows:

$$\frac{\Delta R}{\Delta t} = \frac{S_{tot} R}{T_a}$$

Equation 4-22

$$S_{tot} = log\left(\frac{(10^{n_r} - 1)|Q| + Q_{ref}}{10^{n_r} Q_{ref}}\right) + n_r \frac{log\left(\frac{R_{ref}}{R}\right)}{log\left(\frac{R_{ref}}{R_{min}}\right)}$$

Equation 4-23

Where T_a is the adaptation time controlling the adaptation rate, n_r is a weighting factor for both the target radius and the flow regularization. R_{ref} is the reference radius and R_{min} is the mnininum radius allowed. The reference flow Q_{ref} is calculated on individual vessel based on a reference WSS:

$$Q_{ref} = \tau_{ref} \frac{\pi r^3}{4\mu}$$

Equation 4-24

The radius adaptation signal S_{tot} is designed in this way so that for vessels with zero flow, their radius will gradually decrease toward r_{min} at a programed speed, while for perfused vessels, the radius is positively regulated by its flow and will attempt to approach the reference WSS. In vivo measurement of blood flow velocity in mice brain suggests 1 and 5.6 mm/s for capillaries and arterioles repectively[156], and perfusion calibrated GL261 tumor have a mean WSS around 15 dyn/cm^2 [100] and radius around 12 μm.

The flow-radius relationship curve of a constant WSS of 15 dyn/cm^2, and the curve of a constant flow velocity at 1.5 mm/s is plotted in Figure 4-2. Their intersection point shows a radius of 12 μm, which is selected to be the reference radius R_{ref} in our remodeling module. With boundary

pressure condition applied accordingly, the environmental host vasculature would be encouraged to have a physiological hemodynamic property of WSS, radius, and flow velocity as the intersection point.

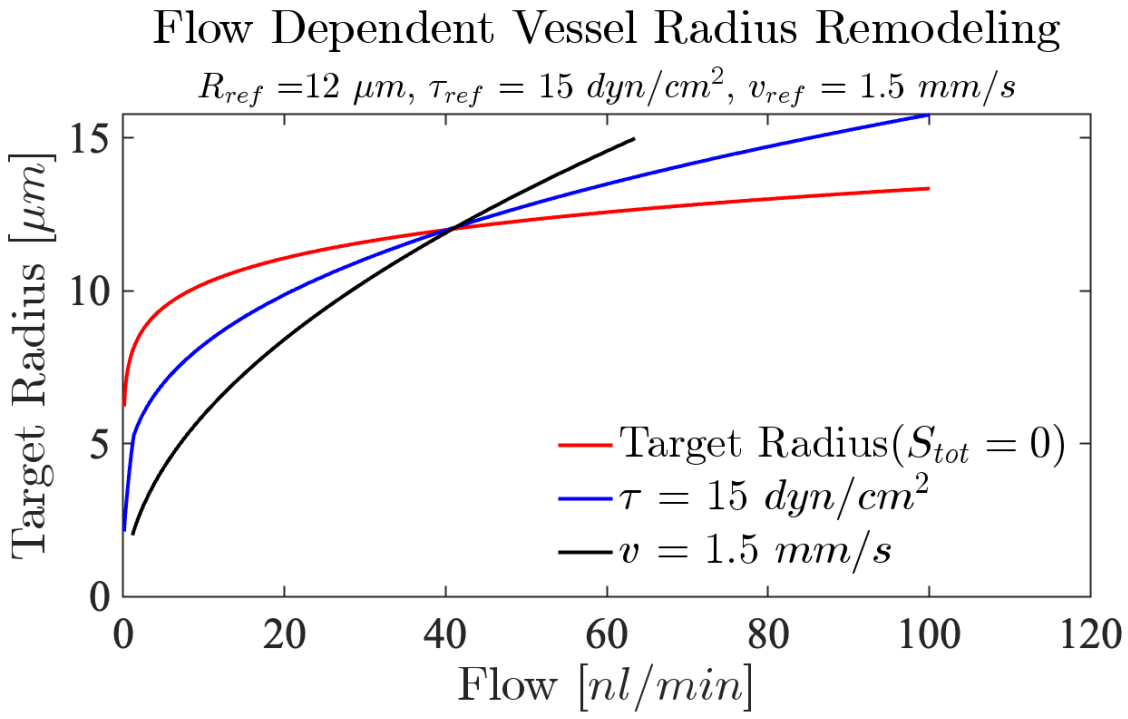

Figure 4-2 The curve for the radius remodeling under various flow conditions. The blue curve shows the reference wall shear stress at 15 dyn/cm^2, black curve shows the constant flow velocity curve at 1.5 mm/s, the intersection radius at 12 μm is made the reference radius R_{ref} in radius remodeling.

4.2.4.4 Host Vasculature Initialization

The vascularization through angiogenesis requires pre-existing host vasculature to start with. Common methods establishing host vasculature includes the cubic grid vasculature[131], parallel vessels arrays[132], and reduced vasculature data containing a few major vessels[133]. However, existing methods can hardly fulfill our need for unbiased tumor growth. The artificial vessel arranged as cubic grid or paralleled lines could introduce bias in certain growth direction while the density of reduced vasculature could be inadequate for nutrition supply and angiogenesis initiation. Ideally, the entire vasculature extracted from normal tissue is preferred for host vasculature initialization, however, with the scarcity of data availability and the cost of handing a much larger simulation region and vasculature size, makes it currently impractical. As an alternative approach, we propose a novel spatially stratified tangent vessel method for host vasculature initialization. This method provides a simple and theoretically unbiased vascular environment for tumor development and allows for random sampling to further annihilation the risk of directional growth bias introduced error in statistical analysis.

In our model, the initial tumor assumes a spherical shape with a radius $R_{Tumor}^{init} = 150$ μm. The environmental vasculature surrounding the tumor is organized as tangent lines on an extended sphere situated $L_{S2V}^{init} = 50$ μm away from the tumor surface. Both the tangent points and vessel orientations on the tangent plane are randomly sampled. To mitigate the risk of large vessel-starved areas, which are not physiologically reasonable in a healthy host, we implement a stratification strategy. This involves sampling the tangent points part by part within uniformly divided subregions on the surface of the sphere. Each initialized vessel is 6 μm in radius, with a total length of $L_{HostVes}^{init} = 1000$ μm.

4.2.4.5 Boundary Blood Pressure

The boundary blood pressure assignment is also crucial for proper perfusion and the downstream vessel remodeling estimation. For a static system, convex optimization method considering the WSS under a mass conservation constraint[91] could be used to estimate the boundary pressure, however, the optimization based estimation is impractically expensive for an evolving vasculature.

Tailer to our dynamic development task and the specific host vasculature morphology, we introduce a novel location-encoded blood pressure assignment method to determine the inlet and outlet blood pressures of the vasculature under significant deformation. This method incorporates two key components.

Distance-to-center-based baseline pressure term: This term adjusts the blood pressure based on the distance from the vessel center. This ensures a progressive increase in pressure difference between the inlet and outlet as the vessel length extends.

Angular-position-based pressure variation term: This term introduces a blood pressure shift for host vessels with different orientation and facilitates the establishment of appropriate pressure gradients within neo-vasculatures connecting different host vessels, especially in the central region.

For the location-encoded blood pressure assignment method, the initial step involves estimating the vessel length based on the position of the inlet or outlet. We assume that throughout the near-spheroidal tumor growth, for the host vessel ends, their distance to tumor surface and angular position with respect to tumor center remains constant. And for other parts in host vasculature, their distance to tumor surface do not drop below initial surface to vessel distance L_{S2V}^{init}. Based on these assumptions, we introduce another geometric approximation to decompose any host vessel into three components: one circular arc component on the extended sphere surface, and two tangent line components connecting the vessel ends and the arc.

The constant host vessel end to tumor surface distance and the constant angle between two ends of a host vessel with respect to the tumor center throughout the tumor development is:

$$L_{S2E} = \sqrt{\left(R_{Tumor}^{init} + L_{S2V}^{init}\right)^2 + \left(\frac{L_{HostVes}^{init}}{2}\right)^2} - R_{Tumor}^{init}$$

Equation 4-25

$$\theta_{ECE} = 2arctan\left(\frac{L_{HostVes}^{init}}{2\left(R_{Tumor}^{init} + L_{S2V}^{init}\right)}\right)$$

Equation 4-26

Then as the tumor grows, the estimated distance from tumor center to the arc sphere at time t goes:

$$L_{C2V}^{t} = L_{C2E}^{t} - L_{S2E} + L_{S2V}^{init}$$

Equation 4-27

Where L_{C2E}^{t} represents the distance from the evaluated vessel end to the tumor center at time t, which is the only required variable. The angle between vessel end and the corresponding tangent point goes:

$$\theta_{ECT}^{t} = \arccos\left(\frac{L_{C2V}^{t}}{L_{C2E}^{t}}\right)$$

Equation 4-28

And the total length of the deformed host vessel is written as:

$$L_{vas}^{t} = 2L_{C2E}^{t}(\theta_{ECE} - \theta_{ECT}^{t} + \sin(\theta_{ECT}^{t}))$$

Equation 4-29

Finally, the baseline pressure term goes:

$$P_{D2C}^{t}(L_{vas}^{t}) = \pm\, \kappa_{D2C}\frac{L_{vas}^{t}}{2} + P_{ref}$$

Equation 4-30

Where P_{ref} is the reference mean blood pressure of the vasculature, κ_{D2C} is the gradient for distance-based blood pressure term, which is determine according to the reference WSS and radius of the vasculature. Sign in the first term determines the flow direction which is randomly assigned during initialization with a positive gradient for inlet and a negative for outlet.

The angular position of the vessel end can be calculated as:

$$\theta_{C2E}^{t} = arccos(\hat{\boldsymbol{n}}_{C2E}^{t} \cdot \hat{\boldsymbol{z}})$$

Equation 4-31

$$\varphi_{C2E}^{t} = arctan\left(\frac{\hat{\boldsymbol{n}}_{C2E}^{t} \cdot \hat{\boldsymbol{y}}}{\hat{\boldsymbol{n}}_{C2E}^{t} \cdot \hat{\boldsymbol{x}}}\right)$$

Equation 4-32

Where $\hat{\boldsymbol{n}}_{C2E}^{t}$ is the unit vector pointing from tumor center to the vessel end, θ is the polar angle and φ is the azimuthal angle. $\hat{\boldsymbol{x}}$, $\hat{\boldsymbol{y}}$, and $\hat{\boldsymbol{z}}$ are unit axis vectors of the cartesian coordinate system.

The angular-position-based pressure term goes:

$$P_{\text{angle}}^{t} = c_{angle}\kappa_{D2C}\frac{L_{C2E}^{t}}{\sqrt{2}}[\cos(2\theta_{C2E}^{t}) + \sin(2\theta_{C2E}^{t})\sin(2\varphi_{C2E}^{t})]$$

Equation 4-33

Where c_{angle} represents the relative strength of angular variation compared to the baseline gradient term. This low-frequency angular term ensures that vessel ends positioned at approximately opposite angles share similar pressure variation values. This guarantees approximately constant blood pressure gradients for all host vessels throughout their growth.

All the biophysical parameters related to vasculature and oxygenation are listed in Table 4-2.

Module	Parameter	Description	Value	Unit	Reference
Oxygen	D_{oxy}	Oxygen diffusion coefficient	2410	$\mu m^2 s^{-1}$	Bentley et al.[157]
	a_{oxy}	Oxygen solubility	38.9	$nlO_2 ml^{-1} mmHg^{-1}$	Bentley et al.[157]
	ρ	Tissue mass density	1000	$kg \cdot m^{-3}$	
	M_{max}	Max oxygen consumption	2-4	$mmHg \cdot s^{-1}$	See text

	P_{M50}	P_{oxy} with half - maximum consumption	1	$mmHg$	Goldman[117]
	P_{boxy}	Blood P_{oxy}	35.5	$mmHg$	
	P_{hs}	Steady state host tissue P_{oxy}	35	$mmHg$	Carreau et al.[146]
	P_{cap}	Max oxygen pressure difference across vessel wall	1	$mmHg$	
Perfusion	μ_0	Apparent viscosity of rat blood at 37℃	1.05	$mPa \cdot s$	Pries et al.[90]
	P_{ref}	Reference mean blood pressure	40	$mmHg$	
	κ_{D2C}	Gradient for distance-based blood pressure term	1.8752	$mmHg \cdot mm^{-1}$	

	c_{angle}	Relative strength of angular blood pressure variation	2		
TAF	C_{max}	Max TAF concentration	1		
	D_{TAF}	TAF Diffusion coefficient	20	$\mu m^2 s^{-1}$	Alberding et al.[134]
	K_{TAF}	TAF decay rate	0.002	s^{-1}	Adapted from Alberding et al.[134]
	P_{TAF}	Tissue P_{oxy} where cells start to release TAF	34.5	$mmHg$	
Angiogenesis	k_{sprout}	Maximum sprout rate per length	0.05	$\mu m^{-1} day^{-1}$	

	C_{TAF50}	C_{TAF} for half-maximal sprout rate	0.33		
	C_{th}	C_{TAF} threshold for sprout formation	0.01		
	C_{mig}	C_{TAF} threshold for stalk cell proliferation	0.01		
	R_{sprout}	Radius of sprout	6	μm	
	V_{sprout}	Velocity of sprout elongation	75	$\mu m \cdot day^{-1}$	Levi B. Wood et al.[151]
	k_{TAF}	Weight for TAF gradient	1		
	k_{ana}	Weight for anastomosis bias	1		
	k_{rand}	Weight for random variation	0.5		

	D_{ana}	Maximum tip cell sensing distance	75	μm	Gerhardt [150]
	θ_{ana}	Maximum vessel sensing angle	$\pi/3$		Secomb et al.[152]
	L_{ana}	Anastomosis threshold	25	μm	
Remodeling	v_{bamax}	Branching angle remodeling velocity	1	$\mu m \cdot h^{-1}$	
	F_{bath}	Branching angle remodeling threshold	0.25		JP Alberding et al.[134]
	T_s	Structural adaptation coefficient	192	day	
	n_r	Adaptation weighting factor for reference radius	4		

	R_{ref}	Reference radius in adaptation	12	μm	
	τ_{ref}	Reference wall shear stress	15	$dyn \cdot cm^{-2}$	Secomb et al.[91]
Initialization	R_{Tumor}^{init}	Initial tumor radius	150	μm	
	L_{S2V}^{init}	Initial tumor surface to host vasculature distance	50	μm	
	$L_{HostVes}^{init}$	Initial host vasculature length	1000	μm	
	$N_{HostVes}^{init}$	Initial host vessel number	50		
	L_{Host}^{init}	Initial host tissue cube length	4000	μm	

Table 4-2 Biophysical Parameters related to vasculature and oxygenation.

4.2.5 Model Implementation

The continuum mechanics of tissue and diffusion-reaction equations of oxygen and TAF are solved in COMSOL Multiphysics® (v6.1) using its fully coupled solver, and the vasculature development and functional modeling are handled in MATLAB® (R2023b) with in-house developed code, the communication between two software is through LiveLink™. The step size of COMSOL is adaptive and automatically determined by COMSOL, that for vasculature development and hemodynamics calculation is 2 hours on MATLAB. Communication between two software happens every 12 hours. The implementation details are shown in Figure 4-2.

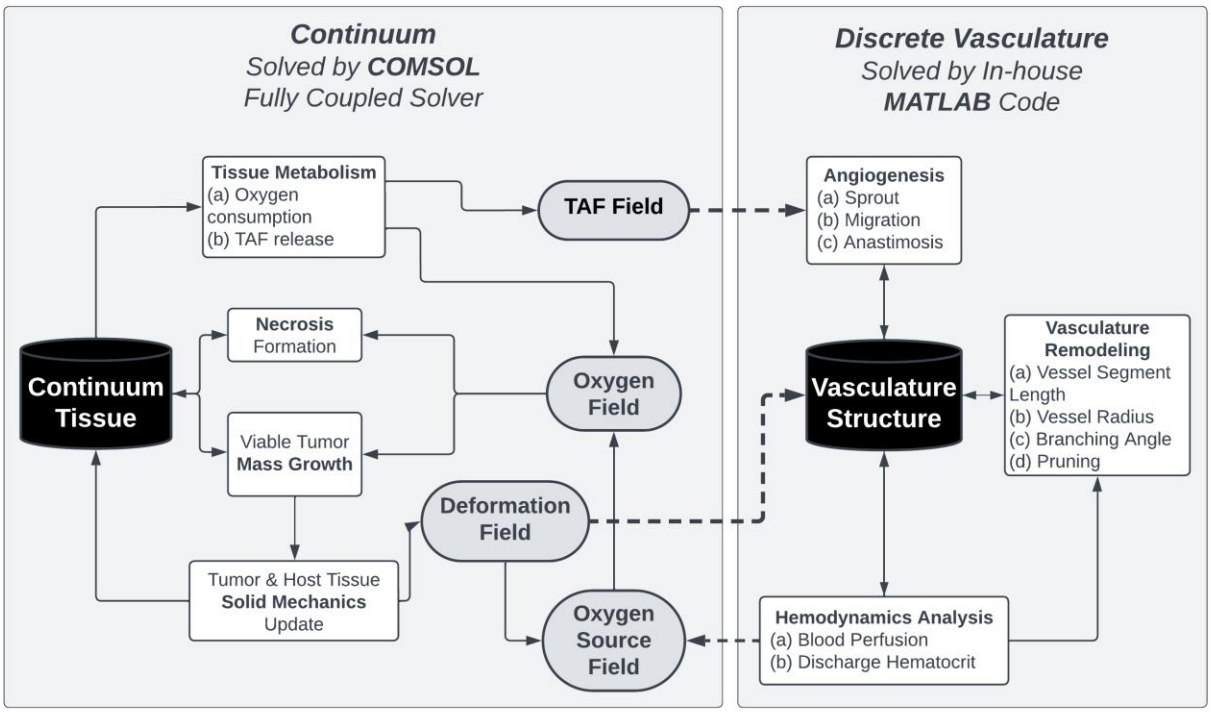

Figure 4-3 Flowchart for Model Implementation.

4.2.6 Tumor Property Map Generation

At the conclusion of the simulation steps, crucial tumor development data are transferred from COMSOL to MATLAB. This data, originally in a tetrahedral finite element mesh, is interpolated onto a Cartesian grid with isotropic voxels, each 50, 100, or 150 microns in size, using MATLAB's 'griddata' function. This process prepares the data for in-depth tumor characterization and analysis. Subsequently, comprehensive property maps are generated on this grid and analyzed, covering various aspects such as tumor and necrosis segmentation, distributions of tissue oxygen partial pressure, cell density, metabolism intensity, hypoxia, proliferation activity, as well as voxel-wise distributions of tissue perfusion and blood volume fraction. Direct analysis of ground truth property maps that are free from the sign-to-noise ratio, contrast mechanisms, and resolution limit allows us to focus on identifying the most informative properties and optimal resolution for investigation, potentially providing insights to guide imaging choices and development.

Although the property maps generated for analysis are not meant to mimic medical images but are ground truth directly calculated from the simulation results, these properties have the potential to be non-invasively imaged in vivo. For instance, cell density might be inferred from ADC MRI, which provides information on the extracellular fluid fraction, or from CT scans that reflect atomic composition. Tissue blood perfusion and volume could be captured using various imaging modalities with contrast agents, while extracellular oxygen levels might be gauged through Electron Paramagnetic Resonance (EPR)[158] imaging. Tissue hypoxia could be visualized

using 18F-Fluoromisonidazole (FMISO) PET[159], oxygen metabolism through Oxygen-17 MRI[123], and proliferation rates through [18F]-FLT-PET[160]. Table 4-3 listed possible modalities that could potentially reflect the tumor properties of interest.

Property Map	Imaging Modality
Cell Density	CT, ADC MRI
Oxygen Level	EPR[158]
Oxygen Metabolism	Oxygen-17 MRI
Volumetric Proliferation Rate	[18F]-FLT-PET[160]
Hypoxia	FMISO[159]
Tissue Perfusion	Perfusion CT, Perfusion MRI
Blood Volume	Perfusion CT, Perfusion MRI

Table 4-3 Imaging modalities reflecting tumor properties.

The cell density map presents a relative estimation of solid tissue mass density, whose voxel intensity is defined as:

$$I_{\rho} = \frac{1}{J_e}$$

Equation 4-34

The oxygen metabolism map is calculated as the relative volumetric oxygen consumption rate, aligned with the volumetric oxygen consumption rate term in the oxygenation simulation, defined as:

$$I_{OCR} = \frac{1}{J_e} \frac{M_{max} P_{oxy}}{P_{oxy} + P_{M50}}$$

Equation 4-35

Similarly, the volumetric proliferation activity map measures the proliferation events within a voxel:

$$I_{pro} = \frac{1}{J_e} \frac{P_{oxy}}{P_{\lambda 50} + P_{oxy}} \cdot H_V$$

Equation 4-36

The hypoxia map in our study is designed to replicate the signal observed in 18F-Fluoromisonidazole (FMISO) PET imaging. While this map reflects tissue oxygen levels, it specifically highlights regions of low oxygenation and deliberately excludes necrotic areas from contributing to the signal. Consequently, it offers distinct insights with a particular emphasis on

hypoxic yet viable tissue regions. The binding rate of FMISO as a function of oxygen partial pressure for living cells is given as[54]:

$$k_b(P_{oxy}) = \frac{1}{J_e}\frac{k_{b0}P_{50b}}{P_{oxy} + P_{50b}} \cdot H_V$$

Equation 4-37

Where k_{b0} is the maximum binding rate at $k_{b0} = 4.5 \times 10^{-4}\ s^{-1}$, and P_{50b} is the oxygen level at the half-maximum binding rate, given as 1.4 mmHg.

4.3 Results

A series of simulations are performed with a range of growth rate and oxygen consumption rate parameters, based on literature values. Initialized as a 300-micron-diameter sphere at the center of the cubic host tissue, the simulation stops when the tumor volume reaches around 12 mm^3. Which takes from 12 to 28 days mainly based on growth rate settings. The quantitative and qualitative characteristics of the vasculature and the tumor tissue are analyzed and compared. Additionally, a set of tumors 12 with random parameters is generated, and a Radiomics model is generated to identify features that differentiate the tumor growth rate as well as the oxygen consumption rate (OCR).

4.3.1 Simulation Results of the Baseline Tumor

The baseline tumor, with a doubling time of 24 hours and an oxygen consumption rate of 3 mmHg/s, grew from 0.0133 mm^3 to 13.064 mm^3 over 14 days. This corresponds to an equivalent daily growth ratio of 63%, aligning with the fast-growing small in vivo gliomas as documented in[143], where the observed daily growth ranged from 13% to 63%. The tumor volume growth curve, depicted in Figure 4-4 (a), exhibits an exponential trend. In this baseline scenario, the tumor does not develop central necrosis, attributed to the early establishment of vasculature during the initial tumor growth stages. The quantitative summary of the tumor and tumor vasculature is available in Table 4-4.

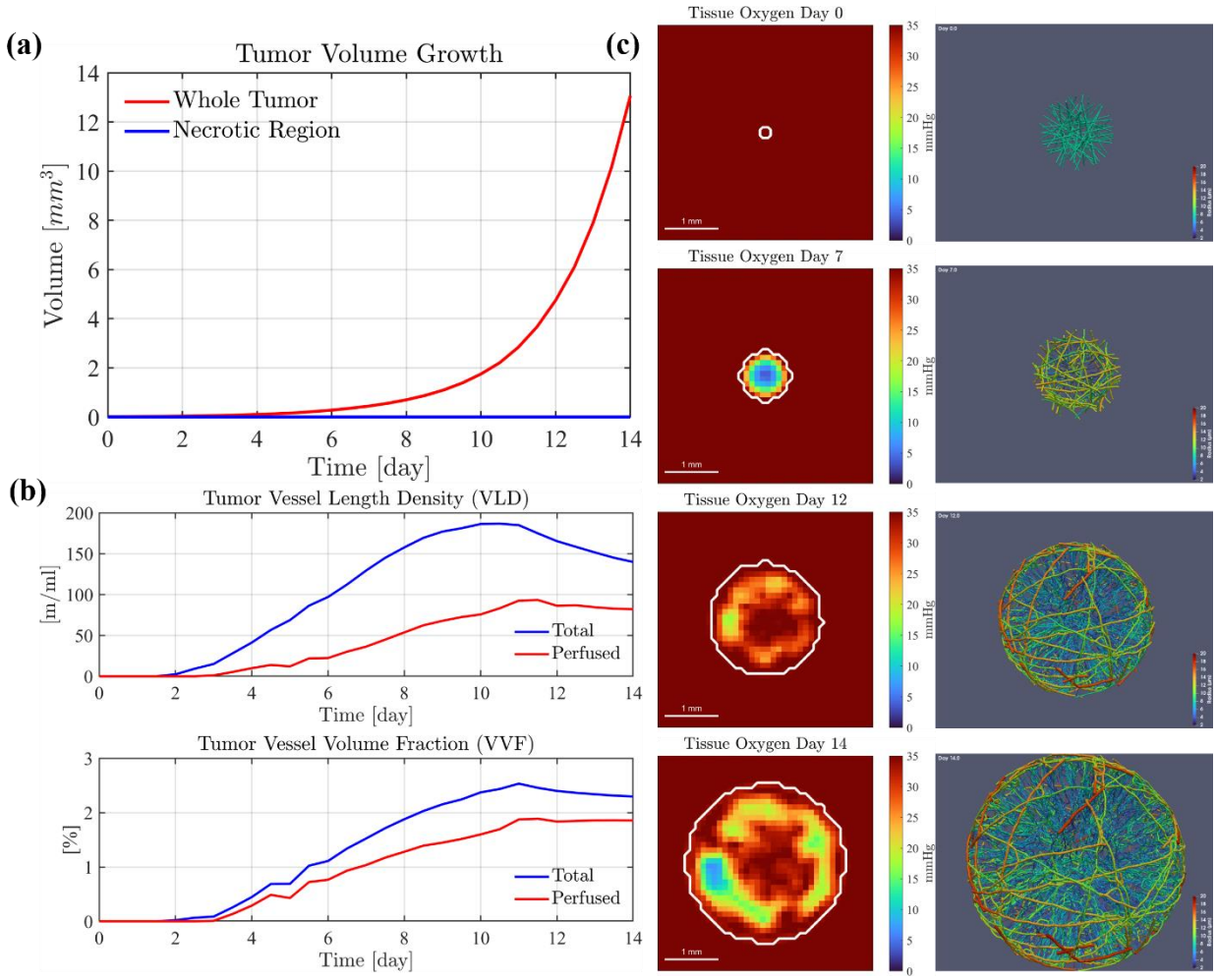

Figure 4-4 (a) The tumor volume growth curve, highlighting the lack of necrosis in this baseline case. (b) The tumor vasculature density throughout the growth period. (c) Sequential images from top to bottom, presenting tissue oxygen levels and vasculature structure on days 0, 7, 12, and 14 respectively. The left column depicts the central slice oxygen partial pressure with a voxel size of 100 microns. The white line delineates the tumor boundary. The right column showcases the rendered vasculature structure, with vessels color-coded according to their radius.

Figure 4-4(b) depicts changes in tumor vasculature density, distinguishing between perfused and unperfused vessels. Vessel segments with flow below 100 um³/s or discharge hematocrit under

0.05 are deemed incapable of oxygen delivery, termed 'unperfused.' These may include nascent sprouts awaiting anastomosis or poorly structured self-looping or shunt bypassing vessel regions. As the tumor grows, vascular density initially increases, then stabilizes, with the mean density of perfused vessels remaining constant and unperfused vessels being progressively pruned. Despite a stable global mean vascular density in this plateau phase, oxygen levels remain spatially heterogeneous, influenced by local variations in oxygen demand and supply. Figure 4-4(c) showcases sequential central slice images of tissue oxygen levels on days 0, 7, 12, and 14, alongside rendered vasculature, with oxygen partial pressure data derived by interpolating from finite element simulations to 100-micron isotropic voxels.

Initially, a hypoxic core forms due to limited oxygen diffusion, prompting outward deformation of the surrounding vasculature and angiogenesis induced by hypoxia-inducible factors from hypoxic cells. Over time, the tumor vasculature evolves into a complex network that, while preventing necrosis, fails to maintain uniform physiological oxygen levels throughout the tissue. By the conclusion of the simulation, the oxygen tension within the tumor decreased from 35 to 27.7 mmHg, with a standard deviation of 6.7 mmHg. Notably, oxygen levels dropped to as low as 5 mmHg in the tumor's peripheral regions due to increased cell density caused by growth-induced mechanical compression. In contrast, the tumor's central area exhibited lower cell density and, consequently, reduced oxygen demand, attributable to the outward mechanical stretching from the rapidly expanding periphery. Figure 4-5(d) illustrates the more substantial growth in peripheral tissue compared to the center, resulting in a gradient of cell density across the tumor, as detailed in Figure 4-5(e). Other property maps are also illustrated in Figure 4-5,

including the hypoxia map, the vessel surface density map that reflects the vessel oxygen source density, and the proliferation activity map.

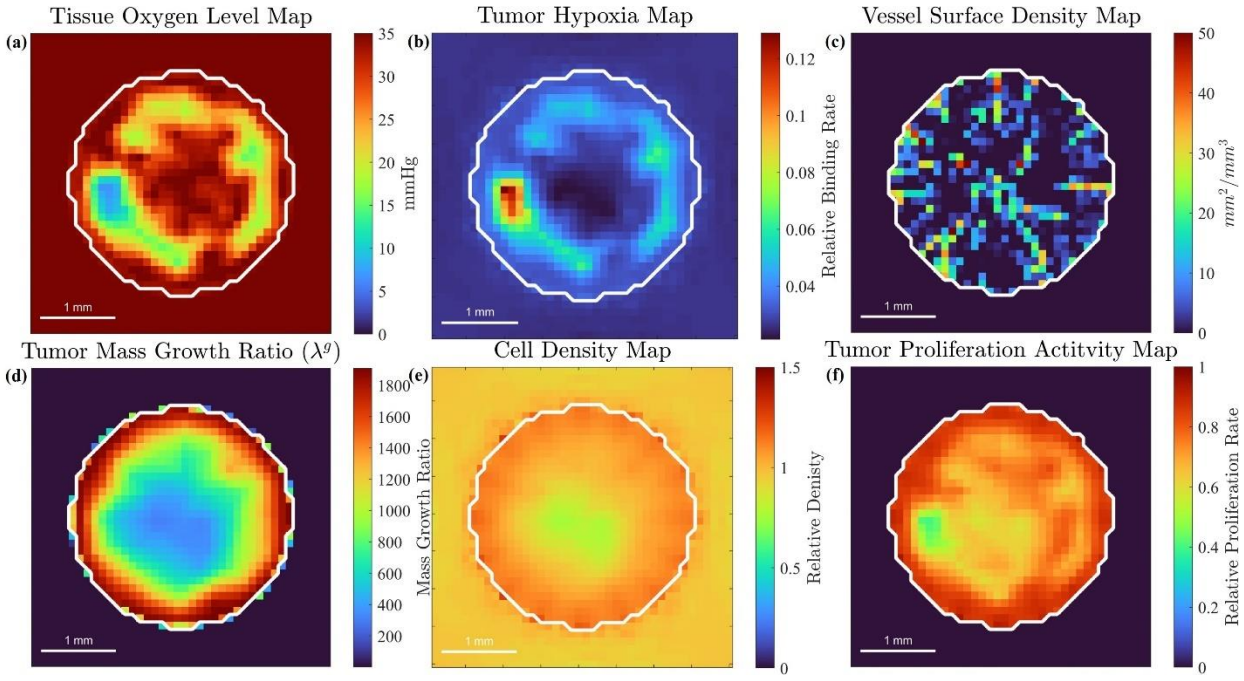

Figure 4-5 Central slice of the tumor property maps. The maps illustrate the tissue oxygen level, binding rate with hypoxia tracer FMISO, vessel surface density, mass growth ratio, relative cell density, and volumetric tumor proliferation activity respectively.

The entire vasculature structure and the vessel radius distribution are shown in Figure 4-6. Figure 4-6(a) highlights the tumor vasculature's intricate topology and the diverse vessel sizes, showcasing the complexity and heterogeneity of the system. In Figure 4-6(b), a detailed view of both the surface environmental vasculature and the internal tumor vasculature is provided. Notably, large vascular shunts can be observed connecting the environmental vessels, creating a

high flow rate shortcut connection. Which is widely observed in tumor vasculature and could harm the perfusion extending toward the tumor inside[161]. The internal network is characterized by its complex interconnections and tortuous pathways, including numerous blind ends. The measured vessel tortuosity is 1.152, which matches with the observed GL261 glioma vasculature tortuosity of 1.151[97]. The wide-ranging vessel radius distribution, spanning from 2 to 20 μm, is depicted in the vessel radius histogram in Figure 4-6(c), highlighting the heterogeneity within the vasculature. This distribution, resembling a normal curve, reflects the naturally emerging pattern from the large-scale, interconnected network of perfused vasculature. The mean vessel radius is 6.5 μm, which falls between the literature-reported GL261 vessel mean radius ranging from 5[162] to 11[97] μm. Figure 4-6(d) illustrates the correlation between vessel radius and flow, aligning closely with the expected curve from the radius remodeling formula, indicating a successful vessel remodeling process for this extremely complex and inter-affected vascular system.

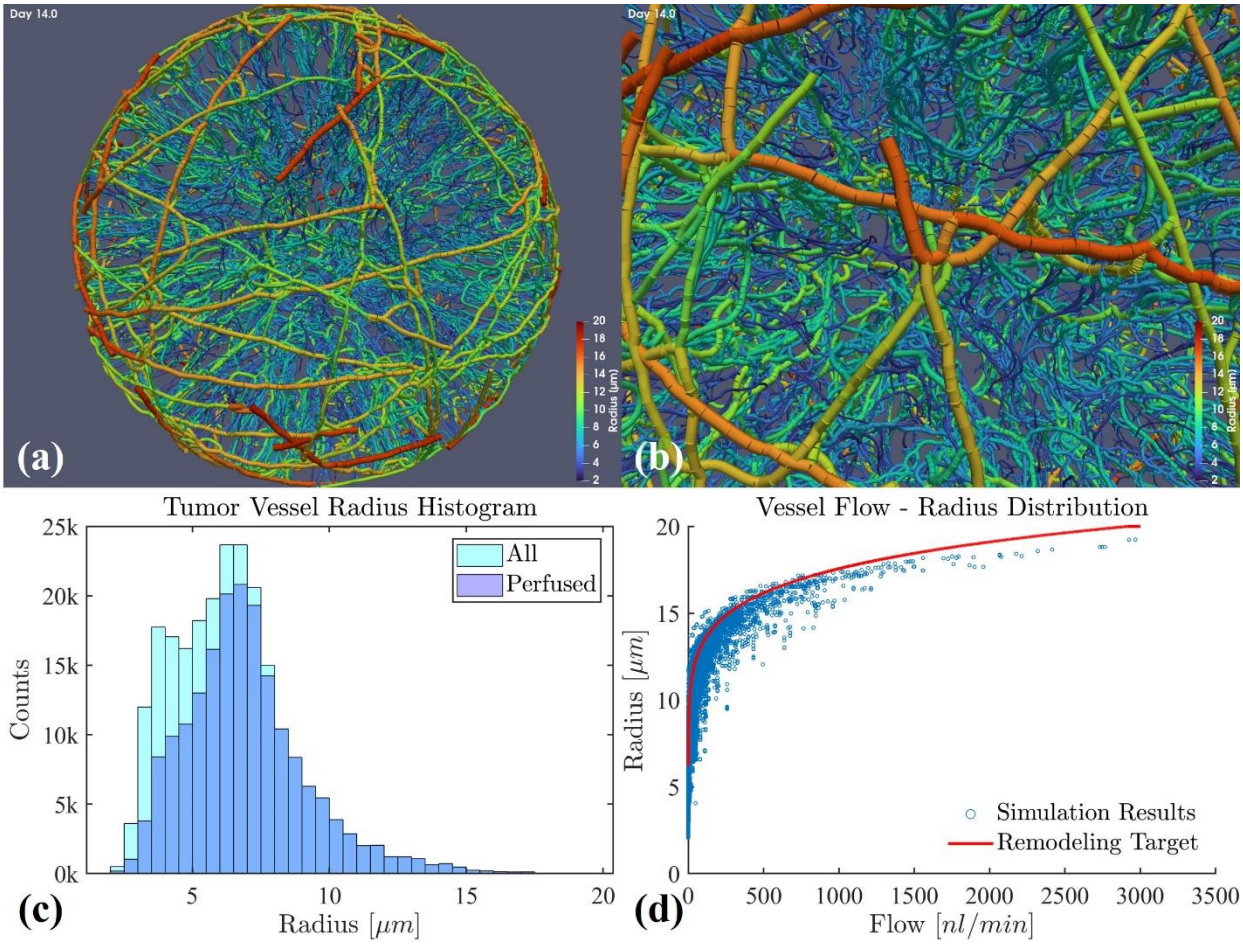

Figure 4-6 Vasculature Morphology and radius distribution. (a) Tumor vasculature, color indicating the vessel radius. (b) A focused view of the vasculature, highlighting shunt formations on the surface and internal chaotic and tortuous network with a significant number of blind ends. (c) Histogram for the vessel radius. (d) Scatter plot of vessel flow-radius distribution. The red line indicating the optimal radius under given flow conditions, given by the vessel radius remodeling formula.

Figure 4-7(a) presents the spatial blood pressure distribution across the entire vasculature and its corresponding histogram. Notably, a low-frequency spatial variation in blood pressure is

observed, with a pressure gradient across downstream tumor vessels emanating from environmental vessels, promoting effective tumor perfusion. The discharged hematocrit distribution exhibits considerable heterogeneity, with a significant portion of vessels showing low discharge hematocrit levels (Hd), typically corresponding to hypo-perfused vessels with small radii. This suggests that a substantial part of the vasculature may be incapable of fulfilling its role in oxygen transport, underscoring the importance of excluding certain vessels from considerations of tissue oxygen supply.

Figure 4-7(c) displays the spatial distribution of blood flow rate and the histogram of blood flow distribution using a logarithmic scale for flow rates. The outer environmental vessels have a higher flow rate compared to the tumor internal vasculature and the overall flow distribution is highly heterogeneous. The histogram reveals a noticeable second bump in the low-flow range, attributed to the numerical errors from the linear solver. However, these anomalously low flows are minimal and do not impact the vasculature's functional properties especially for the functional part of the vasculature. When vessels with zero discharge hematocrit are excluded, the adjusted histogram exhibits a near-normal distribution on the logarithmic flow rate scale. Similar small value numerical artifacts are also observed in the logarithmic histogram for wall shear stress shown in Figure 4-7(d). The anomaly, characterized by a second bump, vanishes when vessels not perfused are omitted from the analysis. Despite this adjustment, the wall shear stress in perfused vessels continues to show a broad distribution and significant spatial heterogeneity. This phenomenon is consistent with findings from blood perfusion studies in actual tumor vasculatures, which demonstrate pronounced heterogeneity in wall shear stress (WSS) despite

efforts to optimize blood pressure at the boundaries and achieve a uniform distribution of WSS along the vasculature walls.

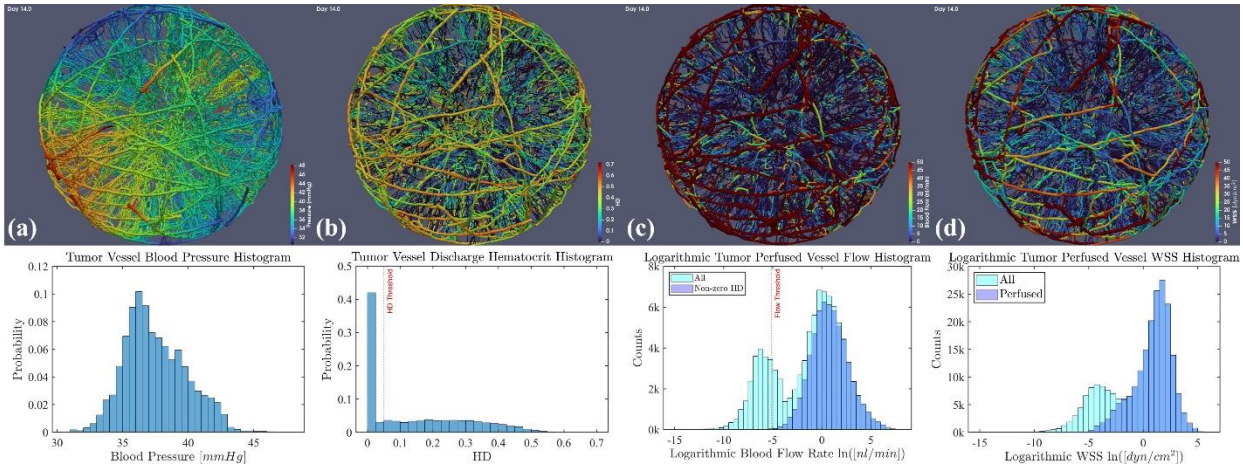

Figure 4-7 Key functional characteristics of tumor vasculature: (a) Histogram of blood pressure distribution in the vasculature. (b) Histogram of vessel discharge hematocrit distribution, with the red dotted line marking the oxygen supply threshold hematocrit at 0.05. (c) Logarithmic histogram of blood flow rates within the tumor vasculature, where the dotted line represents the oxygen supply flow rate threshold at 100 um³/s. Vessels with zero hematocrit are excluded from the dark blue histogram. (d) Logarithmic histogram of wall shear stress across the tumor vasculature. The dark blue histogram excluded unperfused vessels.

	Simulation	**Unit**	**Reference**
Maximum Cell Proliferation Rate	1	Day^{-1}	
Oxygen Consumption Rate	3	mmHg/s	
Growth Time	14	day	

Tumor Volume	13.08	mm^3	
Daily Growth Ratio	62.88	%	13%-63%[143]
Relative Cell Density	1.05 ± 0.09		
Tissue Oxygen	27.68 ± 6.67	mmHg	15-55[126]
Tissue Perfusion	24.22 ± 108.52	ml/g/min	
Vessel Radius	6.46 ± 2.30	µm	5[97] - 11[162]
Vessel Length Density (perfused / total)	79.83 / 136.69	mm/mm^3	76.2[162] - 213[97]
Vessel Surface Density (perfused / total)	4.07 / 5.77	mm^2/mm^3	5.7[162] -7.5[97]
Vessel Volume Density (perfused / total)	1.79 / 2.23	%	1.9[97] – 4.8[162]
Blood Flow Rate	10.58 ± 59.33	nl/min	16.2[162]
Blood Flow Velocity	0.44 ± 1.34	mm/s	0.44[162]
Wall Shear Stress	5.56 ± 11.68	dyn/cm^2	17.8[162]
Vessel Tortuosity	1.152		1.151[162]
Branching Length	45.49 ± 55.44	µm	18[97] - 99.7[162]
Bifurcation Density	1796.87	mm^{-3}	584[162] -10000[97]

Table 4-4 Quantitative summary of the simulated tumor.

4.3.2 Tumors with Varied Spouting Rate

Tumor vasculature is a crucial target in cancer therapy, with interventions taking two divergent approaches. Vascular disrupting therapy[163] focuses on destroying the tumor's vasculature to directly damage the tumor itself. Conversely, tumor vasculature normalization[164] aims to improve angiogenesis, thereby enhancing tumor oxygenation, perfusion, and ultimately, the efficacy of treatments.

To explore how different angiogenesis rates affect tumor growth, we conducted simulations on two samples, altering only the sprouting rate from the baseline tumor model. One sample had its sprouting rate reduced by 50%, while the other had a 50% increase. The resulting vasculatures from these simulations are depicted in Figures 4-8, and the growth curves of three tumors, as well as the tissue oxygen distribution, are shown in Figures 4-9.

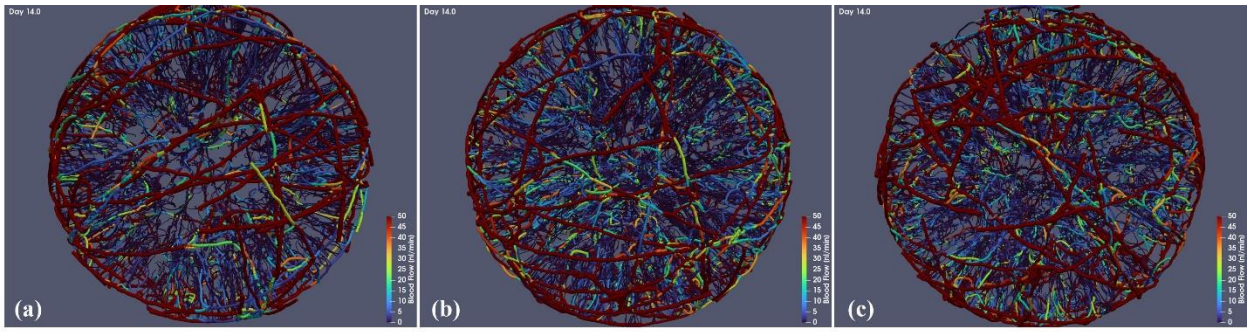

Figure 4-8 Tumor vasculature with varied angiogenesis. (a) sprouting suppressed. (b) Baseline tumor. (c) sprouting enhanced.

The simulation of the angiogenesis-suppressed tumor revealed a sparser vasculature and a central avascular necrotic core. In contrast, the tumor with enhanced angiogenesis showed minimal morphological differences from the baseline model. Growth rates and vascular volume densities for these tumors are charted in Figure 4-9(a), with the enhanced tumor exhibiting the fastest growth and the suppressed tumor the slowest. The vascular volume density curves for the baseline and enhanced tumors demonstrate a swift increase in vascularization, followed by a stable plateau, while the suppressed tumor's vasculature remains underdeveloped, as indicated by a consistent densification trend until the simulation's conclusion.

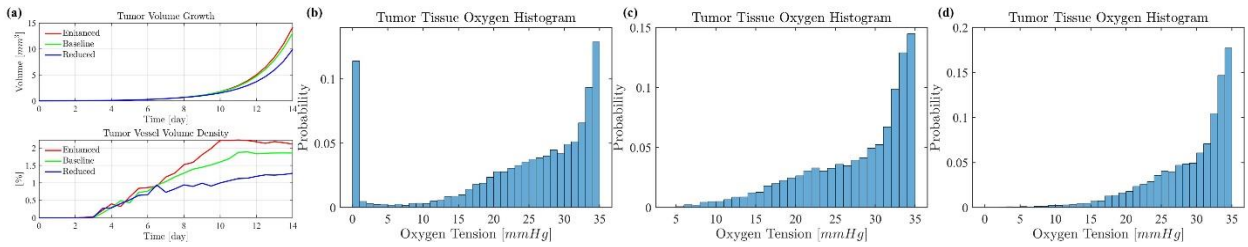

Figure 4-9 Growth curve of tumor vasculature and tissue oxygen histogram. (a): the growth curve of the tumor volume and tumor vascular volume density. (b), (c), and (d): Tissue oxygen level histogram of tumor suppressed, baseline, and enhanced sprouting rate, respectively.

The oxygenation histograms in Figures 4-9(c) and (d) display comparable distributions for the baseline and enhanced tumors. However, the suppressed tumor presents extensive low-oxygen necrosis. Table 4-5 enumerates key characteristics of the tumor tissues and vasculature for the three tumor types. There is a discernible positive correlation between angiogenic rate and parameters such as tissue oxygen level, oxygen homogeneity, vessel density, and blood perfusion. The disparity between the suppressed tumor and the baseline tumor is substantial, whereas the difference between the baseline and the enhanced tumor is subtle. suggesting that angiogenic capability (relative to tissue growth rate) may reach a saturation point due to self-regulating mechanisms like TAF concentration-dependent sprouting rates. Thus, tumors with inherently poor vascularization might experience more pronounced effects from angiogenic modulation, while for normally growing healthy tissue, the effect on angiogenesis can be minor.

		Suppressed	**Baseline**	**Enhanced**
Tumor Growth	**Sprouting Scaling**	0.5	1.0	1.5

	Growth Time [day]	14	14	14
	Tumor Volume [mm^3]	9.91	13.08	14.22
	Necrosis Volume [mm^3]	1.430	0.000	0.006
	Daily Growth [%]	59.7	62.9	63.9
Tissue Characteristics	**Cell density**	0.868 ± 0.396	1.050 ± 0.090	1.044 ± 0.116
	Tissue Oxygen [mmHg]	24.0 ± 10.9	27.7 ± 6.7	29.1 ± 5.8
	Vas Vol Density [%]	1.6 ± 3.7	2.2 ± 4.5	2.4 ± 5.3
	Tissue Perfusion [ml/g/min]	22.8 ± 107.0	24.2 ± 108.5	34.4 ± 142.5
Vasculature Characteristics	**Perfused/Total Length Density [mm/mm^3]**	49.3 / 105.6	79.8 / 136.7	81.4 / 131.2
	Perfused/Total Surface Density [mm^2/mm^3]	2.6 / 4.2	4.1 / 5.8	4.4 / 5.8
	Perfused/Total Volume Density [%]	1.3 / 1.6	1.8 / 2.2	2.0 / 2.4
	Blood Flow [nl/min]	15.4 ± 85.9	10.6 ± 59.3	15.7 ± 71.8
	Blood Flow Velocity [mm/s]	0.58 ± 1.89	0.44 ± 1.34	0.60 ± 1.62
	WSS [dyn/cm^2]	7.0 ± 16.0	5.6 ± 11.7	7.1 ± 13.5
	Branching Length [µm]	69.0 ± 76.9	45.5 ± 55.4	38.2 ± 49.2
	Bifurcation Density [mm^{-3}]	860	1797	2103

Table 4-5 Summary of tumor samples with suppressed, baseline, and enhanced angiogenesis sprouting.

4.3.3 Tumors with Varied Metabolism and Proliferation

To assess the effects of tumor growth rate and oxygen demand on development, we performed simulations with a range of parameters for 9 fast-growing and 3 slow-growing tumor samples, analyzed when the tumor volume reached approximately 12 mm^3. The baseline proliferation rate corresponds to a 24-hour cell doubling time, with the maximum proliferation rate scaling for the fast-growing-tumor of 1.2, equating to a 20-hour doubling time, aligned with GL261 cell proliferation rates observed in vitro[140]. Proliferation rates exceeding this may be considered unrealistic. The lowest scaling at 0.5 results in a daily growth ratio of 30%, comparable to low-proliferation murine GL261 tumors observed in vivo[143], where the overall daily growth ratio for tumors from below 1 mm^3 to around 15 mm^3 ranges from 24% to 49%. For fast-growing tumors, the oxygen consumption rate (OCR) ranges from 2 to 4 mmHg/s, in line with OCRs measured in high-grade gliomas (2.2 mmHg/s) and glioblastomas (3.7 mmHg/s)[123]. Slow-growing tumors have OCRs from 2 to 10 mmHg/s, with the higher rates approximating the oxygen demand of normal brain tissue, offering insights into healthy tissue vascularization. Figure 4-10 showcases the parameter selection alongside tumor property maps, including cell density, vasculature volume fraction, and tissue oxygen levels for each sample. Quantitative summaries of these tumors are provided in Table 4-6 and 4-7.

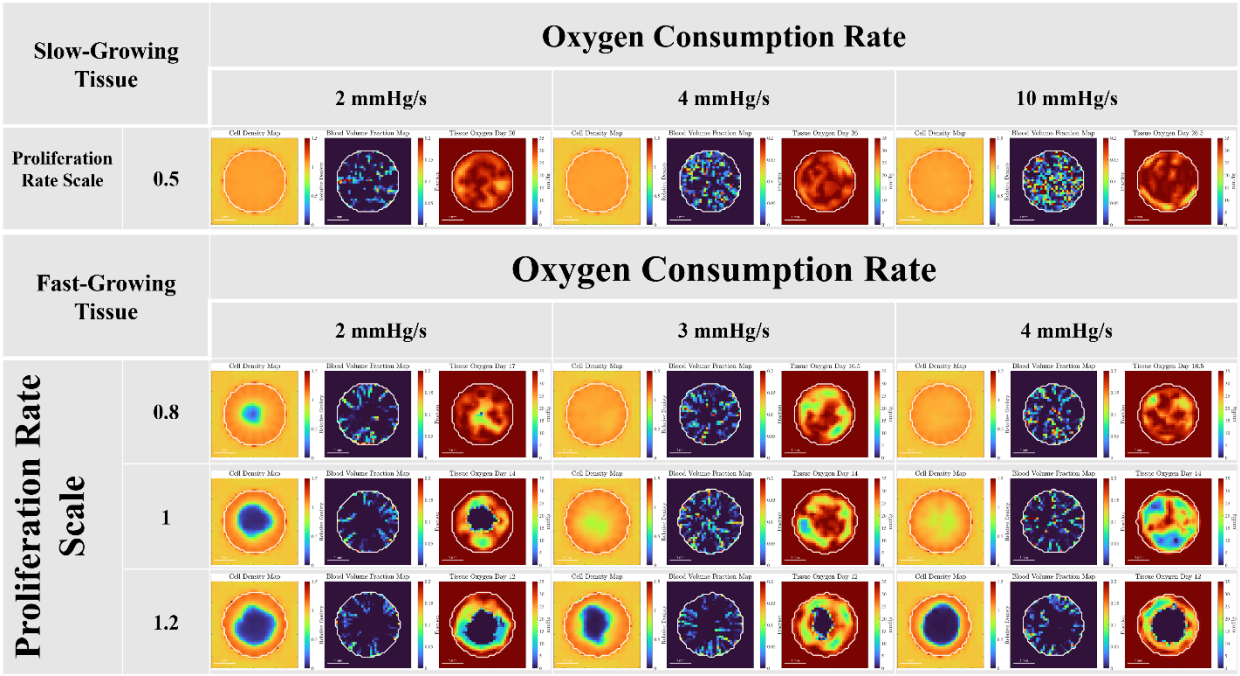

Figure 4-10 Parameter Selection and Simulation Results for Tumor Samples at a Volume of Approximately 12 mm³. Slow-growing tumors, characterized by a maximum cell proliferation time scaling of 0.5 (equivalent to a 48-hour cell doubling time), were simulated with oxygen consumption rates (OCR) of 2, 4, and 10 mmHg/s. For fast-growing tumors, with proliferation rate scaling of 0.8, 1, and 1.2, three samples were generated for each scaling level with OCRs of 2, 3, and 4 mmHg/s. Each sample's cell density map, vessel volume fraction map, and tissue oxygen level map are displayed, providing insights into the varied tumor behaviors.

In our simulations, the predominant factor influencing effective tumor growth rates was cell proliferation, with tumor oxygen consumption rate (OCR) also playing a role; higher OCRs tended to marginally reduce tumor growth rates.

Fast proliferating tumors were characterized by cell density heterogeneity and necrosis, distinguishing them as hallmarks of aggressive growth. Conversely, slow-growing tumors

exhibited high homogeneity and lacked necrosis, regardless of OCR. Fast-growing tumors displayed significantly higher cell density standard deviations, indicating greater heterogeneity even in the absence of necrosis.

The growth rate inversely affected mean tissue oxygen levels, increasing oxygen heterogeneity. However, OCR's impact on oxygen levels and heterogeneity was less pronounced, likely due to angiogenesis' self-regulatory mechanisms.

Central necrosis was primarily triggered by high initial growth rates. In samples with moderate proliferation rates (scaled by 0.8 and 1.0), those with lower oxygen demand developed necrosis, whereas those with higher demand did not, attributed to the marginally higher effective proliferation rates in low OCR samples. This mirrors in vivo observations, where high-grade glioblastomas (GBMs) with rapid proliferation and lower oxygen demand are more prone to necrosis than low-grade GBMs. In samples with a 1.2 proliferation rate, necrosis occurred irrespective of OCR. The extent of necrosis correlated with both growth rate and OCR, with high OCR contributing to a steeper oxygen gradient and a thinner viable tissue rim.

Vascularization was primarily influenced by OCR, with high-demand tumors recruiting more vessels to balance angiogenesis and growth, facilitated by tumor angiogenic factors (TAF) release. Vasculature density-related metrics, such as vessel density and bifurcation density, were almost directly proportional to OCR. Average functional aspects of the vasculature, such as mean blood flow rate, vessel radius, and bifurcation length, saw only slight increases in high-demand tumors, indicating a nuanced impact of OCR on these aspects.

Sample Parameters		Tumor Growth			Tissue			
Pro-Scale	**OCR [mmHg/s]**	**Tumor volume [mm^3]**	**Daily Growth [%]**	**Necrosis Volume [mm^3]**	**Cell density**	**Tissue Oxygen [mmHg]**	**Vas Vol Density [%]**	**Tissue Perfusion [ml/g/min]**
0.5	**2**	12.34	29.8	0	1.066±0.011	30.94±3.45	1.5±3.4	14.8±61.4
	4	11.93	29.6	0	1.066±0.011	32.27±2.79	3.5±6.0	42.5±134.8
	10	11.93	28.9	0	1.066±0.018	30.97±4.28	7.2±10.3	70.1±168.2
0.8	**2**	12.02	48.7	0.008	1.036±0.147	31.0±4.7	1.9±8.8	23.5±102.7
	3	11.64	50.2	0	1.065±0.024	29.3±5.2	2.2±4.4	20.5±81.5
	4	11.05	49.7	0	1.065±0.028	29.1±4.8	2.8±5.2	28.7±97.6
1	**2**	12.38	62.2	0.889	0.950±0.308	27.2±9.0	1.8±4.1	25.0±123.3
	3	13.08	62.9	0	1.050±0.089	27.7±6.7	2.2±4.5	24.2±108.5
	4	12.67	62.5	0.003	1.054±0.079	25.2±7.7	2.5±5.3	29.8±111.7
1.2	**2**	13.30	77.0	2.104	0.874±0.386	21.7±11.7	1.3±3.4	19.2±101.5
	3	13.04	76.6	1.318	0.908±0.356	24.9±9.5	1.7±4.1	22.4±118.2
	4	11.64	75.0	2.265	0.813±0.443	21.8±11.5	2.0±4.7	22.7±102.8

Table 4-6 Growth and tissue-related characteristics of 12 tumor samples.

Sample Parameters	Vasculature Characteristics

Pro-Scale	OCR [mmHg/s]	Radius [μm]	Perfused/Total Len Density [mm/mm^3]	Blood Flow [nl/min]	Branching Length [μm]	Bifurcation Density [mm^{-3}]
0.5	2	6.13±2.76	48.1/83.8	8.7±39.8	55.8±64.7	880
	4	6.77±2.55	125.1/195.5	12.7±56.8	50.0±63.4	2407
	10	7.41±2.33	268.6/353.1	12.1±57.0	37.4±45.2	5939
0.8	2	6.02±2.71	65.1/119.9	12.0±60.6	61.8±79.22	1155
	3	6.27±2.45	80.1/133.5	8.8±44.8	48.7±60.4	1648
	4	6.58±2.36	104.6/162.6	10.0±47.3	44.9±54.1	2193
1	2	6.09±2.46	59.1/117.0	13.2±70.0	48.4±57.8	1444
	3	6.46±2.30	79.8/136.7	10.58±59.3	45.5±55.4	1797
	4	6.66±2.44	91.0±148.0	12.3±57.0	38.2±47.7	2357
1.2	2	5.97±2.40	42.8±93.6	13.7±74.3	48.9±56.2	1116
	3	6.40±2.35	61.0±107.4	13.6±68.1	45.2±52.7	1401
	4	6.72±2.29	70.5±115.6	13.9±65.8	40.6±47.0	1699

Table 4-7 Vasculature-related characteristics of 12 tumor samples

4.3.4 Radiomics Analysis of Random Tumor Samples

While the table of semantic tumor characteristics allows us to discern differences among various types of tumors based on differentiation parameters, such handcrafted analysis captures only a fraction of the patterns that emerge during tumor development. An intriguing question arises: might agnostic features that characterize heterogeneities more effectively encapsulate the differences in tumor biophysical parameters? Conversely, could our mechanistic models, grounded in understanding, bridge the gap with radiomics analysis, providing robust, causality-based insights into key biophysical properties?

To explore these possibilities, we generated 20 random examples with proliferation rate scaling from 0.8 to 1.2 and oxygen consumption rates from 2 to 4 mmHg/s. The randomly generated parameter sets are shown in Figure 4-11. For each sample, we generated a set of 3941 features, comprising 21 semantic features characterizing vasculature morphology and function and 3920 predefined agnostic features extracted from tumor maps using PyRadiomics[165] mainly characterizing tumor heterogeneities. These agnostic features include 14 tumor shape features and 558 quantitative features for each of the seven tumor maps. These maps include relative cell density, oxygen partial pressure, cell oxygen metabolism rate, hypoxia tracer binding rate, vascular volume fraction, blood perfusion, and proliferation activity map. The extensive feature set for each map encompasses various features in quantitative analyses—first-order statistics, gray level co-occurrence matrix (GLCM), gray level dependence matrix (GLDM), gray level run length matrix (GLRLM), gray level size zone matrix (GLSZM), and neighboring gray-tone difference matrix (NGTDM)—enhanced by different filters.

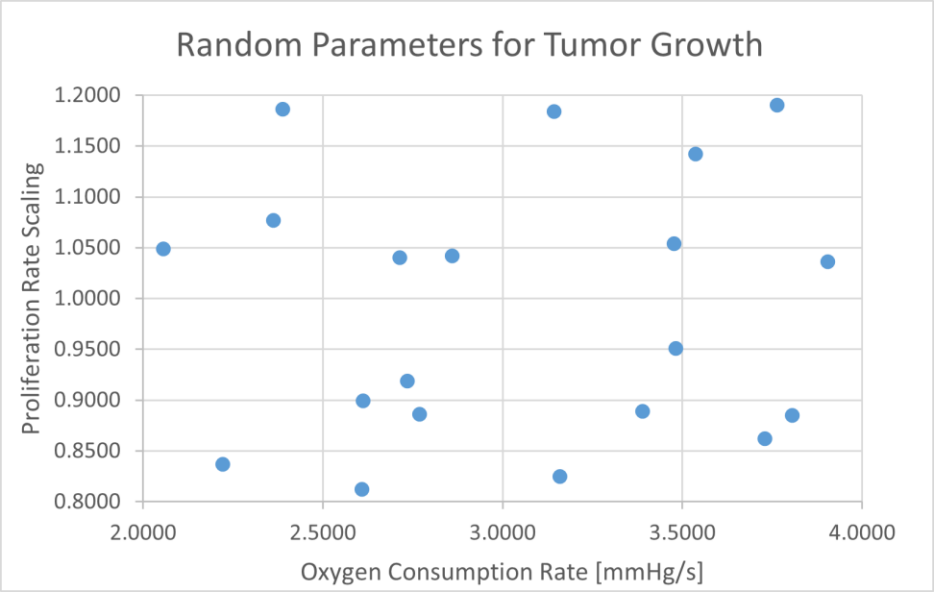

Figure 4-11 Random proliferation rate and oxygen metabolism rate parameters for a total of 20 tumor samples.

4.3.4.1 Correlation Coefficients of Features

To evaluate the correlation between features and key tumor properties, namely the tumor proliferation rate (PR) and oxygen consumption rate (OCR), we calculated their corresponding correlation coefficients. Features with absolute correlation coefficients exceeding 0.5 are called strongly correlated with the biological properties of interest. Given the relatively small sample size and the large number of features, there's a potential risk of identifying spurious correlations. To assess the severity of this issue, we conducted one hundred repeated correlation coefficient assessments between randomly generated tumor properties and extracted tumor features, analyzing the feature statistics.

The statistics of the correlation coefficients are listed in Table 4-8.

Features From	Extracted Features	Strongly Correlated Features For PR	Strongly Correlated Features For OCR	Random Assigned Property
Vasculature Properties	21	11	13	0.32 ± 0.72
Tumor Shape	14	1	0	0.32 ± 1.18
Tissue Oxygen Level Map	558	345	10	9.5 ± 25.12
Relative Cell Density Map	558	97	2	5.21 ± 16.38
Relative Oxygen Metabolism Map	558	392	3	6.57 ± 24.41
Hypoxia Map	558	346	30	8.01 ± 18.31
Blood Volume Map	558	322	71	6.32 ± 13.65
Blood Perfusion Map	558	217	85	7.75 ± 16.22

Relative Proliferation Activity Map	558	383	17	7.40 ± 24.71
Total	3941	2110	231	51.4

Table 4-8 Number of features extracted and the number of strongly correlated features.

In our analysis, significantly more features exhibit strong correlations with cell proliferation rate (PR) than with oxygen consumption rate (OCR). Particularly, features derived from maps characterizing tissue oxygen level and hypoxia, relative oxygen metabolism, and relative proliferation intensity show stronger correlations with PR. Conversely, features from maps of blood volume and perfusion are more strongly correlated with OCR.

For both PR and OCR prediction tasks, the number of features with strong correlations far exceeds those identified with randomly generated properties. This suggests that only a small fraction of strong features are potentially spurious correlations and that real tumor biophysical information is indeed reflected in the majority of these strong features.

The distribution of correlation coefficients between features and real tumor properties versus random properties presents significant differences, as depicted in Figure 4-12. The histogram of feature correlation coefficient with proliferation rate (PR) reveals a substantial number of features with very high correlation coefficients, many of which exceed 0.9. In contrast, the majority of features show only a weak correlation with oxygen consumption rate (OCR). For random properties, the distribution of correlation coefficients is centered around zero, with only a very small fraction of features falling into the strong correlation range, and none exceeding 0.7.

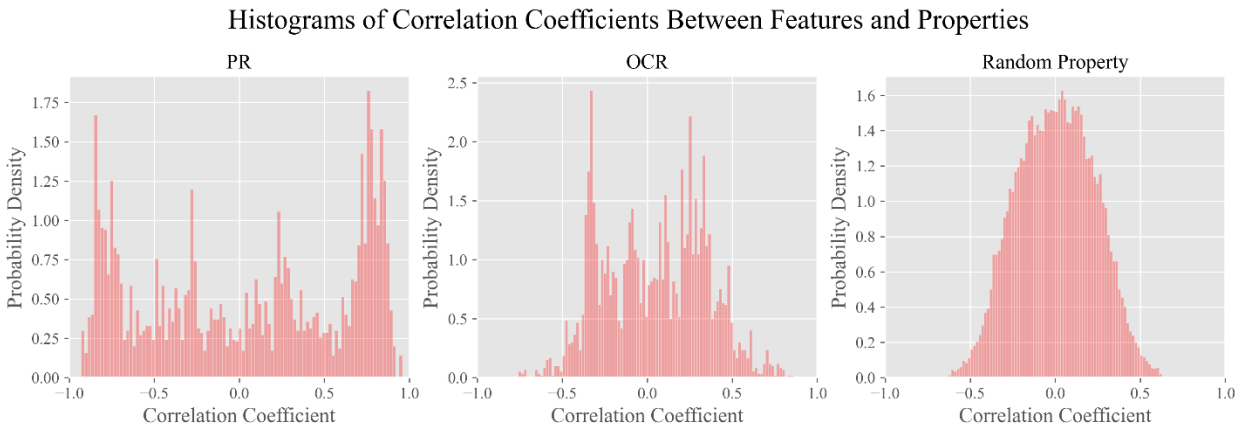

Figure 4-12 Correlation coefficients between features and tumor properties. Left: with tumor proliferation rates; Middle: with oxygen consumption rates; Right: with randomly assigned numbers.

4.3.4.2 Lasso Prediction of Biophysical Properties

Lasso regression was utilized to construct predictive models for two biophysical parameters—proliferation rate (PR) and oxygen consumption rate (OCR), with the absolute values of the coefficients indicating feature importance. Features are normalized before training and leave-one-out cross-validation is employed to enhance model robustness and alleviate the dimensionality issue. Predictive accuracy is depicted in Figures 4-14 and 4-15 for PR and OCR, respectively, with the model demonstrating respectable precision for both. The relative root mean squared error (RRMSE) for PR prediction is 4.6% and that for OCR prediction is 10.4%. For

reference, for the given value range, the prediction simply gives the mean value of all samples, resulting in an RRMSE of 11.5% for PR and 19.3% for OCR; the prediction gives a random value within the data range will result in a RRMSE of 16.3% for PR and 27.2 for OCR.

The feature deemed most important by the model is highlighted in the accompanying plot.

Figure 4-13 Lasso prediction of sample proliferation rate and the top features involved in the prediction.

For PR prediction, the top features are the 90th percentile value of the original cell density map, the Informational Measure of Correlation (IMC) 2 of the Gray Level Co-occurrence Matrix (GLCM) calculated from the high-pass wavelet-filtered cell density map, and the complexity of the Neighbouring Gray Tone Difference Matrix (NGTDM) calculated from the high-pass wavelet-filtered hypoxic map.

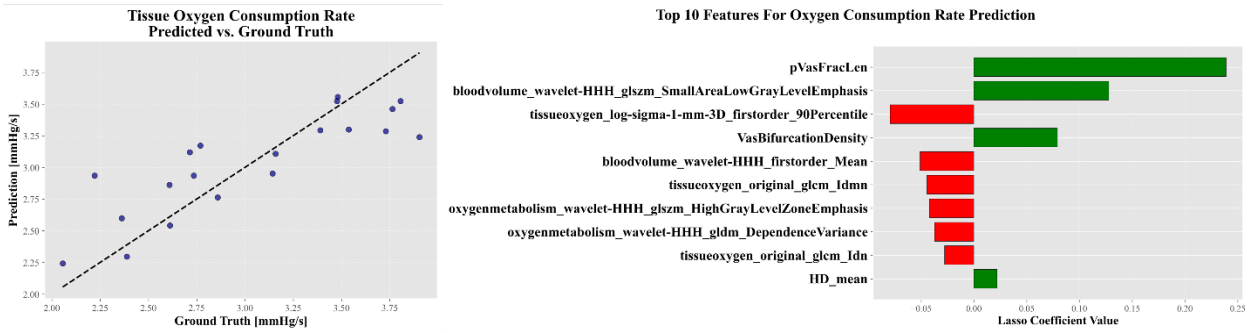

Figure 4-14 Lasso prediction of sample oxygen consumption rate and the top features involved in the prediction.

In OCR prediction, the features are the perfused vessel length fraction, the small-area low gray-level emphasis of the Gray Level Size Zone Matrix (GLSZM) calculated from a high-pass wavelet-filtered blood volume map, the 90th percentile value of the Laplacian of a Gaussian-filtered tissue oxygen map, and the vessel bifurcation density.

4.3.4.3 Lasso Prediction with Specific Property Map

To access the information contained in different tumor maps as well as the effect of image resolution on prediction performances, we perform LASSO prediction based solely on feature extraction from specific property maps at various resolutions.

RRMSE of LASSO Prediction with Partial Features (%)

Prediction For	PR			OCR		
Resolution [µm]	**50**	**100**	**150**	**50**	**100**	**150**
Vasculature Properties	5.76	6.84	7.32	6.91	7.33	6.84
Tumor Shape	11.01	10.36	13.71	25.22	20.18	21.83
Tissue Oxygen Level Map	4.35	6.82	5.60	13.51	14.31	22.48
Relative Cell Density Map	4.46	4.65	4.07	23.37	21.51	19.65
Relative Oxygen Metabolism Map	4.48	5.01	4.15	18.00	23.35	27.61
Hypoxia Map	5.68	6.60	5.99	22.24	30.45	21.23
Blood Volume Map	4.83	4.51	10.59	16.73	14.14	16.26
Blood Perfusion Map	6.70	8.06	7.91	23.38	27.33	27.39
Relative Proliferation Activity Map	5.62	4.67	4.77	16.04	11.91	22.69
All	5.14	4.59	5.01	9.41	10.36	10.98

Table 4-9 LASSO prediction results with only features extracted from specific property maps.

In general, PR is better reflected in various property maps and inherently has a more noticeable effect on tumor patterning than OCR. High resolution is strongly preferred for OCR prediction, but for PR, no obvious resolution preference is observed within the studied resolution range.

4.4 Discussion

4.4.1 Model Validation

In this study, we meticulously calibrate our model by aligning microscopic biophysical parameters with the available literature, utilizing in vivo measurements from GL261 glioma mouse models or, when such data are unavailable, analogous human GBM studies. We focus on several key aspects, including the Poisson's ratio and shear stress for continuum mechanics of host and tumor brain tissues; cell proliferation rate and its oxygen dependence for tumor growth; in vivo viscosity of mouse blood and the phase separation effect for red blood cell distribution; tissue oxygen demand and vessel oxygen mass transfer coefficient for oxygenation; and tip cell migration speed, anastomosis sensing range, and reference wall shear stress for vascular remodeling.

For macroscopic tumor features, we selectively calibrate only crucial aspects against available data, allowing other features to naturally emerge from the defined microscopic parameters while

ensuring they remain within a reasonable physiological range. Such rigidly calibrated macroscopic characteristics include effective tumor growth rate, perfused vessel surface area, and vessel tortuosity, which cover essential aspects of tumor growth, vascularization, oxygenation, and vessel morphology.

Given the variability and limitations of the available calibration data, which often come from different studies or tumor samples, and the sometimes-necessary use of human GBM data or empirical formulas from normal mice tissue, we do not rigidly fit every feature to data. For example, the mean vessel radius. while GL261 vasculature data[97] indicates a mean vessel radius of about 11 μm from imaging with a coarse resolution of 5-8 μm—potentially missing many smaller vessels and overestimating the mean radius—other studies report a mean radius of 5 μm[162] from smaller GL261 tumors, which might lack larger, highly perfused vessels. In our model, we recognize that neither set of available data provides a reliable ground truth for our specific scale and resolution. Therefore, we opt not to calibrate the vessel radius against these measurements. Instead, we allow the vessel radius to be remodeled based on empirical wall shear stress principles. Consequently, the simulated vessel radius naturally falls between the two reported values, reflecting a more balanced and empirically grounded approach.

By adopting this approach, we ensure that our model reflects a reasonable range of tumor properties and maintains its scientific integrity without being constrained by the heterogeneity and quality issues inherent in tumor data. This strategy allows us to focus more on the qualitative relationships between macroscopic features and underlying microscopic biological changes, which are crucial for interpreting the complex dynamics of tumor growth and vascular development.

4.4.2 Result Interpretation

4.4.2.1 Baseline Tumor

Using calibrated microscopic parameters sourced from literature and actual tumor data, we simulated tumor development under constraints such as mechanical deformation, blood perfusion dictated by vessel structure, and nutrient supply regulated by oxygen transport. This methodology enabled the tumor to evolve naturally, exhibiting significant heterogeneities while retaining macroscopic characteristics within the physiological norms for tumor properties.

In our baseline simulation, we achieved groundbreaking modeling of tumor growth on a multi-millimeter scale, with vasculatures that are morphologically and functionally sound. The tumor expanded about one thousand-fold, reaching a volume of approximately twelve cubic millimeters, closely mirroring the daily growth rate observed in vivo. The vasculature displayed an unbiased and extensively interconnected network, with tortuosity, radius, and density that align closely with real GL261 tumor vasculature data.

Moreover, the vasculature properties demonstrated notable naturally emergent heterogeneities. Histograms of vessel radius, blood pressure, logarithmic blood flow rate, and logarithmic wall shear stress (WSS) exhibited near-normal distributions. Such distribution patterns may indicate

the characteristics of a well-functioning, self-regulated vasculature system. Additionally, we noted a decrease in histogram skewness with increased vessel connectivity, suggesting that this metric might provide a potential indicator of the functional wellness of the vasculature system.

We generate several property maps for the analysis of tissue heterogeneities. The property maps identified for analysis have the potential to be non-invasively imaged in vivo. For instance, cell density might be inferred from ADC MRI, which provides information on the extracellular fluid fraction, or from CT scans that reflect atomic composition. Tissue blood perfusion and volume could be captured using various imaging modalities with contrast agents, while extracellular oxygen levels might be gauged through Electron Paramagnetic Resonance (EPR)[158] imaging. Tissue hypoxia could be visualized using 18F-Fluoromisonidazole (FMISO) PET[159], oxygen metabolism through Oxygen 17 MRI[123], and proliferation rates through [18F]-FLT-PET[160]. However, these imaging technologies face challenges, including limited signal-to-noise ratios, coarse resolution, and complex contrast mechanisms that can obscure the direct measurement of the properties of interest. In this study, we bypass the constraints of specific imaging modalities and their contrast mechanisms by directly analyzing ground truth properties. This approach allows us to focus on identifying the most informative properties for investigation, rather than being limited by the capabilities of existing imaging technologies.

4.4.2.2 Sprouting Rate Modulation

In our study comparing tumors with suppressed and enhanced angiogenic sprouting, we found that increased sprouting rates improved tissue oxygen levels, oxygen homogeneity, vessel density, and blood perfusion. Conversely, significant necrosis was observed in tumors with suppressed angiogenesis, aligning with expectations for vasculature regulation therapies. Notably, there was a marked disparity between the suppressed tumor and the baseline tumor, while the difference between the baseline and the enhanced tumor was more subtle. The vessel density over time showed that both the baseline and enhanced tumors experienced a rapid vascularization phase, with the enhanced tumor displaying a steeper slope before both reached a similar plateau in vessel density. In contrast, the suppressed tumor continued to densify its vessel network throughout the simulation, indicating an insufficient rate of new vessel formation.

These findings suggest that angiogenic capability, relative to tissue growth rate, may reach a saturation point due to self-regulating mechanisms such as TAF concentration-dependent sprouting rates. Consequently, tumors with inherently poor vascularization may exhibit more pronounced responses to angiogenic modulation. However, in slowly growing, well-vascularized tissues like benign tumors or healthy tissue, the effects of moderate angiogenic modulation—either upregulation or downregulation—can be minimal. Understanding these dynamics can enhance our comprehension of vascular disrupting treatments and tumor vasculature normalization therapies, helping to identify scenarios where these treatments are most advantageous.

4.4.2.3 Role of Cell Proliferation Rate and Oxygen Consumption Rate on Tumor Development

By generating an array of tumors with varying proliferation rates (PR) and oxygen consumption rates (OCR), we are gaining a mechanistic understanding of the role of these two microscopic biological properties in macroscopic tumor development and its heterogeneity. We found that PR is the dominating factor for tumor growth rates while OCR marginally regulates tumor growth rates. Fast proliferating tumors were characterized by cell density heterogeneity and necrosis, while slow-growing tissue exhibited high homogeneity with no necrosis formation, regardless of OCR. This may provide insight into why normal tissue is always more homogeneous regardless of the wide OCR variation across different organs up to 10 times difference. The formation of central necrosis is dominated by the initial tumor growth rate, depending on the race between angiogenesis and tissue growth. It is observed that at the medium PR range, the higher PR combined with lower OCR is more prone to necrosis formation. This mirrors in vivo observations, where high-grade glioblastomas (GBMs) with rapid proliferation and lower oxygen demand are more prone to necrosis than low-grade GBMs. For cases that already have necrosis, the high OCR will make the viable rim thinner and increase the necrosis area. The vasculature density is dominated by OCR, with higher PR marginally decreasing the vessel density, highlighting that angiogenesis is a heavily demand-driven, self-regulated process that will automatically adjust itself to fulfill the tissue oxygen demand.

By analyzing an array of tumors with varying proliferation rates (PR) and oxygen consumption rates (OCR), we have deepened our mechanistic understanding of how these microscopic biological properties influence macroscopic tumor development and its heterogeneity. Our findings indicate that PR is the primary determinant of tumor growth rates, whereas OCR has a more marginal impact. Fast-proliferating tumors typically exhibit cell density heterogeneity and necrosis, whereas slow-growing tumors show high homogeneity without necrosis formation, regardless of OCR variations. This observation sheds light on why normal tissues maintain homogeneity despite the substantial OCR differences across various organs, which can vary up to tenfold, growth rate is the key.

The emergence of central necrosis appears to be governed primarily by the initial tumor growth rate, influenced by the balance between angiogenesis and tissue expansion. In cases with medium PR, tumors with higher PR and lower OCR are more susceptible to necrosis formation. This pattern aligns with in vivo knowledge where high-grade glioblastomas (GBMs), known for their rapid proliferation and lower oxygen demands, are more likely to develop necrosis compared to their low-grade counterparts. Furthermore, in scenarios where necrosis is already present, a high OCR tends to thin the viable rim and expand the necrotic area.

Vasculature density is primarily influenced by OCR, with higher PR slightly reducing vessel density. This underscores that angiogenesis is a demand-driven, self-regulating process, within a certain range, capable of automatically adjusting itself to meet the oxygen needs of the tissue.

4.4.2.4 *Radiomics Prediction and Interpretation*

To explore the application of Radiomics to capture advanced features beyond these handcrafted statistics to inform the underlying biology. We generated 20 tumors with random PR ranging from 0.8 to 1.2 and random OCR ranging from 2 to 4 mmHg/s. The risk of spurious correlation is estimated through correlation coefficient analysis and is believed not to compromise the conclusions in this study. A Lasso regression model was applied for PR/OCR prediction and its weight on each feature is acquired as a measurement of the feature importance for the prediction task. The Lasso model achieved high performance tested with leave-one-out cross-validation; the relative root mean squared error (RRMSE) for PR prediction is 4.6%, and that for OCR prediction is 11.5%. With the foundation of mechanistic understanding of the entire process from the previous sections, for the first time, we can understand and interpolate what these features stand for and why these features are selected.

For PR prediction, the most influential feature is the 90th percentile value of the original cell density map, which aligns with observations from the modeling where a high proliferation rate tends to create a high-density viable rim at the tumor periphery. The second-ranked feature is the Informational Measure of Correlation (IMC) 2 of the Gray Level Co-occurrence Matrix (GLCM) calculated from the high-pass wavelet-filtered cell density map. GLCM quantifies how often different combinations of pixel brightness values (gray levels) occur in an image. A higher IMC2 indicates more complex and detailed texture information in the image, which can suggest more randomness or irregularity in texture patterns. A low value of this feature indicates low

randomness or irregularity in cell density patterns, which may reflect the large, uniform, acellular necrotic region in high PR cases. The third feature is the complexity of the Neighbouring Gray Tone Difference Matrix (NGTDM) calculated from the high-pass wavelet-filtered hypoxic map. NGTDM focuses on the difference in intensity between a pixel and its neighbors within a specified distance. A low value of the complexity of this matrix indicates a low degree of texture irregularity of the hypoxia signal, which may indicate a large necrotic region producing a uniform zero hypoxia signal.

In OCR prediction, the most important feature is the perfused vessel length fraction. Higher OCR corresponds to higher vessel density stimulated by the tumor's demand, increasing the likelihood that the tumor vasculature is better connected through the angiogenesis process, resulting in a higher fraction of perfused tumor vasculature. The second feature is the small-area low gray-level emphasis of the Gray Level Size Zone Matrix (GLSZM) calculated from a high-pass wavelet-filtered blood volume map. The GLSZM quantifies the size of homogeneous zones for each gray level in an image. Small-Area Low Gray-Level Emphasis (SALGLE) of GLSZM measures the proportion of small areas (zones) with low gray levels, emphasizing the presence of small regions with low-intensity values within the image. Its positive relationship with OCR could be due to the more fractionated avascular regions in higher vessel density tumors, as observed in Figure 4-11. The third feature is the 90th percentile value of the Laplacian of Gaussian filtered tissue oxygen map, which reflects sharp transitions in tissue oxygen levels. This feature is negatively correlated with OCR because, in the relatively low PR range, lower OCR tumors are more likely to produce a necrotic core, resulting in a high oxygen gradient highlighted by this feature.

Beyond interpretability, our study reveals that certain physiological properties inherently have a more significant effect on tumor patterning. For example, a difference in PR is easier to identify compared to a difference in OCR through tumor property patterning. This provides a better understanding of what to expect from genetic alterations. Mutations leading to PR changes are more likely to be revealed through Radiomics compared to mutations leading to OCR changes, assuming the percentage of property alteration is the same. Future virtual biopsies could focus more on these biological properties that lead to more noticeable pattern changes. Furthermore, we identified property maps that best reflect the underlying biology. The cell density map and oxygen metabolism map work particularly well for PR prediction, while semantic vasculature property features and blood volume maps work better for OCR prediction, with generally higher imaging resolution preferred for OCR prediction. These findings provide valuable knowledge for imaging modality selection for the specific biology of interest.

In gengeral, our findings highlight the critical role of functional imaging in enhancing tumor characterization. The insights from our modeling can inform decisions about which tumor properties to focus on and guide the selection of the most appropriate imaging techniques. This strategic approach enables a more selective use of imaging modalities, concentrating on those that provide the most relevant information.

4.4.3 Advancement from Previous Studies

Numerous studies have explored vascularized tumor development, yet they often target different objectives and exhibit significant limitations in capturing tumor heterogeneities at the scale we are investigating. For example, Abbas Shirinifard[131] used an agent-based model to show asymmetric tumor cell cluster growth toward vasculature, focusing solely on a small scale. Similarly, Tobias Duswald et al.[133] developed a dynamic tree-like agent-based model using BioDynaMo[69], but their approach overlooked crucial processes such as anastomosis in vascularization and assumed that nutrients could be supplied through sprouting blind ends without considering perfusion. JP Alberding et al.[134,135] focused on simulating angiogenesis in the normal cerebral cortex and retina with a model that, while fully functional in terms of perfusion and oxygen transport, was confined to small-scale problems and excluded tissue growth or deformation. The green's function solver for their model, involving huge influence coefficient matrices, renders it unsuitable for scaling up to larger tissue and vasculature sizes. Vasileios Vavourakis et al.[132] proposed a hybrid model that combines a continuum approach for tumor growth with discrete vasculature modeling. While this model does account for angiogenesis and perfusion, its parallel vascular arrangement results in unrealistic vasculature morphologies and could introduce severe growth biases along the vessel direction, and tissue heterogeneity is not characterized in the model.

In response to these shortcomings, our research has developed a comprehensive model that significantly advances the simulation of vascularized tumor growth. This model specifically focuses on computational efficiency to reach heterogeneity-informative scales and functional accuracy to capture tumor features. Our unique designs or methods to achieve the goal are illustrated below.

Angiogenesis and vascular functions: Following the methodologies of Secomb et al.[152], we developed a comprehensive angiogenesis model that includes every stage from sprouting and elongation to anastomosis and vessel remodeling. This ensures a proper vasculature. We also perform comprehensive hemodynamics analysis to align vascular flow with its morphology and allow for subsequent WSS-based remodeling. For efficiency, we assume a homogeneous oxygen saturation level across the tissue. As low as 4.3% oxygen extraction fraction was observed on medium-size GL261 tumors (53 mm^3) in our prior modeling work. This assumption is likely to be valid for the smaller (12 mm^3) simulated tumors. For computational efficiency, we assume a uniform oxygen saturation level throughout the tissue. This assumption is supported by the observation of a low oxygen extraction fraction of just 4% in medium-sized GL261 tumors (53 mm^3). We anticipate that low oxygen extraction will hold true for the smaller (12 mm^3) tumors simulated in this study, simplifying our modeling process while maintaining its accuracy.

Capped vascular oxygen supply: The coarse mesh that fails to capture the sharp gradient of tissue oxygen near the blood vessel wall could overestimate the actual oxygen partial pressure difference across the vessel wall. Based on the observation from high-resolution numerical modeling of real GL261 vasculature, which reports a mean cross-vessel oxygen difference of only 0.8 mmHg, we applied a small cap to limit the oxygen source supply. This approach prevents unrealistic oxygen delivery rates without requiring an intensive meshing of the simulation domain.

Dynamically equilibrated host environment: To eliminate the need for explicitly modeling healthy tissue vasculature while maintaining a physiologically sound growth environment, we propose a novel dynamically equilibrated host environment. This approach assumes a balanced,

homogeneous vascular component that supports the host's oxygen demand. This ensures a spatially unbiased environmental condition and avoids the abnormally high boundary oxygen artifacts associated with Dirichlet boundaries. Such artifacts can lead to abnormal growth patterns, hinder peripheral TAF release, and complicate the initiation of angiogenesis from the host vasculature.

Stratified random host vasculature initialization: To avoid potential angiogenic biases sourced from improper environmental vessel arrangement, we proposed a novel spatially stratified tangent vessel method for initializing host vasculature. In this method, environmental vessels are represented as randomly positioned tangent lines at specified distances from the tumor surface, with orientations also randomized. The positioning of tangent points is carefully sampled in a spatially stratified manner to mitigate the risk of creating overly large vascular regions on the surface. This innovative approach ensures a simple yet theoretically unbiased vascular environment conducive to tumor development. Its stochastic nature, combined with high-throughput modeling, further reduces the risk of biases.

Dynamically equilibrated host environment: To eliminate the need for explicitly modeling healthy tissue vasculature while maintaining a physiologically sound growth environment, we propose a novel dynamic host oxygen environment. To eliminate the need for explicitly modeling healthy tissue vasculature while maintaining a physiologically sound growth environment, we propose a novel dynamic host oxygen environment. This approach assumes a virtual homogeneous host vascular that supports the host's oxygen demand and equilibrates at the designed oxygen level in the absence of a tumor. This ensures a spatially unbiased environmental condition and avoids the abnormally high boundary oxygen artifacts associated with Dirichlet

boundaries. Such artifacts can lead to abnormal growth patterns, hinder peripheral TAF release, and complicate the initiation of angiogenesis from the host vasculature.

Location-encoded boundary blood pressure: Alongside the initialization of environmental vessels, we have developed a novel location-encoded blood pressure assignment method to determine the pressures at the inlets and outlets of host vessels. This method incorporates two key components.

Novel boundary blood pressure condition: For tissues that are continuously growing and feature complex networks with hundreds of inlets and outlets, the proper boundary blood flow assignment is not feasible without the help of a computationally extensive optimization method. Moreover, fixed boundary flow conditions prohibit tissue perfusion as an emergency property reflecting vasculature functions. Ee developed a novel location-encoded blood pressure assignment method for our vasculature system. To ensure a physiological pressure gradient along host vessels throughout the simulation, we included a location-encoded blood pressure assignment term that estimates host vessel length and assigns pressure accordingly. To facilitate the pressure gradient establishment in daughter vessels bridging the host vessels, another angular-position-based variation term is applied to create an overall blood pressure shift of entire host vessels according to its random angular orientations.

Pressure blood boundary condition compatible radius remodeling: For vessel radius adaptation, we propose a novel method that aligns with the pressure-based boundary condition. While Wall Shear Stress (WSS) based vasculature regulation is a physiological mechanism observed in vivo, directly applying this principle for vessel radius remodeling can lead to

instabilities due to a positive feedback loop with a pressure-based boundary condition, where large vessels progressively enlarge, and small vessels diminish. To mitigate this, we have developed a reference radius and WSS-guided remodeling framework. This system still primarily utilizes WSS for radius remodeling but introduces constraints to limit deviations from a predetermined reference radius. Where the reference radius is determined by the intersection radius-flow point of the target WSS and flow velocity curve. This approach ensures a stable and functionally appropriate vessel radius distribution throughout the modeling process.

4.4.4 Limitations and Future Directions

Biological systems are inherently complex, and managing such systems requires ongoing effort. While we have achieved unprecedented modeling capabilities for heterogeneous, large-scale tumor development, our study is still limited in several ways. The scarcity of in vivo data, particularly functional data from specific tumor samples, hinders our ability to deepen our understanding of tumor behavior and calibrate our models more accurately to capture diverse aspects of tumor development. Currently, our simulations are restricted to mouse-scale tumors, which do not fully represent the complexity of larger human-scale tumors. Computational constraints also limit the size of tumors we can model, the resolution of our simulations, and the number of samples we can analyze in high-throughput studies. The solid mechanics model struggles to capture the viscoelastic behaviors of tumors that undergo self-rearrangement over prolonged periods and exhibit shape instabilities during development. Additionally, our

vasculature system models currently employ a threshold-based approach for determining oxygen sources, which may be inadequate for simulating tumors larger than a few centimeters, where oxygen extraction becomes more significant.

Future directions involve developing more sophisticated tumor mechanical models that account for various plastic and viscoelastic behaviors of tumor deformation and high-performance simulation platforms capable of scaling up the simulation to multi-centimeter levels. Vasculatures with explicitly modeled intravascular oxygen delivery are also needed for the larger-scale model.

With the advancement of technology in analyzing genetic material, the increasing availability of RNA-seq data that reflects gene expression levels in regions of interest opens new opportunities for computational modeling in terms of model parameterization and calibration. First, a database of the effects of various levels of key gene expression on apparent tumor properties can potentially be acquired through microscopic-level-focused experiments. Then, with this RNA-seq database, patient-specific RNA-seq data could be used to derive simulation parameters, enabling the construction of personalized tumor models.

RNA-seq-based parameterization also provides new calibration opportunities for patient-specific model calibration when combined with ex vivo organoids. Cell samples from patients can be cultured as organoids, serving as a calibration ground truth for patient-specific models with parameters generated from RNA-seq data. Additionally, longitudinal RNA-seq data of the evolving tumor could provide valuable insights into colony evolution and mutation occurrence,

allowing for the study of colony-resolved modeling that reflects intratumoral genetic heterogeneity.

Treatment outcome prediction will also be included in the future model. With the well-established baseline tumor and fully modeled biophysical functions, the delivery of drugs through the blood, as well as treatment efficiency in differentiated tumor regions with varied microenvironments or genetic conditions, can be modeled. The tumor evolution under various treatment interventions, including radiation therapy, chemotherapy, immunotherapy, receptor-targeted therapy, and vasculature-targeted therapy, can be explored with arbitrary treatment combinations and plans. By incorporating personalized biophysical and genetic data for model parameterization, the exploration of personalized treatment can be significantly facilitated through computational modeling while ensuring the entire exploration process can be reasoned and trusted.

4.5 Conclusion

In this study, we introduced a hybrid simulation platform that integrates continuum tissue dynamics with discrete vasculature modeling for large-scale, vascularized tumor growth simulations with comprehensive hemodynamic capabilities. Through innovative vasculature conditioning and remodeling strategies, this platform enables unbiased simulations of tumor

development to sizes previously unattainable, closely mirroring the biophysical vascular properties and tissue growth patterns observed in actual tumors.

Our study has significant implications for understanding tumor characteristics. By examining the influence of cellular proliferation rate (PR) and oxygen consumption rate (OCR) on tumor patterning and heterogeneity, we have elucidated the mechanistic links between biophysical properties and tumor characteristics. Key findings include the pivotal role of tumor proliferation rate in driving necrosis and tissue heterogeneity and the impact of OCR on tissue vascular density. Using our platform, we analyzed 20 randomly generated samples to predict PR and OCR using Radiomics, based on semantic and agnostic features. The resulting high-performance predictive model sees through tumor appearance to identify critical features that uncover underlying biological processes. Given the insight from modeling, the rationale behind feature selection can be understood, and features can be interpreted.

Our study advanced our understanding of the complex tumor vasculature and tissue development problem and laid the groundwork for integrating computational models with Radiomics, bridging the gap between data-driven tumor prediction and fundamental biophysics. This integration opens up exciting new avenues for research in personalized medicine and beyond. It provides a new paradigm for interpreting tumor features and can help identify tumor property types with the highest potential to reveal specific biophysical properties, guiding the development and selection of imaging modalities for advanced non-invasive biophysical assessments.

5.References

1. Gillies, R. J., Kinahan, P. E. & Hricak, H. Radiomics: Images Are More than Pictures, They Are Data. *Radiology* **278**, 563–577 (2015).

2. Aerts, H. J. W. L. *et al.* Decoding tumour phenotype by noninvasive imaging using a quantitative radiomics approach. *Nat. Commun.* **5**, 1–9 (2014).

3. van Timmeren, J. E., Cester, D., Tanadini-Lang, S., Alkadhi, H. & Baessler, B. Radiomics in medical imaging—"how-to" guide and critical reflection. *Insights Imaging* **11**, 91 (2020).

4. Zhang, W., Guo, Y. & Jin, Q. Radiomics and Its Feature Selection: A Review. *Symmetry* **15**, 1834 (2023).

5. Johansen, R. *et al.* Predicting survival and early clinical response to primary chemotherapy for patients with locally advanced breast cancer using DCE-MRI. *J. Magn. Reson. Imaging* **29**, 1300–1307 (2009).

6. Mu, W. *et al.* Staging of cervical cancer based on tumor heterogeneity characterized by texture features on18F-FDG PET images. *Phys. Med. Biol.* **60**, 5123–5139 (2015).

7. Nie, K. *et al.* Quantitative Analysis of Lesion Morphology and Texture Features for Diagnostic Prediction in Breast MRI. *Acad. Radiol.* **15**, 1513–1525 (2008).

8. Gutman, D. A. *et al.* Somatic mutations associated with MRI-derived volumetric features in glioblastoma. *Neuroradiology* **57**, 1227–1237 (2015).

9. Avanzo, M. *et al.* Machine and deep learning methods for radiomics. *Med. Phys.* **47**, e185–e202 (2020).

10. Balagurunathan, Y. *et al.* Test–Retest Reproducibility Analysis of Lung CT Image Features. *J. Digit. Imaging* **27**, 805–823 (2014).

11. Guha, A. *et al.* Radiomic analysis for response assessment in advanced head and neck cancers, a distant dream or an inevitable reality? A systematic review of the current level of evidence. *Br. J. Radiol.* **93**, 20190496 (2020).

12. Lohmann, P., Bousabarah, K., Hoevels, M. & Treuer, H. Radiomics in radiation oncology—basics, methods, and limitations. *Strahlenther. Onkol.* **196**, 848–855 (2020).

13. Sanduleanu, S. *et al.* Tracking tumor biology with radiomics: A systematic review utilizing a radiomics quality score. *Radiother. Oncol.* **127**, 349–360 (2018).

14. Ghosh, P., Tamboli, P., Vikram, R. & Rao, A. Imaging-genomic pipeline for identifying gene mutations using three-dimensional intra-tumor heterogeneity features. *J. Med. Imaging* **2**, 041009 (2015).

15. Guo, W. *et al.* Prediction of clinical phenotypes in invasive breast carcinomas from the integration of radiomics and genomics data. *J. Med. Imaging* **2**, 041007 (2015).

16. Yin, Q. *et al.* Associations between Tumor Vascularity, Vascular Endothelial Growth Factor Expression and PET/MRI Radiomic Signatures in Primary Clear-Cell–Renal-Cell-Carcinoma: Proof-of-Concept Study. *Sci. Rep.* **7**, 43356 (2017).

17. Lopez, C. J. *et al.* Association of Radiomics and Metabolic Tumor Volumes in Radiation Treatment of Glioblastoma Multiforme. *Int. J. Radiat. Oncol.* **97**, 586–595 (2017).

18. Luo, Y. *et al.* Development of a Fully Cross-Validated Bayesian Network Approach for Local Control Prediction in Lung Cancer. *IEEE Trans. Radiat. Plasma Med. Sci.* **3**, 232–241 (2019).

19. Nguyen, A., Yosinski, J. & Clune, J. Understanding Neural Networks via Feature Visualization: A Survey. in *Explainable AI: Interpreting, Explaining and Visualizing Deep Learning* (eds. Samek, W., Montavon, G., Vedaldi, A., Hansen, L. K. & Müller, K.-R.) 55–76 (Springer International Publishing, Cham, 2019). doi:10.1007/978-3-030-28954-6_4.

20. Hollstein, M., Sidransky, D., Vogelstein, B. & Harris, C. C. p53 Mutations in Human Cancers. *Science* **253**, 49–53 (1991).

21. Nicholson, R. I., Gee, J. M. W. & Harper, M. E. EGFR and cancer prognosis. *Eur. J. Cancer* **37**, 9–15 (2001).

22. Song, M. S., Salmena, L. & Pandolfi, P. P. The functions and regulation of the PTEN tumour suppressor. *Nat. Rev. Mol. Cell Biol.* **13**, 283–296 (2012).

23. Dang, C. V. MYC on the Path to Cancer. *Cell* **149**, 22–35 (2012).

24. Hasin, Y., Seldin, M. & Lusis, A. Multi-omics approaches to disease. *Genome Biol.* **18**, 83 (2017).

25. Bray, F. *et al.* Global cancer statistics 2018: GLOBOCAN estimates of incidence and mortality worldwide for 36 cancers in 185 countries. *CA. Cancer J. Clin.* **68**, 394–424 (2018).

26. Hanahan, D. & Weinberg, R. A. Hallmarks of Cancer: The Next Generation. *Cell* **144**, 646–674 (2011).

27. Hanahan, D. & Weinberg, R. A. The Hallmarks of Cancer. *Cell* **100**, 57–70 (2000).

28. Gonçalves, E. *et al.* Bridging the layers: towards integration of signal transduction, regulation and metabolism into mathematical models. *Mol. Biosyst.* **9**, 1576–1583 (2013).

29. Ghaffarizadeh, A., Heiland, R., Friedman, S. H., Mumenthaler, S. M. & Macklin, P. PhysiCell: An open source physics-based cell simulator for 3-D multicellular systems. *PLoS Comput. Biol.* **14**, (2018).

30. Metzcar, J., Wang, Y., Heiland, R. & Macklin, P. A Review of Cell-Based Computational Modeling in Cancer Biology. *JCO Clin. Cancer Inform.* 1–13 (2019) doi:10.1200/CCI.18.00069.

31. Graner, F. & Glazier, J. A. Simulation of biological cell sorting using a two-dimensional extended Potts model. *Phys. Rev. Lett.* **69**, 2013–2016 (1992).

32. Lowengrub, J. S. *et al.* Nonlinear modelling of cancer: bridging the gap between cells and tumours. *Nonlinearity* **23**, R1–R91 (2009).

33. Wolf-Gladrow, D. A. *Lattice-Gas Cellular Automata and Lattice Boltzmann Models: An Introduction*. (Springer, 2004).

34. Van Liedekerke, P., Palm, M. M., Jagiella, N. & Drasdo, D. Simulating tissue mechanics with agent-based models: concepts, perspectives and some novel results. *Comput. Part. Mech.* **2**, 401–444 (2015).

35. Macklin, P., Edgerton, M. E., Thompson, A. M. & Cristini, V. Patient-calibrated agent-based modelling of ductal carcinoma in situ (DCIS): From microscopic measurements to macroscopic predictions of clinical progression. *J. Theor. Biol.* **301**, 122–140 (2012).

36. Alt, S., Ganguly, P. & Salbreux, G. Vertex models: from cell mechanics to tissue morphogenesis. *Philos. Trans. R. Soc. B Biol. Sci.* **372**, 20150520 (2017).

37. Oden, J. T., Hawkins, A. & Prudhomme, S. General diffuse-interface theories and an approach to predictive tumor growth modeling. *Math. Models Methods Appl. Sci.* **20**, 477–517 (2010).

38. Oden, J. T. *et al.* Toward Predictive Multiscale Modeling of Vascular Tumor Growth. *Arch. Comput. Methods Eng.* **23**, 735–779 (2016).

39. Cristini, V., Li, X., Lowengrub, J. S. & Wise, S. M. Nonlinear simulations of solid tumor growth using a mixture model: invasion and branching. *J. Math. Biol.* **58**, 723 (2008).

40. Wang, Z. & Deisboeck, T. S. Computational modeling of brain tumors: discrete, continuum or hybrid? in *Scientific Modeling and Simulations* (eds. Yip, S. & de la Rubia, T. D.) 381–393 (Springer Netherlands, Dordrecht, 2009). doi:10.1007/978-1-4020-9741-6_20.

41. Kłusek, A., Łoś, M., Paszyński, M. & Dzwinel, W. Efficient model of tumor dynamics simulated in multi-GPU environment. *Int. J. High Perform. Comput. Appl.* **33**, 489–506 (2019).

42. Elazab, A. *et al.* Macroscopic Cerebral Tumor Growth Modeling From Medical Images: A Review. *IEEE Access* **6**, 30663–30679 (2018).

43. Qin, R. S. & Bhadeshia, H. K. Phase field method. *Mater. Sci. Technol.* **26**, 803–811 (2010).

44. Kobayashi, R. A brief introduction to phase field method. *AIP Conf. Proc.* **1270**, 282–291 (2010).

45. Lorenzo, G. *et al.* Tissue-scale, personalized modeling and simulation of prostate cancer growth. *Proc. Natl. Acad. Sci.* **113**, E7663–E7671 (2016).

46. Karolak, A., Markov, D. A., McCawley, L. J. & Rejniak, K. A. Towards personalized computational oncology: from spatial models of tumour spheroids, to organoids, to tissues. *J. R. Soc. Interface* **15**, 20170703 (2018).

47. Tang, J. *et al.* Phenotypic transition maps of 3D breast acini obtained by imaging-guided agent-based modeling. *Integr. Biol.* **3**, 408–421 (2011).

48. Poplawski, N. J. *et al.* Front Instabilities and Invasiveness of Simulated 3D Avascular Tumors. *PLoS ONE* **5**, (2010).

49. Piotrowska, M. J. & Angus, S. D. A quantitative cellular automaton model of in vitro multicellular spheroid tumour growth. *J. Theor. Biol.* **258**, 165–178 (2009).

50. Phillips, C. M., Lima, E. A. B. F., Woodall, R. T., Brock, A. & Yankeelov, T. E. A hybrid model of tumor growth and angiogenesis: In silico experiments. *PLoS ONE* **15**, (2020).

51. Scott, J. G., Fletcher, A. G., Anderson, A. R. A. & Maini, P. K. Spatial Metrics of Tumour Vascular Organisation Predict Radiation Efficacy in a Computational Model. *PLoS Comput. Biol.* **12**, (2016).

52. Rejniak, K. A. *et al.* The Role of Tumor Tissue Architecture in Treatment Penetration and Efficacy: An Integrative Study. *Front. Oncol.* **3**, (2013).

53. Merlo, L. M. F., Pepper, J. W., Reid, B. J. & Maley, C. C. Cancer as an evolutionary and ecological process. *Nat. Rev. Cancer* **6**, 924–935 (2006).

54. Muz, B., de la Puente, P., Azab, F. & Azab, A. K. The role of hypoxia in cancer progression, angiogenesis, metastasis, and resistance to therapy. *Hypoxia* **3**, 83–92 (2015).

55. McKeown, S. R. Defining normoxia, physoxia and hypoxia in tumours—implications for treatment response. *Br. J. Radiol.* **87**, 20130676 (2014).

56. Ganeshan, B. & Miles, K. A. Quantifying tumour heterogeneity with CT. *Cancer Imaging* **13**, 140–149 (2013).

57. Ganeshan, B. *et al.* Non–Small Cell Lung Cancer: Histopathologic Correlates for Texture Parameters at CT. *Radiology* **266**, 326–336 (2013).

58. Grant, M. R., Mostov, K. E., Tlsty, T. D. & Hunt, C. A. Simulating Properties of In Vitro Epithelial Cell Morphogenesis. *PLoS Comput. Biol.* **2**, (2006).

59. Perfahl, H. *et al.* Multiscale Modelling of Vascular Tumour Growth in 3D: The Roles of Domain Size and Boundary Conditions. *PLoS ONE* **6**, (2011).

60. Lundh, T. Cellular Automaton Modeling of Biological Pattern Formation: Characterization, Applications, and Analysis Authors: Andreas Deutsch and Sabine Dormann, Birkhäuser, 2005, XXVI, 334 p., 131 illus., Hardcover. ISBN:0-8176-4281-1, List Price: $89.95. *Genet. Program. Evolvable Mach.* **8**, 105–106 (2007).

61. Chopard, B., Ouared, R., Deutsch, A., Hatzikirou, H. & Wolf-Gladrow, D. Lattice-Gas Cellular Automaton Models for Biology: From Fluids to Cells. *Acta Biotheor.* **58**, 329–340 (2010).

62. Graner, F. & Glazier, J. A. Simulation of biological cell sorting using a two-dimensional extended Potts model. *Phys. Rev. Lett.* **69**, 2013–2016 (1992).

63. Kang, S., Kahan, S., McDermott, J., Flann, N. & Shmulevich, I. Biocellion : accelerating computer simulation of multicellular biological system models. *Bioinformatics* **30**, 3101–3108 (2014).

64. Breitwieser, L. *et al.* BioDynaMo: a general platform for scalable agent-based simulation. *ArXiv200606775 Cs* (2021).

65. Germann, P., Marin-Riera, M. & Sharpe, J. ya||a: GPU-Powered Spheroid Models for Mesenchyme and Epithelium. *Cell Syst.* **8**, 261-266.e3 (2019).

66. Mirams, G. R. *et al.* Chaste: An Open Source C++ Library for Computational Physiology and Biology. *PLOS Comput. Biol.* **9**, e1002970 (2013).

67. Mathias, S., Coulier, A. & Hellander, A. *CBMOS: A GPU-Enabled Python Framework for the Numerical Study of Center-Based Models*. 2021.05.06.442893 https://www.biorxiv.org/content/10.1101/2021.05.06.442893v2 (2021) doi:10.1101/2021.05.06.442893.

68. Hesam, A., Breitwieser, L., Rademakers, F. & Al-Ars, Z. GPU Acceleration of 3D Agent-Based Biological Simulations. *2021 IEEE Int. Parallel Distrib. Process. Symp. Workshop IPDPSW* 210–217 (2021) doi:10.1109/IPDPSW52791.2021.00040.

69. Breitwieser, L. *et al.* BioDynaMo: a modular platform for high-performance agent-based simulation. *Bioinformatics* **38**, 453–460 (2022).

70. Baghban, R. *et al.* Tumor microenvironment complexity and therapeutic implications at a glance. *Cell Commun. Signal.* **18**, 59 (2020).

71. Ghaffarizadeh, A., Friedman, S. H. & Macklin, P. BioFVM: an efficient, parallelized diffusive transport solver for 3-D biological simulations. *Bioinformatics* **32**, 1256–1258 (2016).

72. Povitsky, A. & Morris, P. J. A Higher-Order Compact Method in Space and Time Based on Parallel Implementation of the Thomas Algorithm. *J. Comput. Phys.* **161**, 182–203 (2000).

73. Satish, N., Harris, M. & Garland, M. Designing efficient sorting algorithms for manycore GPUs. in *2009 IEEE International Symposium on Parallel Distributed Processing* 1–10 (2009). doi:10.1109/IPDPS.2009.5161005.

74. Z-order curve. *Wikipedia* (2022).

75. Zanoni, M. *et al.* 3D tumor spheroid models for in vitro therapeutic screening: a systematic approach to enhance the biological relevance of data obtained. *Sci. Rep.* **6**, 19103 (2016).

76. Kimlin, L. C., Casagrande, G. & Virador, V. M. In vitro three-dimensional (3D) models in cancer research: An update. *Mol. Carcinog.* **52**, 167–182 (2013).

77. Bull, J. A., Mech, F., Quaiser, T., Waters, S. L. & Byrne, H. M. Mathematical modelling reveals cellular dynamics within tumour spheroids. *PLOS Comput. Biol.* **16**, e1007961 (2020).

78. Dorie, M. J., Kallman, R. F., Rapacchietta, D. F., Van Antwerp, D. & Huang, Y. R. Migration and internalization of cells and polystyrene microspheres in tumor cell spheroids. *Exp. Cell Res.* **141**, 201–209 (1982).

79. Mao, X. *et al.* An agent-based model for drug-radiation interactions in the tumour microenvironment: Hypoxia-activated prodrug SN30000 in multicellular tumour spheroids. *PLOS Comput. Biol.* **14**, e1006469 (2018).

80. Doctor, A., Seifert, V., Ullrich, M., Hauser, S. & Pietzsch, J. Three-Dimensional Cell Culture Systems in Radiopharmaceutical Cancer Research. *Cancers* **12**, 2765 (2020).

81. Burstein, H. J., Polyak, K., Wong, J. S., Lester, S. C. & Kaelin, C. M. Ductal Carcinoma in Situ of the Breast. *N. Engl. J. Med.* **350**, 1430–1441 (2004).

82. Grimm, L. J., Rahbar, H., Abdelmalak, M., Hall, A. H. & Ryser, M. D. Ductal Carcinoma in Situ: State-of-the-Art Review. *Radiology* **302**, 246–255 (2022).

83. Franks, S. J., Byrne, H. M., Underwood, J. C. E. & Lewis, C. E. Biological inferences from a mathematical model of comedo ductal carcinoma in situ of the breast. *J. Theor. Biol.* **232**, 523–543 (2005).

84. Franks, S. J., Byrne, H. M., King, J. R., Underwood, J. C. E. & Lewis, C. E. Modelling the early growth of ductal carcinoma in situ of the breast. *J. Math. Biol.* **47**, 424–452 (2003).

85. Rejniak, K. A. & Dillon, R. H. A single cell-based model of the ductal tumour microarchitecture. *Comput. Math. Methods Med.* **8**, 51–69 (2007).

86. Norton, K.-A. *et al.* A 2D mechanistic model of breast ductal carcinoma in situ (DCIS) morphology and progression. *J. Theor. Biol.* **263**, 393–406 (2010).

87. Butner, J. D. *et al.* A Multiscale Agent-Based Model of Ductal Carcinoma In Situ. *IEEE Trans. Biomed. Eng.* **67**, 1450–1461 (2020).

88. Lin, B. *et al.* Mechanisms of FLASH effect. *Front. Oncol.* **12**, 995612 (2022).

89. Pries, A. R. *et al.* Resistance to blood flow in microvessels in vivo. *Circ. Res.* **75**, 904–915 (1994).

90. Pries, A. R. & Secomb, T. W. Microvascular blood viscosity in vivo and the endothelial surface layer. *Am. J. Physiol.-Heart Circ. Physiol.* **289**, H2657–H2664 (2005).

91. Fry, B. C., Lee, J., Smith, N. P. & Secomb, T. W. Estimation of Blood Flow Rates in Large Microvascular Networks. *Microcirculation* **19**, 530–538 (2012).

92. Kreuzer, F. Oxygen supply to tissues: The Krogh model and its assumptions. *Experientia* **38**, 1415–1426 (1982).

93. Grimes, D. R. *et al.* Estimating oxygen distribution from vasculature in three-dimensional tumour tissue. *J. R. Soc. Interface* **13**, 20160070 (2016).

94. Cui, S. & Pratx, G. 3D computational model of oxygen depletion kinetics in brain vasculature during FLASH RT and its implications for in vivo oximetry experiments. *Med. Phys.* **49**, 3914–3925 (2022).

95. Secomb, T. W., Hsu, R., Park, E. Y. H. & Dewhirst, M. W. Green's Function Methods for Analysis of Oxygen Delivery to Tissue by Microvascular Networks. *Ann. Biomed. Eng.* **32**, 1519–1529 (2004).

96. Secomb, T. W. A Green's function method for simulation of time-dependent solute transport and reaction in realistic microvascular geometries. *Math. Med. Biol. J. IMA* **33**, 475–494 (2016).

97. d'Esposito, A. *et al.* Computational fluid dynamics with imaging of cleared tissue and of in vivo perfusion predicts drug uptake and treatment responses in tumours. *Nat. Biomed. Eng.* **2**, 773–787 (2018).

98. Kirst, C. *et al.* Mapping the Fine-Scale Organization and Plasticity of the Brain Vasculature. *Cell* **180**, 780-795.e25 (2020).

99. Wang, Q. *et al.* The Allen Mouse Brain Common Coordinate Framework: A 3D Reference Atlas. *Cell* **181**, 936-953.e20 (2020).

100. Du, J. & Sheng, K. Oxygen Depletion Kinetics Due to Flash with Real Tumor Vasculature Coupling. in (AAPM, 2023).

101. Fåhræus, R. & Lindqvist, T. THE VISCOSITY OF THE BLOOD IN NARROW CAPILLARY TUBES. *Am. J. Physiol.-Leg. Content* **96**, 562–568 (1931).

102. Pries, A. R., Neuhaus, D. & Gaehtgens, P. Blood viscosity in tube flow: dependence on diameter and hematocrit. *Am. J. Physiol.-Heart Circ. Physiol.* **263**, H1770–H1778 (1992).

103. Botkin, N. D., Kovtanyuk, A. E., Turova, V. L., Sidorenko, I. N. & Lampe, R. Accounting for Tube Hematocrit in Modeling of Blood Flow in Cerebral Capillary Networks. *Comput. Math. Methods Med.* **2019**, 4235937 (2019).

104. Pries, A. R. *et al.* Microvascular blood flow resistance: role of endothelial surface layer. *Am. J. Physiol.-Heart Circ. Physiol.* **273**, H2272–H2279 (1997).

105. Stamatelos, S. K., Kim, E., Pathak, A. P. & Popel, A. S. A bioimage informatics based reconstruction of breast tumor microvasculature with computational blood flow predictions. *Microvasc. Res.* **91**, 8–21 (2014).

106. Saad, Y. & Schultz, M. H. GMRES: A Generalized Minimal Residual Algorithm for Solving Nonsymmetric Linear Systems. *SIAM J. Sci. Stat. Comput.* **7**, 856–869 (1986).

107. Du, J. & Sheng, K. Modeling Tumor Vasculature for Perfusion and Oxygenation Analysis. in (AAPM, 2023).

108. Pries, A. R., Ley, K., Claassen, M. & Gaehtgens, P. Red cell distribution at microvascular bifurcations. *Microvasc. Res.* **38**, 81–101 (1989).

109. Pittman, R. N. Tissue Gas Transport. in *Regulation of Tissue Oxygenation* (Morgan & Claypool Life Sciences, 2011).

110. Everds, N. CHAPTER 17 - Hematology of the Mouse. in *The Laboratory Mouse* (eds. Hedrich, H. J. & Bullock, G.) 271–286 (Academic Press, London, 2004). doi:10.1016/B978-012336425-8/50070-4.

111. Murray, C. D. The Physiological Principle of Minimum Work. *Proc. Natl. Acad. Sci. U. S. A.* **12**, 207–214 (1926).

112. Sherman, T. F. On connecting large vessels to small. The meaning of Murray's law. *J. Gen. Physiol.* **78**, 431–453 (1981).

113. Hafen, B. B. & Sharma, S. Oxygen Saturation. in *StatPearls* (StatPearls Publishing, Treasure Island (FL), 2024).

114. Kerger, H., Torres Filho, I. P., Rivas, M., Winslow, R. M. & Intaglietta, M. Systemic and subcutaneous microvascular oxygen tension in conscious Syrian golden hamsters. *Am. J. Physiol.-Heart Circ. Physiol.* **268**, H802–H810 (1995).

115. Hellums, J. D., Nair, P. K., Huang, N. S. & Ohshima, N. Simulation of intraluminal gas transport processes in the microcirculation. *Ann. Biomed. Eng.* **24**, 1–24 (1995).

116. Lu, Y., Hu, D. & Ying, W. A fast numerical method for oxygen supply in tissue with complex blood vessel network. *PLOS ONE* **16**, e0247641 (2021).

117. Goldman, D. Theoretical Models of Microvascular Oxygen Transport to Tissue. *Microcirc. N. Y. N 1994* **15**, 795–811 (2008).

118. Wagner, B. A., Venkataraman, S. & Buettner, G. R. The Rate of Oxygen Utilization by Cells. *Free Radic. Biol. Med.* **51**, 700–712 (2011).

119. Jetté, M., Sidney, K. & Blümchen, G. Metabolic equivalents (METS) in exercise testing, exercise prescription, and evaluation of functional capacity. *Clin. Cardiol.* **13**, 555–565 (1990).

120. Rink, C. & Khanna, S. Significance of Brain Tissue Oxygenation and the Arachidonic Acid Cascade in Stroke. *Antioxid. Redox Signal.* **14**, 1889–1903 (2011).

121. Wiesner, H. M. *et al.* Quantitative and simultaneous measurement of oxygen consumption rates in rat brain and skeletal muscle using 17O MRS imaging at 16.4T. *Magn. Reson. Med.* **85**, 2232–2246 (2021).

122. Liberti, M. V. & Locasale, J. W. The Warburg Effect: How Does it Benefit Cancer Cells? *Trends Biochem. Sci.* **41**, 211–218 (2016).

123. Paech, D. *et al.* Quantitative Dynamic Oxygen 17 MRI at 7.0 T for the Cerebral Oxygen Metabolism in Glioma. *Radiology* **295**, 181–189 (2020).

124. Hu, Y., Li, T.-M., Anderson, L., Ragan-Kelley, J. & Durand, F. Taichi: a language for high-performance computation on spatially sparse data structures. *ACM Trans. Graph.* **38**, 201:1-201:16 (2019).

125. Helmlinger, G., Yuan, F., Dellian, M. & Jain, R. K. Interstitial pH and pO2 gradients in solid tumors in vivo: High-resolution measurements reveal a lack of correlation. *Nat. Med.* **3**, 177–182 (1997).

126. Zhong, J., Sakaki, M., Okada, H. & Ahrens, E. T. In Vivo Intracellular Oxygen Dynamics in Murine Brain Glioma and Immunotherapeutic Response of Cytotoxic T Cells Observed by Fluorine-19 Magnetic Resonance Imaging. *PLoS ONE* **8**, e59479 (2013).

127. Xu, K., Boas, D. A., Sakadžić, S. & LaManna, J. C. Brain Tissue PO2 Measurement During Normoxia and Hypoxia Using Two-Photon Phosphorescence Lifetime Microscopy. *Adv. Exp. Med. Biol.* **977**, 149–153 (2017).

128. Ausprunk, D. H. & Folkman, J. Migration and proliferation of endothelial cells in preformed and newly formed blood vessels during tumor angiogenesis. *Microvasc. Res.* **14**, 53–65 (1977).

129. Weinberg, R. A. & Weinberg, R. A. *The Biology of Cancer*. (Garland Science, 2013).

130. Nagy, J. A., Chang, S.-H., Shih, S.-C., Dvorak, A. M. & Dvorak, H. F. Heterogeneity of the Tumor Vasculature. *Semin. Thromb. Hemost.* **36**, 321–331 (2010).

131. Shirinifard, A. *et al.* 3D Multi-Cell Simulation of Tumor Growth and Angiogenesis. *PLoS ONE* **4**, (2009).

132. Vavourakis, V. *et al.* A Validated Multiscale In-Silico Model for Mechano-sensitive Tumour Angiogenesis and Growth. *PLOS Comput. Biol.* **13**, e1005259 (2017).

133. Duswald, T., Lima, E. A. B. F., Oden, J. T. & Wohlmuth, B. Bridging scales: A hybrid model to simulate vascular tumor growth and treatment response. *Comput. Methods Appl. Mech. Eng.* **418**, 116566 (2024).

134. Alberding, J. P. & Secomb, T. W. Simulation of angiogenesis in three dimensions: Application to cerebral cortex. *PLOS Comput. Biol.* **17**, e1009164 (2021).

135. Alberding, J. P. & Secomb, T. W. Simulation of Angiogenesis in Three Dimensions: Development of the Retinal Circulation. *Bull. Math. Biol.* **85**, 27 (2023).

136. MacLaurin, J. The buckling of capillaries in tumours. (University of Oxford, 2011).

137. Nia, H. T., Munn, L. L. & Jain, R. K. Physical traits of cancer. *Science* **370**, eaaz0868 (2020).

138. Bhargav, A. G., Domino, J. S., Chamoun, R. & Thomas, S. M. Mechanical Properties in the Glioma Microenvironment: Emerging Insights and Theranostic Opportunities. *Front. Oncol.* **11**, (2022).

139. Moran, R., Smith, J. H. & García, J. J. Fitted hyperelastic parameters for Human brain tissue from reported tension, compression, and shear tests. *J. Biomech.* **47**, 3762–3766 (2014).

140. Szatmári, T. *et al.* Detailed characterization of the mouse glioma 261 tumor model for experimental glioblastoma therapy. *Cancer Sci.* **97**, 546–553 (2006).

141. Casciari, J. J., Sotirchos, S. V. & Sutherland, R. M. Variations in tumor cell growth rates and metabolism with oxygen concentration, glucose concentration, and extracellular pH. *J. Cell. Physiol.* **151**, 386–394 (1992).

142. Wu, S., Calero-Pérez, P., Arús, C. & Candiota, A. P. Anti-PD-1 Immunotherapy in Preclinical GL261 Glioblastoma: Influence of Therapeutic Parameters and Non-Invasive

Response Biomarker Assessment with MRSI-Based Approaches. *Int. J. Mol. Sci.* **21**, 8775 (2020).

143. Rutter, E. M. *et al.* Mathematical Analysis of Glioma Growth in a Murine Model. *Sci. Rep.* **7**, 2508 (2017).

144. Secomb, T. W., Hsu, R., Dewhirst, M. W., Klitzman, B. & Gross, J. F. Analysis of oxygen transport to tumor tissue by microvascular networks. *Int. J. Radiat. Oncol.* **25**, 481–489 (1993).

145. Roy, T. K. & Secomb, T. W. Functional implications of microvascular heterogeneity for oxygen uptake and utilization. *Physiol. Rep.* **10**, e15303 (2022).

146. Carreau, A., Hafny-Rahbi, B. E., Matejuk, A., Grillon, C. & Kieda, C. Why is the partial oxygen pressure of human tissues a crucial parameter? Small molecules and hypoxia. *J. Cell. Mol. Med.* **15**, 1239–1253 (2011).

147. Adair, T. H. & Montani, J.-P. Overview of Angiogenesis. in *Angiogenesis* (Morgan & Claypool Life Sciences, 2010).

148. Yadav, L., Puri, N., Rastogi, V., Satpute, P. & Sharma, V. Tumour Angiogenesis and Angiogenic Inhibitors: A Review. *J. Clin. Diagn. Res. JCDR* **9**, XE01–XE05 (2015).

149. Blanco, R. & Gerhardt, H. VEGF and Notch in Tip and Stalk Cell Selection. *Cold Spring Harb. Perspect. Med.* **3**, a006569 (2013).

150. Gerhardt, H. *et al.* VEGF guides angiogenic sprouting utilizing endothelial tip cell filopodia. *J. Cell Biol.* **161**, 1163–1177 (2003).

151. Wood, L. B., Ge, R., Kamm, R. D. & Asada, H. H. Nascent vessel elongation rate is inversely related to diameter in in vitro angiogenesis. *Integr. Biol.* **4**, 1081–1089 (2012).

152. Secomb, T. W., Alberding, J. P., Hsu, R., Dewhirst, M. W. & Pries, A. R. Angiogenesis: An Adaptive Dynamic Biological Patterning Problem. *PLOS Comput. Biol.* **9**, e1002983 (2013).

153. Gaehtgens, P. A. L. Radial and longitudinal distensibility of arterial microvessels in the mesentery and their dependence on extravascular structures. *Pflüg. Arch.* **330**, 277–289 (1971).

154. Jackson, Z. S., Gotlieb, A. I. & Langille, B. L. Wall Tissue Remodeling Regulates Longitudinal Tension in Arteries. *Circ. Res.* **90**, 918–925 (2002).

155. Pries, A. R., Secomb, T. W. & Gaehtgens, P. Design Principles of Vascular Beds. *Circ. Res.* **77**, 1017–1023 (1995).

156. Schmid, F., Tsai, P. S., Kleinfeld, D., Jenny, P. & Weber, B. Depth-dependent flow and pressure characteristics in cortical microvascular networks. *PLOS Comput. Biol.* **13**, e1005392 (2017).

157. Bentley, T. B., Meng, H. & Pittman, R. N. Temperature dependence of oxygen diffusion and consumption in mammalian striated muscle. *Am. J. Physiol.-Heart Circ. Physiol.* **264**, H1825–H1830 (1993).

158. Epel, B., Redler, G. & Halpern, H. J. How in vivo EPR Measures and Images Oxygen. *Adv. Exp. Med. Biol.* **812**, 113–119 (2014).

159. Warren, D. R. & Partridge, M. The role of necrosis, acute hypoxia and chronic hypoxia in 18F-FMISO PET image contrast: a computational modelling study. *Phys. Med. Biol.* **61**, 8596 (2016).

160. McKinley, E. T. *et al.* Limits of [18F]-FLT PET as a Biomarker of Proliferation in Oncology. *PLOS ONE* **8**, e58938 (2013).

161. Pries, A. R., Höpfner, M., le Noble, F., Dewhirst, M. W. & Secomb, T. W. The shunt problem: control of functional shunting in normal and tumour vasculature. *Nat. Rev. Cancer* **10**, 587–593 (2010).

162. Hahn, A. *et al.* Glioblastoma multiforme restructures the topological connectivity of cerebrovascular networks. *Sci. Rep.* **9**, 11757 (2019).

163. Siemann, D. W. & Horsman, M. R. Vascular targeted therapies in oncology. *Cell Tissue Res.* **335**, 241–248 (2009).

164. Jain, R. K. Normalization of Tumor Vasculature: An Emerging Concept in Antiangiogenic Therapy. *Science* **307**, 58–62 (2005).

165. van Griethuysen, J. J. *et al.* Computational Radiomics System to Decode the Radiographic Phenotype. *Cancer Res.* **77**, e104–e107 (2017).